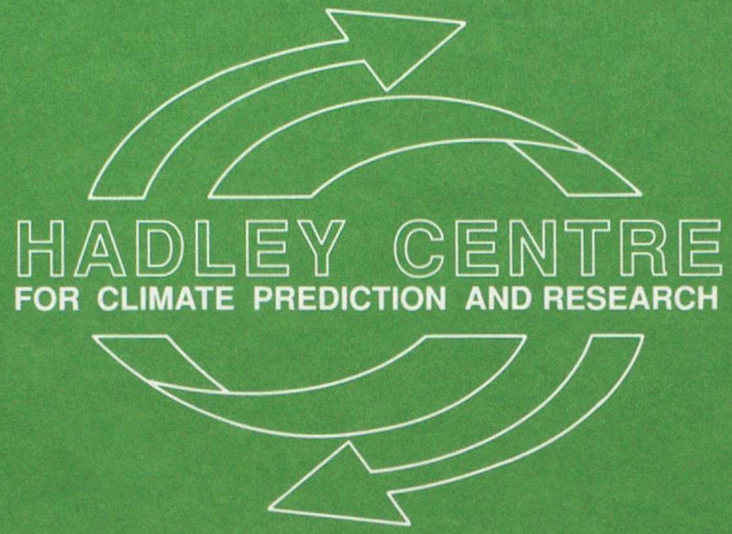

A tropical ocean model with reduced physics.

by

M. K. Davey

CRTN 29 **June 1992**

CLIMATE
RESEARCH
TECHNICAL
NOTE

Hadley Centre
Meteorological Office
London Road
Bracknell
Berkshire RG12 2SY

CLIMATE RESEARCH TECHNICAL NOTE NO. 29

A TROPICAL OCEAN MODEL WITH REDUCED PHYSICS

by

Michael Davey

Hadley Centre for Climate Research and Prediction
Meteorological Office
London Road
Bracknell
Berkshire RG12 2SY
U.K.

Note: This paper has not been published. Permission to quote from it should be obtained from the Director of the Hadley Centre.

A TROPICAL OCEAN MODEL WITH REDUCED PHYSICS

Michael K. Davey
Meteorological Office Unit, Robert Hooke Institute
Clarendon Laboratory, Parks Road, Oxford OX1 3PU, UK

Summary

A tropical upper ocean model with two active layers and simplified physics is described. The aim is to construct a model that can produce reasonably realistic large-scale currents and sea surface temperatures on seasonal to interannual timescales, and yet is easy to analyse and understand. Details of the model are documented here, and the model response to a windburst and to seasonal cycle forcing fields is described.

1. Introduction

El Niño Southern Oscillation (ENSO) events are interannual climate changes that involve close coupling between the atmosphere and oceans, predominantly in the tropical Pacific region. (See e.g. Philander (1990) for a detailed description.) Dynamical simulation and prediction of such events is the major goal of the UK Meteorological Office Tropical Oceanography group, and of several other groups around the world. The work is carried out as part of the international Tropical Ocean Global Atmosphere (TOGA) modelling and observation programme.

Many different oceanic and atmospheric models are being used for ENSO studies, ranging from coupled general circulation models (GCMs) that attempt detailed realistic simulations to ordinary differential equations that demonstrate some elementary process in an idealised way. (See Neelin et al. 1991 for an intercomparison of several GCMs, and the review by McCreary & Anderson 1991.) The UKMO group uses both coupled GCMs (Gordon 1989) and models of intermediate complexity with reduced physics (Budin & Davey 1990).

The intermediate coupled model described in Budin & Davey (1990) included an oceanic component that was essentially the same as that used by Anderson & McCreary (1985), with a single active layer. Although that model could produce interannual oscillations, the oscillations were very robust and regular, unlike the observed behaviour, even when substantial 'noise' was added to the model atmosphere. Further, some fea-

tures such as ocean currents were not well reproduced. The defects can be partly attributed to the single-layer ocean structure, which effectively represented conditions averaged over the top 200 metres, so thermal inertia was large and surface and sub-surface currents were not separated. Such a model can represent integrated quantities such as upper ocean volume well (see e.g. Busalacchi et al. 1983), but is less accurate for other important quantities such as the sea surface temperature. Consequently the UKMO group decided to develop a multi-layer ocean for the next intermediate coupled model.

Several intermediate two-layer ocean models have already been developed with some success: for example, Cane et al. (1986) have used such a model in making skillful ENSO hindcasts and predictions. Their ocean model combines a fixed-depth surface layer with a variable- depth thermocline, using tuned linear long-wave dynamics and nonlinear thermodynamics (see Zebiak & Cane 1987 for details). McCreary & Kundu (1988) developed a nonlinear two-layer ocean model for the Indian Ocean, and Schopf & Suarez (1988) have used a similar model in coupled ocean-atmosphere experiments.

The dynamical model described here is based on the linearised shallow-water equations, as presented in section 2, with the depths of both active layers allowed to vary. A simple background temperature structure, constant in each layer, is used. The finite-difference scheme (section 4) is combined with a variable C-grid (section 3). The linear equatorial wave properties of the model are demonstrated by the windburst experiment described in section 5.

In practise layer depth variations are substantial, and these are limited by the simple *ad hoc* entrainment and detrainment algorithms given in section 6. These processes play an important part in the thermal balance of the model: in particular entrainment of cooler water into the upper layer where it is shallow offsets the surface heat flux into the ocean. The temperature equations in section 7 also include horizontal advection by the ocean currents.

The ocean response to the climatological surface heat flux in the absence of advection and entrainment is considered in section 8, using a linearised feedback term to achieve equilibrium. In section 9 climatological surface stress is added, and the model seasonal cycle is compared with observed behaviour. Note that the dynamical response of this model is separated from the thermodynamic response: the currents and layer depths are determined by the prescribed wind stress and background state alone, with no feedback from temperature variations.

One application of this model will be to couple it to various atmospheric models. In that case sea surface temperature changes will cause wind stress anomalies that in turn alter the ocean currents.

2. Basic dynamics

The response of a linear model can be analysed and understood in terms of classical equatorial waves, whereas a nonlinear model can be quite difficult to analyse. Indeed, it was the analysis by Battisti (1988) and Battisti & Hirst (1989) of the Cane & Zebiak model with linear dynamics and a simple domain that led to its successful interpretation in terms of a simple delayed- oscillator mechanism. Thus we decided to adopt a basically linear dynamical structure for the new two-layer model. For simplicity equatorial beta-plane geometry is used, with co-ordinates x eastward and y northward, and the equator at y=0. The various physical constants that appear in the equations below are listed in Table I at the end of this section.

The vertical structure, with layer depths h_1 and h_2, is illustrated in Fig. 2.1 . The model is linearised about a state of rest, with mean layer depths $\bar{h}_1$ and $\bar{h}_2$, and mean temperatures $\bar{T}_1$ and $\bar{T}_2$. The passive deep layer below layer 2 has fixed temperature $\bar{T}_3$. Salinity effects are ignored in the equation of state, which is linearised to

$$\rho = \rho_o[1 - \alpha(T - T_o)] \quad , \tag{2.1}$$

where ρ is density, α is the constant thermal expansion coefficient, and ρ_o and T_o are reference values. Through the hydrostatic relation

$$\frac{\partial p}{\partial z} = -\rho g \tag{2.2}$$

the pressure p is determined by the layer depths and densities. Although temperature can vary horizontally within each layer in this model (see below), for simplicity such temperature variations (i.e. perturbations from $\bar{T}$) are ignored when calculating horizontal pressure gradients. Further, the horizontal pressure gradient is taken to be zero in a motionless passive deep third layer. With these assumptions we have

$$\frac{1}{\rho_0}\nabla p_1 = g\alpha[(\bar{T}_1 - \bar{T}_2)\nabla h_1 + (\bar{T}_2 - \bar{T}_3)\nabla(h_1 + h_2)] \quad , \tag{2.3}$$

$$\frac{1}{\rho_0}\nabla p_2 = g\alpha(\bar{T}_2 - \bar{T}_3)\nabla(h_1 + h_2) \quad . \tag{2.4}$$

The displacement of the free surface η provides the pressure gradient in layer 1. It can be diagnosed as

$$\eta = \alpha(\bar{T}_2 - \bar{T}_3)(h_1 + h_2 - \bar{h}_1 - \bar{h}_2) + \alpha(\bar{T}_1 - \bar{T}_2)(h_1 - \bar{h}_1) \quad . \tag{2.5}$$

The pressure gradients, and the wind stress applied to the upper layer, drive the ocean currents. The momentum equations are

$$\frac{\partial \underline{u}_1}{\partial t} + f\underline{k} \times \underline{u}_1 = -\frac{1}{\rho_0}\nabla p_1 + A_m \nabla^2 \underline{u}_1 - d_1(\underline{u}_1 - \underline{u}_2) - d_{ns}\underline{u}_1 + \frac{\underline{\tau}}{\rho_0 \bar{h}_1} \quad , \tag{2.6}$$

$$\frac{\partial \underline{u}_2}{\partial t} + f\underline{k} \times \underline{u}_2 = -\frac{1}{\rho_0}\nabla p_2 + A_m \nabla^2 \underline{u}_2 + d_2(\underline{u}_1 - \underline{u}_2) - d_{ns}\underline{u}_2 \quad . \tag{2.7}$$

The lateral momentum dissipation coefficient A_m varies according to the grid size, taking values as small as numerical stability will allow. The constant vertical momentum exchange coefficients d_j are also weak. The damping term d_{ns} only acts near the closed northern and southern boundaries, to suppress coastal waves (see section 3.1). The Coriolis parameter on the equatorial beta-plane is

$$f = \beta y \quad . \tag{2.8}$$

Equations for the layer depths are

$$\frac{\partial h_1}{\partial t} + \bar{h}_1 \nabla . \underline{u}_1 = w_{e1} + w_{d1} \quad , \tag{2.9}$$

$$\frac{\partial h_2}{\partial t} + \bar{h}_2 \nabla . \underline{u}_2 = -w_{e1} - w_{d1} + w_{e2} + w_{d2} \quad . \tag{2.10}$$

The positive terms w_{e1} (mass entrainment from layer 2 into layer 1) and w_{e2} (entrainment from the deep ocean into layer 2) are used to represent upwelling. They act only when a layer depth is less than some critical value, and they limit the shallowing of each layer. Similarly, negative detrainment terms w_{d1} and w_{d2} are active when layer depths tend to become too large. Details of the entrainment/detrainment algorithm are given in section 6. In the absence of entrainment and detrainment, the dynamical system is linear.

These equations control a wind-driven circulation that is independent of any thermal changes. When the wind stress, dissipation and entrainment terms are neglected the linear equations can easily be solved to determine the structure and speeds of the first and second baroclinic modes, as described in appendix A. With the same terms neglected the following energy conservation relation can be derived:

$$\partial(< KE > + < PE >)/\partial t = 0 \quad , \tag{2.11}$$

where

$$KE = [\bar{h}_1({u_1}^2 + {v_1}^2) + \bar{h}_2({u_2}^2 + {v_2}^2)]/2 \quad , \tag{2.12}$$

$$PE = \alpha g[(\bar{T}_1 - \bar{T}_2){h_1}^2 + (\bar{T}_2 - \bar{T}_3)(h_1 + h_2)^2]/2 \quad , \tag{2.13}$$

and <> denotes an average over the area of the ocean basin. In the absence of entrainment mass is also conserved in each layer:

$$< h_1 >= \bar{h}_1 \quad , \quad < h_2 >= \bar{h}_2 \quad . \tag{2.14}$$

Table I: Ocean model parameters

$\bar{T}_1 = 28°C$	$\bar{T}_2 = 20°C$	$\bar{T}_3 = 12°C$
$\bar{h}_1 = 100m$	$\bar{h}_2 = 150m$	
$c_+ = 2.43\ m\ sec^{-1}$	$c_- = 0.99\ m\ sec^{-1}$	
$h_{1e} = 40\ m$	$h_{2e} = 40\ m$	$h_d = 700\ m$
$d_1 = (200\ day)^{-1}$	$d_2 = (\bar{h}_1/\bar{h}_2)d_1$	$d_{nso} = (5\ day)^{-1}$
$A_{mo} = 2000\ m^2 sec^{-1}$	$A_T = 2000\ m^2 sec^{-1}$	
$\rho_o = 1000\ Kg\ m^{-3}$	$\alpha = 2.5\text{x}10^{-4}$	$c_p = 4 \times 10^{-3}\ J\ °K^{-1}\ Kg^{-1}$
$\beta = 2.28 \times 10^{-11}\ m^{-1} sec^{-1}$	$\Delta t = 7200\ sec$	

3. The variable grid

3.1 Grid layout

To resolve the important equatorial waveguide and upwelling regions it is desirable to have high horizontal resolution there, and to save computation time it is common to use lower resolution elsewhere by adopting a variable grid. For example, the grid used for the present UKMO tropical Pacific ocean GCM is shown in Fig. 3.1a: near the equator meridional resolution is 1/3°, increasing to 1° at the northern and southern boundaries near 30°N and 30°S. For this GCM there is enhanced zonal resolution near the east and west coasts also, to better represent boundary currents and upwelling. In the interior the zonal resolution is 1.5°, decreasing to 0.54° at the eastern and western boundaries. The GCM uses a B-grid arrangement for the model variables, as shown in Fig. 3.2a, with temperature points centred between velocity points, and with velocity points placed along the equator.

A similar variable grid is adopted for the two-layer model, but with the C-grid arrangement (Fig. 3.2b) that is commonly used for layer models. (The C-grid allows accurate calculation of the divergence term that controls layer depth variations.) The naming convention used (in the text below and in the program code) for the location of points and their separations is included in Fig. 3.2b (note that these definitions differ in some respects from the convention used in the GCM). Depth and temperature variables are located at h-points (XH_i, YH_j), zonal velocities at u-points (XU_i, YU_j), and meridional velocities at v-points (XV_i, YV_j).

Depth and temperature points are centred between velocity points because this allows easy calculation of fluxes and budgets. Thus

$$XH_i = \frac{1}{2}(XU_i + XU_{i-1}) \quad , \tag{3.1}$$

$$YH_j = \frac{1}{2}(YV_j + YV_{j-1}) \quad . \tag{3.2}$$

The distances between points are denoted

$$DXU_i = XU_{i+1} - XU_i \quad , \tag{3.3}$$

$$DYV_j = YV_{j+1} - YV_j \quad , \tag{3.4}$$

$$DXH_i = XH_{i+1} - XH_i = \frac{1}{2}(DXU_{i-1} + DXU_i) \quad , \tag{3.5}$$

$$DYH_j = YH_{j+1} - YH_j = \frac{1}{2}(DYV_{j-1} + DYV_j) \ . \qquad (3.6)$$

Note that $DYU_j = DYH_j$ and $DXV_i = DXH_i$.

The variable grid is defined by the locations XU_i and YV_j. Algorithms for calculating suitable values of these points are given in appendix B: they are based on those developed by Dr Gordon for the UKMO tropical Pacific Ocean GCM.

The Pacific ocean domain chosen for the two-layer model differs slightly from that for the ocean GCM, in that it is based on the region used for the Florida State University (FSU) tropical Pacific pseudostress dataset. [The FSU dataset is a subjectively-analysed dataset (Goldenberg & O'Brien 1981) that provides monthly-average values from 1961 to the present, on a $2° \times 2°$ latitude-longitude grid.] This particular domain was chosen for convenience; other domains can be easily used.

In initial experiments with the two-layer model a grid with the same resolution as the ocean GCM was used. Several variations were then tested, using short windburst experiments (see section 5) for comparison. The version used for the experiments described in this Technical Note is shown in Fig. 3.1b: the meridional resolution is half that of the GCM, and uniform 1.5° zonal resolution is used, with $IDIM \times JDIM = 113 \times 47$ gridpoints. (By comparison, the ocean GCM has 134×94 points. For the windburst tests, the results with 113×47 points were essentially the same as those obtained using the finer GCM resolution.)

The two-layer model and ocean GCM domains differ in another important respect: the GCM has open northern and southern boundaries, with a relaxation-to-climatology buffer zone, whereas the two-layer model has closed boundaries. To prevent coastal Kelvin waves sending information along those artificial boundaries an extra velocity damping term with coefficient d_{ns} was added, with

$$d_{ns} = d_{ns0} \begin{cases} (6-j)/4 & j=2,...,5 \\ 0 & \text{otherwise} \\ (j+5-JDIM)/4 & j = JDIM-4,...,JDIM-1 \end{cases} \qquad (3.7)$$

where $JDIM$ is the number of meridional points.

3.2 Coasts and land/sea masks

Land and sea points on the grids are defined by setting masks as follows. The integer mask array $MASKH$ for h-points (and T-points) is determined first by

$$MASKH_{ij} = \begin{cases} 1 & \text{ocean} \\ 0 & \text{land} \end{cases} \qquad (3.8)$$

The coast is made up of zonally- and meridionally-aligned sections. U-points are placed on meridionally-aligned sections (where u=0), and v-points are placed on zonally-aligned sections (where v=0). An example of coastal position is given in Fig 3.3 .

Masks for u-points and v-points are determined by $MASKH$, according to

$$MASKU_{ij} = MASKH_{ij}\ MASKH_{i+1j} \quad , \tag{3.9}$$

$$MASKV_{ij} = MASKH_{ij}\ MASKH_{ij+1} \quad . \tag{3.10}$$

Thus $MASKU$ and $MASKV$ are zero at land points and on coasts, and unity at ocean points.

4. The finite-difference scheme

4.1 Derivatives

Using the notation introduced in section 3, spatial derivatives of h at u- and v-points respectively take the form

$$(h_x)_{ij} = \frac{h_{i+1j} - h_{ij}}{DXH_i} \quad , \tag{4.1}$$

$$(h_y)_{ij} = \frac{h_{ij+1} - h_{ij}}{DYH_j} \quad . \tag{4.2}$$

Similarly, derivatives of u and v at h-points are

$$(u_x)_{ij} = \frac{u_{ij} - u_{i-1j}}{DXU_{i-1}} \quad , \tag{4.3}$$

$$(v_y)_{ij} = \frac{v_{ij} - v_{ij-1}}{DYV_{j-1}} \quad . \tag{4.4}$$

4.2 Coriolis terms

The Coriolis terms are somewhat awkward and ambiguous on a C-grid, because the u- and v-points do not coincide. To choose from the various possibilities a scheme was selected that would satisfy the finite difference form of the global energy conservation equation (2.11), as described in appendix C. For the Coriolis terms to cancel in this equation we require at u- points

$$\begin{aligned}(fv)_{ij} = \big(&f_j^+[v_{ij}DXU_{i-1} + v_{i+1j}DXU_i] + \\ &f_j^-[v_{ij-1}DXU_{i-1} + v_{i+1j-1}DXU_i]\big) \\ &/(4DXH_i) \quad ,\end{aligned} \tag{4.5}$$

and at v-points

$$\begin{aligned}(fu)_{ij} = \big(&f_j^+[u_{i-1j} + u_{ij}]DYV_{j-1} + \\ &f_{j+1}^-[u_{ij} + u_{i+1j}]DYV_j\big) \\ &/(4DYH_j) \quad ,\end{aligned} \tag{4.6}$$

where

$$f_j^+ = \beta\,(YH_j + DYV_{j-1}/4) \quad , \tag{4.7}$$

$$f_j^- = \beta\,(YH_j - DYV_{j-1}/4) \quad . \tag{4.8}$$

4.3 Temperature advection

Temperature advection terms at ocean T-points ij are calculated using the centred-difference forms

$$(uT_x)_{ij} = \frac{1}{2}\left[u_{ij}\frac{T_{i+1j} - T_{ij}}{DXH_i} + u_{i-1j}\frac{T_{ij} - T_{i-1j}}{DXH_{i-1}}\right] , \tag{4.9}$$

$$(vT_y)_{ij} = \frac{1}{2}\left[v_{ij}\frac{T_{ij+1} - T_{ij}}{DYH_j} + v_{ij-1}\frac{T_{ij} - T_{ij-1}}{DYH_{j-1}}\right] . \tag{4.10}$$

These forms are the average of advection at neighbouring velocity points. A simple average is used because the T-points are centred between the neighbouring u- and v-points. Note that boundary conditions on T need not be taken into account because $u = 0$ on meridionally-aligned coasts and $v = 0$ on zonally-aligned coasts.

4.4 Velocity boundary conditions

Only closed boundaries are considered here. Boundary conditions of no flow normal to coasts are maintained by multiplying the u and v fields by the respective masks defined in section 3. Other boundary conditions can be incorporated into the finite-difference form of the Laplacian diffusion terms. Without taking boundaries into account the finite-difference Laplacian velocity terms are as follows. At ocean u-points ij in each layer

$$\frac{\partial^2 u}{\partial x^2}_{ij} = \frac{\left[\frac{(u_{i+1j} - u_{ij})}{DXU_i} - \frac{(u_{ij} - u_{i-1j})}{DXU_{i-1}}\right]}{(DXU_i + DXU_{i-1})/2} , \tag{4.11}$$

$$\frac{\partial^2 u}{\partial y^2}_{ij} = \frac{\left[\frac{(u_{ij+1} - u_{ij})}{DYU_j} - \frac{(u_{ij} - u_{ij-1})}{DYU_{j-1}}\right]}{(DYU_j + DYU_{j-1})/2} . \tag{4.12}$$

At v-points in each layer,

$$\frac{\partial^2 v}{\partial x^2}_{ij} = \frac{\left[\frac{(v_{i+1j} - v_{ij})}{DXV_i} - \frac{(v_{ij} - v_{i-1j})}{DXV_{i-1}}\right]}{(DXV_i + DXV_{i-1})/2} , \tag{4.13}$$

$$\frac{\partial^2 v}{\partial y^2}_{ij} = \frac{\left[\frac{(v_{ij+1} - v_{ij})}{DYV_j} - \frac{(v_{ij} - v_{ij-1})}{DYV_{j-1}}\right]}{(DYV_j + DYV_{j-1})/2} . \tag{4.14}$$

Problems arise if a u- or v-point is used which is not in the ocean or on the coast. For the grid layout described in section 3 this situation does not occur for (4.11) and (4.14), but (4.12) and (4.13) need to be modified near coasts. We consider both free-slip and no-slip boundary conditions, and use the masks to incorporate these conditions into the Laplacian forms.

(a) no-slip boundary: u=v=0 on all coasts.

Suppose there is a zonally-aligned coast between the ocean u-point ij and the u-point $i, j+1$ (i.e. $MASKU_{ij} = 1$ and $MASKU_{ij+1} = 0$). Then, by linear interpolation,

$$u_{coast} = 0 = u_{ij} + \frac{DYV_{j-1}}{2} \frac{u_{ij+1} - u_{ij}}{DYU_j} \quad , \tag{4.15}$$

which implies

$$\frac{u_{ij+1} - u_{ij}}{DYU_j} = -\frac{2u_{ij}}{DYV_{j-1}} \quad . \tag{4.16}$$

Similarly for a coast between the u-points $i, j-1$ and ij (i.e. $MASKU_{ij} = 1$ and $MASKU_{ij-1} = 0$) we use

$$u_{coast} = 0 = u_{ij} - \frac{DYV_{j-1}}{2} \frac{u_{ij} - u_{ij-1}}{DYU_{j-1}} \quad , \tag{4.17}$$

which implies

$$\frac{u_{ij} - u_{ij-1}}{DYU_{j-1}} = \frac{2u_{ij}}{DYV_{j-1}} \quad . \tag{4.18}$$

Using (4.16) and (4.18) and $MASKU$, (4.12) can be put in a form that covers all possibilities by replacing the numerator [ ] by:

$$\left[\frac{(u_{ij+1} - u_{ij})}{DYU_j} MASKU_{ij+1} - \frac{(u_{ij} - u_{ij-1})}{DYU_{j-1}} MASKU_{ij-1} + \frac{2u_{ij}}{DYV_{j-1}} (MASKU_{ij+1} + MASKU_{ij-1} - 2)\right] \quad . \tag{4.19}$$

Similarly (4.13) can be modified to include cases adjacent to meridionally-aligned coasts by replacing [ ] by

$$\left[\frac{(v_{i+1j} - v_{ij})}{DXV_i} MASKV_{i+1j} - \frac{(v_{ij} - v_{i-1j})}{DXV_{i-1}} MASKV_{i-1j} + \frac{2v_{ij}}{DXU_{i-1}} (MASKV_{i+1j} + MASKV_{i-1j} - 2)\right] \quad . \tag{4.20}$$

(b) free-slip boundaries

On meridionally-aligned free-slip coasts v can be non-zero but $v_x = 0$, and on zonally-aligned coasts u can be non-zero but $u_y = 0$. These free-slip boundary conditions can also be incorporated into the Laplacian terms. If a zonally-aligned coast lies between u_{ij} and u_{ij+1} ($MASKU_{ij+1} = 0$) then we require

$$\frac{u_{ij+1} - u_{ij}}{DYU_j} = 0 \quad . \tag{4.21}$$

Likewise, if $MASKU_{ij-1} = 0$ then

$$\frac{u_{ij} - u_{ij-1}}{DYU_{j-1}} = 0 \quad . \tag{4.22}$$

Then (4.12) can be modified to take this into account by replacing [ ] by

$$\left[\frac{u_{ij+1} - u_{ij}}{DYU_j} MASKU_{ij+1} - \frac{u_{ij} - u_{ij-1}}{DYU_{j-1}} MASKU_{ij-1}\right] \quad . \tag{4.23}$$

Similarly, (4.13) can be modified by replacing [ ] by

$$\left[\frac{v_{i+1j} - v_{ij}}{DXV_i} MASKV_{i+1j} - \frac{v_{ij} - v_{i-1j}}{DXV_{i-1}} MASKV_{i-1j}\right] \quad . \tag{4.24}$$

Again, (4.11) and (4.14) need not be adjusted.

4.5 Variable diffusivity

The momentum diffusivity coefficient A_m is allowed to vary as the grid spacing changes, increasing where resolution is coarser. In this model the variation used at u-points ij is

$$A_m = A_{mo} \frac{DXU_i + DXU_{i-1}}{2\, DXU_{mid}} \frac{DYU_j + DYU_{j-1}}{2\, DYU_{eq}} \tag{4.25}$$

where DXU_{mid} is the zonal spacing in the mid-Pacific, and DYU_{eq} is the meridional spacing in the high-resolution equatorial belt. A corresponding form is used at v-points. Note that the terms $(DXU_i + DXU_{i-1})/2$ etc. cancel when A_m multiplies the finite-difference Laplacian forms in the preceding section.

4.6 Temperature boundary conditions

The Laplacian of temperature T at T-points ij is

$$\frac{\partial^2 T}{\partial x^2}_{ij} = \frac{\frac{(T_{i+1j} - T_{ij})}{DXH_i} - \frac{(T_{ij} - T_{i-1j})}{DXH_{i-1}}}{(DXH_i + DXH_{i-1})/2} , \tag{4.26}$$

$$\frac{\partial^2 T}{\partial y^2}_{ij} = \frac{\frac{(T_{ij+1} - T_{ij})}{DYH_j} - \frac{(T_{ij} - T_{ij-1})}{DYH_{j-1}}}{(DYH_j + DYH_{j-1})/2} . \tag{4.27}$$

When diffusivity is included in the system, the derivative of T normal to coasts should be set to zero to prevent heat exchange across boundaries . To take this condition into account the above Laplacian terms are modified to

$$\frac{\partial^2 T}{\partial x^2}_{ij} = \frac{\frac{(T_{i+1j} - T_{ij})MASKH_{i+1j}}{DXH_i} - \frac{(T_{ij} - T_{i-1j})MASKH_{i-1j}}{DXH_{i-1}}}{(DXH_i + DXH_{i-1})/2} , \tag{4.28}$$

$$\frac{\partial^2 T}{\partial y^2}_{ij} = \frac{\frac{(T_{ij+1} - T_{ij})MASKH_{ij+1}}{DYH_j} - \frac{(T_{ij} - T_{ij-1})MASKH_{ij-1}}{DYH_{j-1}}}{(DYH_j + DYH_{j-1})/2} . \tag{4.29}$$

4.7 Layer depth boundary conditions

For the system described in this Technical Note there is no Laplacian term in the layer depth equations. If such terms are included then boundary conditions can be treated as follows. When no-slip velocity conditions are used then the derivative of h normal to coasts should be zero: in this case the appropriate Laplacian forms are (4.28) and (4.29) with h replacing T.

If free-slip velocity conditions are used then the boundary conditions on h are $\partial^2 h/\partial x^2 = 0$ on meridionally-aligned coasts and $\partial^2 h/\partial y^2 = 0$ on zonally-aligned coasts. Convenient approximate forms for the Laplacian are

$$\frac{\partial^2 h}{\partial x^2}_{ij} = \frac{\left(\frac{h_{i+1j} - h_{ij}}{DXH_i} - \frac{h_{ij} - h_{i-1j}}{DXH_{i-1}}\right)MASKH_{i+1j}MASKH_{i-1j}}{(DXH_i + DXH_{i-1})/2} , \tag{4.30}$$

$$\frac{\partial^2 h}{\partial y^2}_{ij} = \frac{\left(\frac{h_{ij+1} - h_{ij}}{DYH_j} - \frac{h_{ij} - h_{ij-1}}{DYH_{j-1}}\right)MASKH_{ij+1}MASKH_{ij-1}}{(DYH_j + DYH_{j-1})/2} . \tag{4.31}$$

4.8 The time stepping algorithm

The basic timestep unit is Δt. Starting from some known conditions at time t the state of the system (S say) is first stepped using the predictor-corrector sequence

$$S(t + \Delta t/2) = S(t) + Strend(t)\ \Delta t/2 \quad , \tag{4.32}$$

$$S(t + \Delta t) = S(t) + Strend(t + \Delta t/2)\ \Delta t \quad , \tag{4.33}$$

where $Strend(t)$ is the rate-of-change evaluated using $S(t)$.

Leapfrog steps are used following the initial predictor-corrector:

$$S(t + 2\Delta t) = S(t) + Strend(t + \Delta t)\ 2\Delta t \quad . \tag{4.34}$$

(Diffusive terms in *Strend* are here evaluated at time t.)

To prevent time-splitting instability, after a certain number of steps (101 for the experiments described here) data at successive times $t - \Delta t$ and t are averaged to obtain $S(t - \Delta t/2)$. A forward step of length $\Delta t/2$ is then taken to obtain initial conditions $S(t)$ for a new predictor-corrector and leapfrog sequence. For convenience, a 360-day year is used.

5. The response to a wind burst

In this section an experiment is described that demonstrates the wavelike properties of the dynamical part of the model. The system is initially at rest, and at time t_0 a westerly wind burst is added to force an equatorial region near the dateline. Entrainment/detrainment mechanisms do not act because the layer depth perturbations are small in this experiment, so the dynamical response of the ocean is linear. Ocean model parameters are as listed in Table I.

5.1 The wind burst

Westerly wind bursts that last several days are common features in the western Pacific. (See e.g. Keen (1982), McPhaden et al. (1988), Murakami & Sumathilapa (1989), Delcroix et al. (1991).) For this experiment a zonal wind burst is used of the form

$$\tau^{(x)} = A(t)\rho_a C_d U|U| \quad , \quad \tau^{(y)} = 0 \quad , \tag{5.1}$$

where

$$U(x,y) = U_o e^{-[(x-x_o)/(x_2-x_0)]^2} \; e^{-[(y-y_o)/(y_2-y_0)]^2} \tag{5.2}$$

in a rectangular region $x_1 < x < x_2$, $y_1 < y < y_2$ centred on (x_0, y_0), and

$$A(t) = \begin{cases} (t-t_0)/(t_1-t_0) & t_0 < t \le t_1 \\ 1 & t_1 < t \le t_2 \\ (t_3-t)/(t_3-t_2) & t_2 < t \le t_3 \\ 0 & \text{otherwise} \end{cases} \quad . \tag{5.3}$$

The linear ramp form for $A(t)$ and the Gaussian spatial dependence are used to reduce the generation of strong vertical motion and inertia-gravity waves. Forcing parameters are listed in Table II below. These provide a westerly burst lasting 10 days, located west of the dateline, as shown in Fig. 5.1 .

Table II: windburst parameters

$U_o = 5m\ sec^{-1}$	$\rho_a = 1.3Kg\ m^{-3}$	$C_d = 0.001$
$x_1 = 150°E$	$x_2 = 180°E$	$x_0 = 165°E$
$y_1 = -10°$	$y_2 = 10°N$	$y_0 = 0°$
$t_0 = 0$	$t_1 = 2\ days$	
$t_2 = 8\ days$	$t_3 = 10\ days$	

The strength of the burst is modest, with a maximum stress of $0.0325N\ m^{-2}$. Note that the ocean perturbations scale with the square of U_o, and change sign if the wind is easterly rather than westerly.

5.2 Wave generation

The westerly burst directly forces an eastward current in the upper layer in the forced region, causing convergence (divergence) at the western (eastern) end of the region. Coriolis effects also cause equatorward turning of the current, leading to convergence around the equator. This convergence in turn forces displacement of the layer interfaces and the generation of horizontal pressure gradients: gravitational restoring forces in the statically stable system then give rise to wave motions.

The burst drives equatorially trapped Kelvin and Rossby waves which propagate zonally away from the forced region, plus higher frequency inertial-gravity waves which largely remain in the vicinity of the burst. The Kelvin and Rossby waves later reflect from the east and west coasts, generating further waves. (See e.g. Philander (1990) chapter 3, or Gill (1982) chapter 11 for detailed descriptions of these waves.)

5.3 The x-t view along the equator

Figs. 5.2 - 5.4 show time-longitude sections of several quantities along the equator. The zonal velocity u_1 (Fig. 5.2a) is locally accelerated by the burst to a maximum of $16cm\ sec^{-1}$ during the first few days, while layer 1 deepens by up to $7m$ (Fig. 5.3a). There is little change in u_2 (Fig. 5.2b) or in the depth $h_1 + h_2$ of the interface between layer 2 and the deep ocean (Fig. 5.3b).

Several distinct waves can be seen travelling across the Pacific in the following months. The fastest is the eastward-propagating first baroclinic Kelvin wave (denoted K_+), which takes about two months to travel from the dateline to the South American coast. It is associated with eastward u_1 and u_2 of similar magnitude, and downward bulges in h_1 and $h_1 + h_2$ (a 'downwelling' Kelvin wave). (Remember that the sign of the perturbations is changed for an easterly burst, which would directly drive an 'upwelling' K_+ wave.) The propagation speed of the K_+ wave is about $2.4m\ sec{-}1$, in good agreement with the inviscid prediction in Appendix A.

On reaching the east coast, the K_+ signal is reflected as Rossby waves. The fastest Rossby wave (denoted R_+) travels westward with one-third the speed of K_+, and in this case is associated with westward currents and deeper h_1 and h_1+h_2. The reflected signal is relatively weak: this is partly because the K_+ wave also generates coastal waves, and

partly because Rossby waves have their maximum depth signal off the equator (see the x-y view below).

After the wind burst, the second baroclinic mode Kelvin wave (K_-) can also be seen leaving the forced region, at a slower speed of about $1m\ sec^{-1}$. Zonal velocity is eastward in layer 1, but westward in layer 2; and h_1 is deepened while $h_1 + h_2$ has an upward bulge. After four months K_- crosses the path of the westward R_+ wave from the east coast, and at this time the amplitude of u_2 is reinforced but u_1 is reduced. After nearly six months K_- reflects from the eastern boundary, generating further coastal and Rossby waves.

As well as the Kelvin waves east of the windburst region, weaker Rossby waves propagate westward from that region, to encounter the west 'coast'. (In practise this boundary is not solid but contains straits and shallow seas.) The Rossby waves reflect as symmetric Kelvin, anti-symmetric Yanai, and short slow Rossby waves. The reflected signal is weak, partly because the irregular shape of the western boundary acts to smear out the incident signal and partly due to dissipative effects.

The separate + and − modes are more clearly emphasised in Fig. 5.4: $\bar{u} = (\bar{h}_1 u_1 + \bar{h}_2 u_2)/(\bar{h}_1 + \bar{h}_2)$ is dominated by the faster + mode (Fig. 5.4a), while $\hat{u} = u_1 - u_2$ is dominated by the − mode. (A more precise decomposition into + and − modes could be made by using the structure described in Appendix A.)

5.4 The x-y view

Fig. 5.5 shows fields for η, $h_1' = h_1 - \bar{h}_1$, and $(h_1 + h_2)' = h_1 + h_2 - (\bar{h}_1 + \bar{h}_2)$, every 30 days for the first six months of the experiment: Fig. 5.6 shows $\underline{u}_1$, $\underline{u}_2$ and w_1 for the same times. Kelvin waves appear as elliptical bulges in the depth perturbations, with corresponding elliptical patches of zonal currents, symmetric about the equator and largest on the equator. By contrast, Rossby waves characteristically have paired bulges in the depth fields with extrema either side of the equator. The currents for the north-south symmetric Rossby waves are similar to those of the Kelvin waves, being strongest on the equator, but they are less zonal off the equator.

By day 30 (Figs. 5.5a, 5.6a) Kelvin and Rossby waves are emerging from the windburst region. Following the westerly burst, currents in the upper layer are eastward and concentrated along the equator. In layer 2 currents are also eastward, except near the dateline where westward flow is associated with the slower K_- Kelvin wave. In the forced region itself behaviour is more erratic due to the inertial oscillations generated by the burst. (Note the strong and changing w_1 signal there.)

At day 60 (Figs. 5.5b, 5.6b) the K_+ and K_- waves are distinct, located at about

270° and 210° respectively. (Note how these non-dispersive waves travel with little attenuation or change of shape.) The K_+ wave is just reaching the east coast at day 60, and by day 90 it has reflected from that coast. The R_+ Rossby wave is clearly marked by the paired downward bulges in the depth fields near the east coast at day 90 (Fig. 5.5c), and by that time layers 1 and 2 have been deepened along the coast by coastally-trapped waves spreading poleward. The corresponding R_+ current is westward in both layers, while the coastal currents are equatorward (Fig. 5.6c).

The eastward-propagating R_+ and westward K_- waves have met at day 120: their respective patterns simply superimpose in this linear system, with the currents tending to cancel in layer 1 and reinforce in layer 2. By day 150 K_- is reflecting from the east coast, and the reflected R_- wave can be clearly seen in the h_1' field at day 180. Higher meridional Rossby modes have also appeared by days 150 and 180, being particularly evident in the $(h_1 + h_2)'$ fields.

To the east of the forced region Rossby waves impinge on the west coast at about day 60: the change in current on the equator at about 130° from eastward (day 60) to westward (day 90) is an indication of R_+ reflecting as K_+. The K_+ wave is quite weak. One factor affecting the reflected wave strength is the coastline shape, which causes an incident wave to reflect south of the equator well before it reflects north of the equator. The zonal extent of the incident wave is relevant: shorter waves (such as that generated by the burst in this example) are more affected by the coastal shape than longer waves. Another factor is the enhanced dissipation associated with the small-scale flow near the west coast.

6. Entrainment and detrainment

In response to an easterly wind stress the model upper layer deepens in the west Pacific and becomes more shallow in the east Pacific, as a pressure gradient is set up to oppose the wind stress. (Recall that, by hydrostatic balance, the layer depth changes reflect small surface displacements that actually provide the pressure gradient.) In the absence of entrainment (i.e. mass exchange between the layers) the layer depths could vanish, which is a situation that the numerical scheme cannot handle. In practice, vanishing of the 'upper layer depth' (surfacing of the thermocline in the OGCM) is prevented by turbulent mixing, which is represented in the GCM by a combination of Richardson-number dependent vertical diffusivity (Pacanowski & Philander 1981) and bulk mixing (cf Kraus & Turner 1967). A similar scheme could be implemented for the present two-layer model (and may be desirable in the future), but at present a much simpler *ad hoc* method is used that depends only on the layer depths and tendencies.

When the depth of a layer tends to be less than some critical value h_e then entrainment from the layers above and/or below is initiated, to prevent the layer becoming too shallow. Similarly, when the net depth of the active layers exceeds some other critical value h_d then detrainment to the deep ocean below is activated. (Note that entrainment into a layer is necessarily associated with detrainment from another.) The amount of entrainment is controlled by the choice of h_e etc.. The simple three-stage algorithm described below is used to determine the amount of entrainment or detrainment.

6.1 Algorithm

Suppose the layer depths are predicted to be h_1^* and h_2^* after a timestep Δt, before applying the entrainment/ detrainment terms w_{e1} etc. in equs. (2.9) and (2.10).

Stage 1: is layer 1 too shallow?

If $h_1^* \leq h_{1e}$ then the depth of layer 1 is increased by an amount E_1, where

$$E_1 = \begin{cases} (h_{1e} - h_1^*)^2 / 2h_{1e} & h_1^* \text{ too shallow} \\ 0 & \text{otherwise} \end{cases}$$

$$= (\delta_{e1} + |\delta_{e1}|)^2 / 8h_{1e} \quad , \tag{6.1}$$

where

$$\delta_{e1} = h_{1e} - h_1^* \quad . \tag{6.2}$$

This formula is easy to implement numerically. Its form ensures that

$$0 \leq E_1 < h_{1e}/2 \quad , \tag{6.3}$$

and that E_1 increases smoothly and monotonically from zero as δ_{e1} increases above zero (i.e. as the shallowing tendency increases) - see Fig. 6.1. Correspondingly, the depth of layer 2 must be decreased by the same amount E_1. Note that this process does not change the total depth $h_1 + h_2$.

Stage 2: is layer 1 + layer 2 too deep?

If the bottom of layer 2 is becoming too deep (i.e. $h_1 + h_2 > h_d$) then the depth of layer 2 is decreased by an amount D_2, according to

$$D_2 = \begin{cases} (h_1^* + h_2^* - h_d)^2/2h_d & h_1^* + h_2^* \text{ too deep} \\ 0 & \text{otherwise} \end{cases}$$

$$= (\delta_{d2} + |\delta_{d2}|)^2/8h_d \quad , \tag{6.4}$$

where

$$\delta_{d2} = h_1^* + h_2^* - h_d \quad , \tag{6.5}$$

and D_2 is bounded by

$$0 \leq D_2 < h_d/2 \quad . \tag{6.6}$$

Stage 3: is layer 2 too shallow?

If layer 2 is now too shallow (i.e. $h_2^* - E_1 - D_2 < h_{2e}$) then its depth is increased by an amount $E_2 + D_1$, according to

$$E_2 + D_1 = \begin{cases} \delta_2^2/2h_{1e} & \text{layer 2 too shallow} \\ 0 & \text{otherwise} \end{cases}$$

$$= (\delta_2 + |\delta_2|)^2/8h_{1e} \quad , \tag{6.7}$$

where

$$\delta_2 = h_{2e} - h_2^* + E_1 + D_2 \quad . \tag{6.8}$$

As before,

$$0 \leq E_2 + D_1 < h_{1e}/2 \quad . \tag{6.9}$$

The increase is partitioned between detrainment D_1 from layer 1 to layer 2, and entrainment E_2 from the deeper ocean. The partitioning is achieved by first taking as

much as possible from layer 1 (without making it too shallow; i.e. h_1 must be greater than h_{1e}) by setting

$$D_1 = \min \left[(E_2 + D_1) \, , \, (|\delta_{e1}| - \delta_{e1})/2 \right] \quad . \tag{6.10}$$

This form ensures that if $\delta_{e1} < 0$ (i.e. layer 1 was already too shallow and was adjusted at stage 1) then $D_1 = 0$. The remainder is entrained from the deep ocean:

$$E_2 = (D_1 + E_2) \; - \; D_1 \quad . \tag{6.11}$$

After this process the new layer depths are

$$h_1 = h_1^* + E_1 - D_1 \quad , \tag{6.12}$$

$$h_2 = h_2^* - E_1 + D_1 + E_2 - D_2 \quad . \tag{6.13}$$

Thus during each timestep the entrainment/detrainment velocities in the layer depth equations (2.9) and (2.10) are effectively

$$w_{e1} = E_1/\Delta t \quad , \quad w_{d1} = -D_1/\Delta t \quad ,$$

$$w_{e2} = E_2/\Delta t \quad , \quad w_{d2} = D_2/\Delta t \quad . \tag{6.14}$$

Note that only one of E_1 and D_1 can be greater than zero at any one time. Note also that in the steady limit equ. (2.9) requires $w_{e1} = \bar{h}_1 \nabla . \underline{u}_1$ where entrainment occurs.

6.2 Alternative form

The entrainment term E_1 can be put into an alternative approximate form as follows. The difference between the estimate h_1^* after time Δt and the previous value h_1 is proportional to Δt, and is usually relatively small in practise, so (6.2) can be replaced by

$$\delta_{e1} = h_{1e} - h_1 \quad . \tag{6.15}$$

Then the entrainment velocity into the upper layer is

$$w_{e1} = \begin{cases} (h_{1e} - h_1)^2 / 2 h_{1e} \Delta t & h_1 \text{ too shallow} \\ 0 & \text{otherwise} \quad . \end{cases} \tag{6.16}$$

Such a quadratic form has been used directly in the layer depth equation (2.9) in similar ocean model by Anderson (private communication), with the term Δt in the denominator replaced by a longer fixed time scale.

7 Thermodynamics

7.1 Both layers thermodynamically active

The nonlinear thermodynamic equations used in this model are

$$\frac{\partial T_1}{\partial t} + (\bar{h}_1/h_1)\underline{u}_1.\nabla T_1 = \frac{Q}{\rho_0 c_p h_1} + A_T\nabla^2 T_1 + w_{e1}(T_2 - T_1)/h_1 \quad , \tag{7.1}$$

$$\frac{\partial T_2}{\partial t} + (\bar{h}_2/h_2)\underline{u}_1.\nabla T_2 = A_T\nabla^2 T_2 + w_{e2}(T_3 - T_2)/h_2 + w_{d1}(T_2 - T_1)/h_2 \quad , \tag{7.2}$$

where w_{e1}, w_{e2} and w_{d1} are entrainment/detrainment rates, Q is the net surface heat flux, and A_T is the diffusivity coefficient.

The unusual form of the horizontal advection terms stems from consideration of the conservation of heat. When combined with the linearised layer depth equations (2.9) and (2.10) the thermodynamic equations can be written in flux form as

$$\frac{\partial(h_1 T_1)}{\partial t} + \nabla.(\bar{h}_1 T_1 \underline{u}_1) = \frac{Q}{\rho_0 c_p} + dissipation + w_{e1}T_2 + w_{d1}T_1 \quad , \tag{7.3}$$

$$\frac{\partial(h_2 T_2)}{\partial t} + \nabla.(\bar{h}_2 T_2 \underline{u}_2) = dissipation - w_{e1}T_2 - w_{d1}T_1 + w_{e2}T_3 + w_{d2}T_2 \quad . \tag{7.4}$$

This form was chosen to conserve the total heat content $< h_1T_1 + h_2T_2 >$ of the two layers in the absence of Q, w_{e2}, w_{d2} and dissipation. It can be shown that the finite-difference forms of equations (2.9), (2.10), (7.1) and (7.2) have the same conservation property when the net heat content of a layer is defined as

$$< hT >= \sum_i \sum_j h_{ij} T_{ij} dA_{ij} \quad , \tag{7.5}$$

where

$$dA_{ij} = DXU_{i-1} DYV_{j-1}$$

and the sum is over interior (ocean) points. (Cf the energy conservation calculation in Appendix C.)

The advection form used can also be partially justified as follows. Owing to the linear form of the momentum and continuity equations, the velocity (u, v) is effectively forced over the depth $\bar{h}$; thus the velocity of advection of some quantity spread over a layer of depth h is effectively $(u, v)h/\bar{h}$.

In the numerical model the temperature adjustment due to entrainment and detrainment during a timestep is calculated such that the total heat content of a water

column is conserved in the process. The layer depths are updated first, with entrainment and detrainment terms E_1 etc. calculated as in section 6. Next the temperatures are predicted without entrainment and detrainment: suppose these are T_1^* and T_2^*. Then the temperatures after entrainment and detrainment are calculated, with

$$T_1 = T_1^* - (T_1^* - T_2^*)E_1/h_1 \quad , \tag{7.6}$$

$$T_2 = T_2^* - (T_2^* - \bar{T}_3)E_2/h_2 + (T_1^* - T_2^*)D_1/h_2 \quad , \tag{7.7}$$

where h_1 and h_2 are the updated layer depths. Thus layer 1 is cooled by entrainment E_1 of water from layer 2, and layer 2 can be cooled by entrainment E_2 from layer 3 or warmed by entrainment from layer 1. Note that

$$h_1T_1 + h_2T_2 = h_1^*T_1^* + h_2^*T_2^* - D_2T_2^* + E_2\bar{T}_3 \quad , \tag{7.8}$$

where h_1^* and h_2^* are the layer depths predicted before entrainment and detrainment (see (6.12) and (6.13)), so the heat content of the upper two layers is only altered by exchange with the deep third layer in this process, as required.

The final step in the adjustment process is to ensure static stability by mixing the two upper layers if $T_1 < T_2$, again preserving heat content. Thus

$$T_1 \rightarrow \max(T_1, \hat{T}) \quad , \tag{7.8}$$

$$T_2 \rightarrow \min(T_2, \hat{T}) \quad , \tag{7.9}$$

where

$$\hat{T} = (h_1T_1 + h_2T_2)/(h_1 + h_2) \quad . \tag{7.10}$$

A comment is needed on the form of the diffusive terms in (7.1) and (7.2) because, as stated, they do not strictly allow conservation of net heat content. Alternative forms that did strictly conserve net heat were tried, but they produced undesirable local temperature anomalies and were abandoned in favour of the simpler form used here. The resulting heat exchange is small by comparison with surface heat fluxes and entrainment effects in realistic simulations.

7.2 Only upper layer thermodynamically active

In climatological experiments with active temperature changes in both layers the model took a long time (decades) to reach reasonable equilibrium. A thermal damping

term with a time constant of O(years) was added to layer 2 to speed up the process, but results were very sensitive to the choice of time constant. (A long time constant allowed anomalies developed in the western Pacific to be advected in the Equatorial Undercurrent with little change, to be subsequently upwelled in the eastern Pacific and recycled. A short time constant tended to keep layer 2 too cool.) To obtain shorter equilibration times with reasonable climatology a different formulation was used for the climatological simulations described in section 9.

Equation (7.1) for the upper layer was retained, but T_2 was held constant in time with values approximating those obtained along the equator when T_2 was allowed to vary. Thus (7.2) was replaced by

$$T_2 = 25°\mathrm{C} - (x - 180)/80 \tag{7.11}$$

at longitude $x°E$. For layer 1 (and hence the sea surface temperature) the effect of this change is that water is always upwelled into layer 1 with this temperature.

8. Surface heat flux and static response

In this section the effect of a prescribed climatological heat flux is introduced, by first considering the response of the ocean model with no wind stress. Because dynamic and thermodynamic effects are separated, the ocean currents in this case remain at rest and the layer depths are not perturbed. The surface heat flux Q then simply heats up the upper layer locally. When contrasted with the case in section 9 with wind stress added, this example will help to identify regions where dynamical effects are important.

8.1 Forcing data

In practise various processes act to limit the change in ocean temperature, and Seager et al. (1988) describe a parameterisation of these effects. A simpler commonly-used form for the surface heat flux is to linearise these limiting processes about climatological values. We choose

$$Q = Q_c - \left(\frac{dQ}{dT}\right)_c (T_c - T_1) \quad , \tag{8.1}$$

where Q_c and surface temperature T_c are taken from the COADS monthly climatology and the climatological feedback rate $(dQ/dT)_c$ is as calculated by Oberhuber (1988).

Fig. 8.1 shows the seasonal cycle along the equator of Q_c and $(dQ/dT)_c$. Linearly interpolated monthly mean values are given. (Better interpolation methods exist - see Epstein (1991) - but the uncertainty of the monthly fields does not warrant their use.) Because $(dQ/dT)_c$ is negative everywhere the surface temperature is damped toward T_c. Its value is uncertain, and in many models it is simply given a constant value, typically $-35\ W\ m^{-2}\ °C^{-1}$. The surface flux Q_c is largest in the central-east Pacific (typically $100 W m^{-2}$) where T_c is low in the equatorial cold tongue and cloud cover is thin (but note the small Q_c next to the east coast in the second half of the year).

Maps of T_c in the Pacific region for Jan 1, Apr 1, Jul 1 and Oct 1 (linearly interpolated) are provided in Fig. 8.2: main features to note are the west Pacific warm pool and the equatorial cold tongue. Monthly mean maps of T_c, Q_c and $(dQ/dT)_c$ for individual months in the tropics can be found in Oberhuber (1988). The seasonal cycle of T_c along the equator is shown in Fig. 8.3a.

8.2 Static ocean response

Using the above thermal forcing, we solve (7.1) with $\underline{u}_1 = 0$ and $h_1 = \bar{h}_1$: i.e.

$$\frac{\partial T}{\partial t} = \frac{Q}{\rho_o c_p \bar{h}_1} + A_T \nabla^2 T \quad , \tag{8.2}$$

with standard parameters as in Table I. The resulting seasonal cycle of the temperature difference $T_1 - T_c$ along the equator is shown in Fig. 8.3b. Generally temperatures are too warm, as expected in the absence of any cooling upwelling mechanism. West of $210°E$ errors are mainly less than $1°C$, indicating that missing upwelling and advection effects are relatively unimportant in the west Pacific. Errors are much larger in the east Pacific ($> 4°C$ in places), and are largest where T_c is lowest in the equatorial cold tongue. Note that the diffusive term in (8.2) has only a small effect: if it is omitted then the maximum error increases by $0.15°C$.

Spatial maps of $T_1 - T_c$ are given in Fig. 8.4, every 90 days as in Fig. 8.2 . The difference is small in the west Pacific over a large area, whereas there are large positive errors in the east Pacific 'cold tongue' region, extending southward along the east coast. Negative errors occur near the artificial north and south boundaries, and in the south-east Pacific near the too-warm South American coast.

9. A seasonal cycle experiment

In this section an experiment with climatological forcing is described in detail. Ocean model parameters are as in Table I. Descriptions of typical observed tropical conditions can be found in books by e.g. Gill (1982), Philander (1990), and Pickard & Emery (1990). Detailed observations for meridional sections near 195°E (Wyrtki & Kilonsky 1984) and 165°E (Delcroix et al. 1987) are available. For detailed numerical simulations of the tropical Pacific Ocean seasonal cycle see e.g. Philander et al. (1987) and Gordon & Corry (1991).

9.1 Forcing data

The surface heat flux Q is prescribed as in section 8 (see equ. 8.1). The surface wind stress $\underline{\tau}$ is taken from the Hellerman dataset (Hellerman & Rosenstein 1983) of monthly mean values on a 2° × 2° grid, linearly interpolated in space and time. As this dataset is generally regarded as an overestimate of the true stress, values are reduced to 75% of the original stresses. Further, stresses are reduced to zero near the artificial northern and southern boundaries of the model. Thus the Hellerman values are multiplied by the factor

$$F(y) = 0.75 \begin{cases} 0 & y < -30 \\ (y+30)/10 & -30 < y < -20 \\ 1 & -20 < y < 20 \\ (30-y)/10 & 20 < y < 30 \\ 0 & 30°N < y \end{cases} \qquad (9.1)$$

where units for y are degrees of latitude. The resulting wind stress patterns for various times of year are shown in Fig. 9.1, with north-easterly and south-easterly trade winds being the main feature. The cycle of zonal stress along the equator is given in Fig. 9.2: the zonal stress component is easterly year round, apart from the seasonal monsoon reversal in the west Pacific, and the westerlies that appear next to the South American coast.

9.2 Model seasonal cycle

The ocean model was integrated for 13 years using the above forcing, by which time the ocean had effectively settled into a steady seasonal cycle. Values vary smoothly from one month to the next, with no short time scale wave activity such as the observed shear instabilities (Legeckis 1977), so instantaneous values are shown in the spatial maps provided for various times of year. The time-longitude diagrams below are constructed

by saving values at 96 times per year.

The currents in layers 1 and 2 are shown in Figs. 9.3 and 9.4 (x-y), and Fig. 9.5 (x-t along the equator). The surface current pattern $\underline{u}_1$ is dominated by the westward South Equatorial Current (SEC), which here is strongest in Sep-Jan, with speeds of up to 80 $cm\ sec^{-1}$, and weakest in Apr-May. The eastward North Equatorial Counter-Current (NECC) is also evident across most of the Pacific most of the year, strongest in October and fading in Mar-Apr. In the west Pacific the North Equatorial Current (NEC) can be seen at about $15°N$, dividing into northward and southward branches at the west coast. The strong southward branch is the Mindanao Current, which turns eastward to run into the NECC. The western boundary current is not well resolved by the zonal grid. (See Masumoto & Yamagata 1992 for a higher resolution model of this region.) On the eastern side, there is no obvious Peru Current along the east coast.

The main feature in the lower layer is the Equatorial Under-Current (EUC), which flows eastward along the equator. The magnitude (up to 50 $cm\ sec^{-1}$) is substantially less than that observed, but bear in mind that the currents in this model represent averages over the depth of the respective layers. The linearised mass transport in the model EUC at $195°E$ (the approximate location of the Hawaii-Tahiti Shuttle Experiment described by Wyrtki & Kilonsky 1984) varies from $45 \times 10^6\ m^3\ sec^{-1}$ (45 Sv) in July to 15Sv in December. Wyrtki & Kilonsky (1984) estimate an average of 30Sv for the observed EUC.

Upper layer depth h_1 is shown in Fig. 9.6 . This layer is shallowest in the east Pacific, generally deepening westward at all latitudes before changing sharply at the western edges of the sub-tropical gyres. Note that in this model entrainment from cooler layer 2 into layer 1 occurs where $h_1 < 40m$ in the equatorial east Pacific and along the east coast. There is little seasonal variation in this field, the most obvious being the changes north of the equator in the central Pacific that are associated with variations in the NECC.

Gradients in the depth $h_1 + h_2$ (Fig. 9.7) provide the pressure gradients in layer 2 that principally drive the currents there. Like h_1, $h_1 + h_2$ generally deepens westward. Along the equator the eastward pressure gradient is not balanced by Coriolis forces, thus giving rise to the strong EUC, whereas currents are weak away from the equator. Note that in this experiment $h_1 + h_2$ is not affected by entrainment, as it is never deep enough ($> 700m$) to cause entrainment from the deep passive layer below. Again, seasonal variation is weak. Note that $h_1 + h_2$ varies less when h_1 is allowed to change (as here) than when h_1 is fixed (as in the Cane & Zebiak model), because the wind stress is partially balanced by gradients in h_1.

The temperature difference $T_1 - T_c$ is given in Fig. 9.8 . The largest positive errors (i.e. model too warm) occur well outside the equatorial region, near the north-east and

south-east boundaries: these values are significantly larger than found in the static case (see Fig. 8.4), for reasons that are not clear. (Possibly changes in h_1 cause shifts in the phase of the seasonal cycle response to the surface flux.) This tendency for positive error also extends along the South American coast. However, differences are generally less than $1°C$ in the west Pacific and the subtropics, as found in the static case. For the dynamic model, advection from the cooler east Pacific has reduced the positive error in the west Pacific slightly compared to the static case.

In the dynamical model the errors in the important equatorial cold tongue region are generally less than about about $1.5°C$. Entrainment and advection combine to cool this region substantially compared to the static case. Fig. 9.8 also shows that the regions just north and south of the cold tongue tend to be too warm, suggesting that the cooling entrainment occurs in too narrow a region.

Another way of comparing T_1 and T_c is to use area averages. The 'NINO' areas shown in Fig. 9.9a are often used to monitor SST variations, and the model and observed seasonal cycles for NINO3 (east Pacific) and NINO4 (central Pacific) are provided in Fig. 9.9b . By this measure, T_1 and T_c agree well in NINO4, where variability is small, while T_1 tends to be $0.5 - 1°C$ too warm most of the year in NINO3.

The more detailed time-longitude equatorial cycle of T_1 and $T_1 - T_c$ is given in Fig. 9.10 . Compared to T_c, the model cold tongue is too cold in Feb-Mar-Apr and too warm in Sep-Oct. The observed cold tongue is coolest in September and warmest in March (Fig. 8.3), so the model seasonal cycle is too weak. Fig. 9.10 also reveals a warm error in May-June around $220°E$, with a strong temperature gradient to the east. This warm anomaly is terminated by a sharp cooling.

The temperature equation (7.1) can be re-written as

$$\rho_o c_p h_1 \frac{\partial T_1}{\partial t} = Q + Q_e + Q_{xadv} + Q_{yadv} + dissipation \quad , \tag{9.1}$$

where Q is the surface heat flux (eq. 8.1), and

$$Q_e = -\rho_o c_p (T_1 - T_2) w_{e1} \quad , \tag{9.2}$$

$$Q_{xadv} = -\rho_o c_p \bar{h}_1 u_1 \partial T_1 / \partial x \quad , \tag{9.3}$$

$$Q_{yadv} = -\rho_o c_p \bar{h}_1 v_1 \partial T_1 / \partial y \quad . \tag{9.4}$$

The surface flux Q and the entrainment flux Q_e into layer 1 along the equator are given in Fig. 9.11 . The surface flux is generally small in the west Pacific ($< 50\ W\ m^{-2}$), and is largest in February-March in the east when the cold tongue is too cold. Cooling by

entrainment only occurs east of $240°E$, and the strong cooling in March causes the cool error in $T_1 - T_c$ at that time. The May-June warm error in $T_1 - T_c$ noted above is large enough to cause the surface flux then to become slightly negative in compensation.

The zonal heat advection Q_{xadv} is provided in Fig. 9.12a: note that negative values imply a cooling tendency. In the central and west Pacific this term is generally weak, though values lower than $-100\ W\ m^{-2}$ appear early in the year. The main feature is the strong negative region that appears near $240°E$ in May and moves westward over the next few months: this is associated with the strong zonal temperature gradient evident in Fig. 9.10a. Q_{yadv} (not shown) also has a smaller cooling tendency here. The cooling influence of Q_{xadv} weakens near $240°E$ in April as u_1 weakens (Fig. 9.5a), and this seems to be the cause of the warm patch that appears there.

Upper layer divergence along the equator is given in Fig. 9.12b: with little temporal change in h_1, this term is approximately equal to $w_{1e}/\bar{h}_1$ in the entrainment region and effectively zero elsewhere. The diagram shows that w_{1e} is not maximum at the time of strongest Q_e.

Another useful way of viewing the model structure is to plot cross-sections at select latitudes and longitudes. The general equatorial structure of the model can be seen in the cross-sections in Fig. 9.13 for April 1. The upper layer depth varies from $200m$ in the west to less than $40m$ in the east, while $h_1 + h_2$ varies much less, so the lower layer thickness increases markedly from west to east. Zonal currents are mostly of opposite sign in the two layers. The temperature section shows a cold-tongue minimum at the equator, and also shows the zonal profile fixed for T_2.

The meridional cross-sections in Fig. 9.14 are at $195°E$; approximately the location of the Hawaii-Tahiti Shuttle Experiment (Wyrtki & Kilonsky 1984). h_1 and $h_1 + h_2$ have generally the same shape, being deepest in the centre of the subtropical gyres. Across the equator h_1 bows upward while $h_1 + h_2$ bows down, which is the signature of the SEC and EUC. Further north h_1 shallows again, in conjunction with the NECC.

10. Conclusions

The aim at the outset was to develop an ocean model that could simulate the seasonal cycle in the Pacific Ocean reasonably well while using simplified and easily understandable physical processes. This aim has been achieved.

With a view to coupling this model to an atmospheric model, the most important feature to simulate is the sea surface temperature, as it is the SST that communicates with the overlying atmosphere. In the important equatorial region the SST error (model minus climatology) is less than $1°C$ in the west Pacific, and generally less than $1.5°C$ in the east Pacific. The main weaknesses are the positive and negative errors in the equatorial cold tongue (where the amplitude of the seasonal cycle is too low), and a tendency to form strong temperature gradients in the east-central Pacific. These defects are partly due to the very simple forms for entrainment and lower layer temperature used in the model. They must also be partly due to errors in the forcing fields: in particular, the surface heat flux given by equ. (8.1) contains uncertain climatology and has an oversimplified form of feedback.

The TOGA Numerical Experimentation Group (TOGA–NEG) has been carrying out an intercomparison experiment using several ocean GCMs (including the UKMO Pacific model), and using climatological forcing fields as applied in the seasonal cycle experiment described in section 9. The results (Stockdale, private communication: see also Appendix D of the 1991 TOGA Scientific Steering Group Report [WMO/TD 441]) show equatorial SST errors that in most cases are comparable to those found for this reduced physics model. The GCM errors are in some cases due to low resolution. However it does seem that, for SST at least, the reduced physics and GCM models have similar simulation skill. It remains to be seen whether that conclusion is also true for interannual changes. The interannual behaviour of the reduced physics model is being assessed, and will be the subject of another article.

How might this model be improved? With regard to the surface heat flux, Seager (1988, 1989) has developed an improved formulation that gave good SST results when used with the Cane & Zebiak ocean model, and that approach could be adopted. Entrainment temperatures depended on the lower layer structure in that model, whereas temperature in layer 2 was fixed for the the model results described here, so improvements in the SST simulation could probably be made by altering the temperature entrainment algorithm.

References

Allen MR, Davey MK (1991) Empirical parameterisation of tropical ocean-atmosphere coupling: the 'inverse Gill' problem. To appear in J Clim

Anderson DLT, McCreary JP (1985) Slowly propagating disturbances in a coupled ocean-atmosphere model. J Atmos Sci 42:615-628

Battisti DS (1988) The dynamics and thermodynamics of a warming event in a coupled tropical atmosphere-ocean model. J Atmos Sci 45:2889-2919

Battisti DS, Hirst AC (1989) Interannual variability in the tropical atmosphere-ocean system: Influence of the basic state, ocean geometry and nonlinearity. J Atmos Sci 46:1687-1712

Budin G, Davey MK (1990) Intermediate models of intraseasonal and interannual waves in the tropics. J Mar Sys 1:39-50

Busalacchi AJ, O'Brien JJ (1981) Interannual variability of the equatorial Pacific in the 1960's. J Geophys Res 86:10901-10907

Busalacchi AJ, Takeuchi K, O'Brien JJ (1983) Interannual variability of the equatorial Pacific - revisited. J Geophys Res 88:7551-7562

Cane MA, Zebiak SE, Dolan SC (1986) Experimental forecasts of El Niño. Nature 321:827-832

Cox MD (1984) A primitive equation, 3-dimensional model of the ocean. GFDL Ocean Group Tech Rep. 1, Geophys. Fluid Dyn. Lab./NOAA, Princeton, N.J.

Delcroix T, Eldin G, Hénin C (1987) Upper ocean water masses and transports in the western tropical Pacific (165°E). J Phys Oceanog 17:2248-2262

Delcroix T, Picaut J, Eldin G (1991) Equatorial Kelvin and Rossby waves evidenced in the Pacific Ocean through Geosat sea level and surface current anomalies. J Geophys Res 96:3249-3262

Epstein ES (1991) On obtaining daily climatological values from monthly means. J Clim 4:365-368

Gill AE (1980) Some simple solutions for heat-induced tropical circulations. Q J Roy Met Soc 106:447-462

Gill AE (1982) Atmosphere-Ocean Dynamics. Academic Press.

Goldenberg SB, O'Brien JJ (1981) Time and space variability of tropical Pacific wind stress. Mon Weath Rev 109:1190-1207

Gordon C (1989) Tropical ocean-atmosphere interactions in a coupled model. Phil Trans Roy Soc London A329:207-223

Gordon C, Corry RA (1991) A model simulation of the seasonal cycle in the tropical Pacific ocean using climatological and modeled surface forcing. J Geophys Res 96:847-864

Hellerman S, Rosenstein M (1983) Normal monthly windstress over the world ocean with error estimates. J Phys Oceanog 13:1093-1104

Hirst AC (1989) Unstable and damped equatorial modes in simple coupled ocean-atmosphere models. J Atmos Sci 43:606-630

Inoue M, O'Brien JJ (1987) Interannual variability in the tropical Pacific for the period 1979-1982. J Geophys Res 92:11671-11679

Keen RA (1982) The role of cross-equatorial tropical cyclone pairs in the Southern Oscillation Mon Weath Rev 110:1405-1416

Kraus EB, Turner JS (1967) A one dimensional model of the seasonal thermocline. Part II Tellus 19:98-105

Legeckis R (1977) Long waves in the eastern equatorial Pacific: a view from a geostationary satellite Science 197:1177-1181

Levitus S (1982) Climatological atlas of the world ocean. NOAA Prof. Pap. 13, Natl. Oceanic and Atmos. Admin., Boulder, Colo.

Masumoto Y, Yamagata T (1991) The response of the western tropical Pacific to the Asian winter monsoon: the generation of the Mindanao Dome. J Phys Oceanog 21:1386-1398

McCreary JP, Anderson DLT (1991) An overview of coupled ocean-atmosphere models of El Niño and the Southern Oscillation. J Geophys Res 96:3125-3150

McCreary JP, Kundu PK (1988) A numerical investigation of the Somali Current during the Southwest Monsoon. J Mar Res 46:25-58

McPhaden MJ, Freitag HP, Hayes SP, Taft BA (1988) The response of the equatorial Pacific Ocean to a westerly wind burst in May 1986 J Geophys Res 93:10589-10603

Murakami T, Sumathilapa WL (1989) Westerly bursts during the 1982/83 ENSO J Clim 2:71-85

Neelin JD, Latif M, Allaart MAF, Cane MA, Cubasch U, Gates WL, Gent PR, Ghil M, Gordon C, Lau NC, Mechoso CR, Meehl GA, Oberhuber JM, Philander SGH, Schopf PS, Sperber KR, Sterl A, Tokioka T, Tribbia J, Zebiak SE (1991) Tropical air-sea interaction in general circulation models. Climate Dyn , to appear

Oberhuber JM (1988) An atlas based on the COADS dataset. Max-Planck-Institut für Meteorologie Report No. 15

Pacanowski R, Philander SGH (1981) Parametrization of vertical mixing in numerical models of the tropical oceans. J Phys Oceanog 11:1443-1451

Philander SGH (1990) El Niño, La Niña and the Southern Oscillation. Academic Press, 287pp.

Philander SGH, Hurlin WJ, Seigel AD (1987) Simulation of the seasonal cycle of the tropical Pacific Ocean. J Phys Oceanog 17:1986-2002

Pickard GL, Emery WJ (1990) Descriptive physical oceanography. (5th edition) Pergamon Press, 320pp.

Sausen R, Barthel K, Hasselmann K (1988) Coupled ocean-atmosphere models with flux correction. Climate Dyn 2:154-163

Schopf PS, Suarez MJ (1988) Vacillations in a coupled ocean-atmosphere model. J Atmos Sci 45:549-566

Seager R, Zebiak SE, Cane MA (1988) A model for the tropical Pacific sea surface temperature climatology. J Geophys Res 93:1265-1280

Seager R (1988) A model of the tropical Pacific sea surface temperature climatology. J Geophys Res 93:1265-1280

Seager R (1989) Modeling tropical Pacific sea surface temperature: 1970-1987. J Phys Oceanog 19:419-434

Slingo A (1985) Handbook of the Meteorological Office 11-layer atmospheric general circulation model. UKMO Tech Note DCTN 29

Slingo A, Wilderspin RC, Smith R.N.B. (1989) The effect of improved physical parameterizations on simulations of cloudiness and the Earth's radiation budget. J Geophys Res 94:2281-2302

Smith RNB (1990) A scheme for predicting layer clouds and their water content in a general circulation model. Q J Roy Met Soc 116:435-460

Woodruff SD, Slutz RJ, Jenne RL, Steurer PM (1987) A Comprehensive Ocean Atmosphere Data Set. Bull Amer Met Soc 68:1239-1250

Wyrtki K, Kilonsky B (1984) Mean water and current structure during the Hawaii-to-Tahiti Shuttle Experiment J Phys Oceanog 14:242-254

Zebiak SE, Cane MA (1987) A model ENSO. Mon Weath Rev 115:2262-2278

Appendix A Vertical modes and wave speeds

Typical wave speeds and vertical modes can be determined by considering the free momentum and continuity equations

$$\frac{\partial \underline{u}_1}{\partial t} + f\underline{k} \times \underline{u}_1 = -\frac{1}{\rho_0}\nabla p_1 \quad , \tag{A1}$$

$$\frac{\partial \underline{u}_2}{\partial t} + f\underline{k} \times \underline{u}_2 = -\frac{1}{\rho_0}\nabla p_2 \quad , \tag{A2}$$

$$\frac{\partial h_1}{\partial t} + \bar{h}_1 \nabla . \underline{u}_1 = 0 \quad , \tag{A3}$$

$$\frac{\partial h_2}{\partial t} + \bar{h}_2 \nabla . \underline{u}_2 = 0 \quad . \tag{A4}$$

The two layers are coupled through the pressure gradient terms, given by (2.3) and (2.4) as before. These equations can be rewritten in terms of two independent vertical modes, denoted + and −. The fastest waves for each mode are the Kelvin waves; the speeds of other equatorial waves scale accordingly. The Kelvin wave speeds c_+ and c_- are given by

$$c_+{}^2 = \alpha g \gamma \sigma \quad , \tag{A5}$$

$$c_-{}^2 = \alpha g \Delta_1 \Delta_2 \bar{h}_1 \bar{h}_2 / \gamma \sigma \quad , \tag{A6}$$

where

$$\Delta_1 = \bar{T}_1 - \bar{T}_2 \quad , \tag{A7}$$

$$\Delta_2 = \bar{T}_2 - \bar{T}_3 \quad , \tag{A8}$$

$$\gamma = \Delta_2(\bar{h}_1 + \bar{h}_2) + \Delta_1 \bar{h}_1 \quad , \tag{A9}$$

$$\sigma = [1 + \sqrt{1 - 4\Delta_1 \Delta_2 \bar{h}_1 \bar{h}_2)/\gamma^2}\,]/2 \quad . \tag{A10}$$

For each mode the depth perturbations and velocities in (layer 1,layer 2) are proportional to $(\mu, 1)$, where

$$\mu_- = -1 + \Delta_1 \bar{h}_1 / \gamma \sigma \quad , \tag{A11}$$

$$\mu_+ \mu_- = -\bar{h}_1 / \bar{h}_2 \quad . \tag{A12}$$

Approximate values are

$$c_+ \approx \alpha g \Delta_2 (\bar{h}_1 + \bar{h}_2) \quad , \tag{A13}$$

$$c_- \approx \alpha g \Delta_1 \bar{h}_1 \bar{h}_2 / (\bar{h}_1 + \bar{h}_2) \quad , \tag{A14}$$

$$\mu_+ \approx \bar{h}_1 / \bar{h}_2 \quad , \tag{A15}$$

$$\mu_- \approx -1 \quad . \tag{A16}$$

(The above approximation is exact when $\Delta_1 = 0$.) Thus the + mode corresponds to the two layers acting in unison (the first baroclinic mode), whereas perturbations in each layer are opposed for the − mode (the second baroclinic mode).

Damping and dissipation terms are generally weak, and have little effect on the above properties. However, mass exchange by upwelling can have a strong damping effect on the waves. In particular, upwelling in the equatorial east Pacific cold tongue can severely inhibit the penetration of remotely-generated Kelvin waves into that region from the central and west Pacific.

Appendix B Variable grid algorithms

There are many ways of choosing variable grids. In most cases some functional form is used for the transition from coarse to fine resolution, and for the algorithms described below a cosine form is selected. Grids with the temperature points (T-points) centred between the velocity points (u-points and v-points) are considered. The procedure is to define the velocity points first: the meridional velocity v-points define the latitudinal grid (latitudes $YLATV_j$), and the zonal velocity u-points define the longitudinal grid (longitudes $XLONGU_i$). Meridional grids with the transition zones located symmetrically either side of the equator are described.

B.1 Meridional grid without a v-point on the equator

For the experiments described in this technical note the C-grid was chosen such that there is a line of u-points along the equator, so v-points were all located off the equator.

We consider a total of L v-points located at latitudes $YLATV_j$, with $L_1 = K_1 + N + M$ points south of the equator and $L_2 = M + N + K_2$ points north of the equator as shown schematically in Fig. B1a. The northernmost ocean boundary is at $YLATV_L$ and the southernmost boundary at $YLATV_1$. The extents of the constant and variable resolution regions are controlled by choosing K_1, K_2, N and M.

The $L-1$ separations $\Delta_j = YLATV_{j+1} - YLATV_j$ are given by

$$\frac{\Delta_j}{\Delta} = \begin{cases} 1 & j = 1,...,K_1 \\ \left(1+\epsilon+(1-\epsilon)\cos[\pi(j-K_1)/N]\right)/2 & j = K_1,...,K_1+N \\ \epsilon & j = K_1+N,...,K_1+N+2M \\ \left(1+\epsilon-(1-\epsilon)\cos[\pi(j-L_1-M)/N]\right)/2 & j = L_1+M,...,L_1+N+M \\ 1 & j = L_1+N+M,...,L-1 \end{cases} \qquad (B1)$$

where Δ is the coarse resolution near the north and south boundaries and $\epsilon\Delta$ is the finer resolution near the equator.

Using

$$\sum_{j=0}^{J} \cos(\pi j/J) = 0 \qquad (B2)$$

the sum of the separations is

$$YLATV_L - YLATV_1 = \Delta[K_1 + K_2 + N - 1 + \epsilon(2M+N)] \ . \qquad (B3)$$

The easiest way to determine a suitable grid is to solve the above equation for ϵ, varying the other parameters until a suitable value is obtained. For example, the C-grid for the two-layer model in Fig. 3.1b, which is based on half the resolution of the Met.O. tropical Pacific Ocean GCM grid (Fig. 3.1a), was calculated using K_1=K_2=M=2, N=19 (so L=46), $\Delta = 2°$, $YLATV_L = 28.75°N$, $YLATV_1 = -28.75°$, which gives $\epsilon = 0.59°$. The latitudes of the v-points can easily be determined once the separations are known. (NB In the numerical model an extra row of land v-points is added north of $YLATV_L$, so the total meridional number of v-points is $JDIM = L + 1$.)

B.2 Meridional grid with a v-point on the equator

A meridional grid with a v-point on the equator may also be used, as in for example the tropical Pacific Ocean GCM B-grid. Suppose there are $L_1 = K_1 + N + M - 1$ v-points south of the equator, and $L_2 = K_2 + N + M - 1$ north of the equator, giving $L = L_1 + L_2 + 1$ v-points as shown in Fig. B1b. The $L - 1$ separations are

$$\frac{\Delta_j}{\Delta} = \begin{cases} 1 & j = 1,...,K_1 \\ \left(1 + \epsilon + (1-\epsilon)\cos[\pi(j-K_1)/N]\right)/2 & j = K_1,...,K_1+N \\ \epsilon & j = K_1+N,...,K_1+N+2M-1 \\ \left(1 + \epsilon - (1-\epsilon)\cos[\pi(j-L_1-M)/N]\right)/2 & j = L_1+M,...,L_1+N+M \\ 1 & j = L_1+N+M,...,L-1 \end{cases} . \qquad (B4)$$

The sum of the separations is

$$YLATV_L - YLATV_1 = \Delta[K_1 + K_2 + N - 1 + \epsilon(2M + N - 1)] \quad . \qquad (B5)$$

B.3 Longitudinal grid of u-points

Suppose there are $L = M + N + K + 1$ u-points at longitudes $XLONGU_i$ distributed between and on the boundaries, as shown in Fig. B1c, with the westernmost ocean boundary at longitude $XLONGU_1$ and the easternmost at $XLONGU_L$. There is a broad interior coarse resolution band with grid separation Δ, and finer resolution near the eastern and western boundaries. The grid separation at the western boundary is $\epsilon\Delta$, and is $\epsilon\lambda\Delta$ at the eastern boundary. The separations $\Delta_i = XLONGU_{i+1} - XLONGU_i$ are given by

$$\frac{\Delta_i}{\Delta} = \begin{cases} \left(1+\epsilon-(1-\epsilon)\cos[\pi(i-1)/M]\right)/2 & i = 1,...,M+1 \\ 1 & i = M+1,...,M+N \\ \left(1+\lambda\epsilon+(1-\lambda\epsilon)\cos[\pi(i-M-N)/K]\right)/2 & i = M+N,...,M+N+K \end{cases} . \quad (B6)$$

The sum of the separations is the distance between the east and west boundaries:

$$XLONGU_L - XLONGU_1 = \Delta\ [\ N-1+(M+K)/2+(\epsilon/2)\big(M+1+\lambda(K+1)\big)\ ] . \quad (B7)$$

It is easiest to solve this equation for ϵ after choosing the other parameters, adjusting them until a satisfactory value for ϵ is obtained. The tropical Pacific OGCM longitudinal grid used in Fig. 3.1a was calculated with M=51, N=44, K=37 (so L=133), $\lambda = 1, \Delta = 1.5°, XLONGU_L = 281.25°E$, and $XLONGU_1 = 126.96°E$, which gives $\epsilon\Delta = 0.54°$.

The grid for the two-layer model (Fig. 3.1b) was calculated using N=111, K=0, M=0, $\Delta = 1.5°$, $XLONGU_1 = 123.75°E$, $XLONGU_L = 290.25°E$, to give uniform zonal resolution $\Delta_i = \Delta$. (NB The numerical model has an extra row of land u-points added east of $XLONGU_L$, so the total number of zonal u-pounts is $IDIM$=L+1.)

Appendix C The energy equation

A two-layer system with no forcing or dissipation is considered here. The equations of motion are (A1)-(A4). The total kinetic energy in a layer is

$$KE = \frac{1}{2}\bar{h}\sum_i\sum_j \overline{u_{ij}^2} + \overline{v_{ij}^2}\; dA_{ij} \quad , \tag{C1}$$

where the double sum is over all area elements centred on interior (ocean) h-points, with area $dA_{ij} = DXU_{i-1}DYV_{j-1}$. Choosing

$$\overline{u_{ij}^2} = \frac{1}{2}(u_{i-1j}^2 + u_{ij}^2) \quad , \tag{C2}$$

$$\overline{v_{ij}^2} = \frac{1}{2}(v_{ij-1}^2 + v_{ij}^2) \quad , \tag{C3}$$

and using $u = 0$ on east and west coasts, $v = 0$ on north and south coasts, and the grid definitions in section 3, (C1) gives on rearrangement

$$KE = \frac{1}{2}\bar{h}\sum\sum u_{ij}^2\; DXH_iDYV_{j-1} \;+\; v_{ij}^2\; DXU_{i-1}DYH_j \quad . \tag{C4}$$

The time derivative (denoted by subscript t) is

$$KE_t = \bar{h}\sum\sum u_{ij}(u_t)_{ij}\; DXH_iDYV_{j-1} \;+\; v_{ij}(v_t)_{ij}\; DXU_{i-1}DYH_j \quad . \tag{C5}$$

The u_t and v_t terms are replaced using the momentum equations (A1) and (A2). The Coriolis terms cancel, using the finite-difference forms defined in section 3, leaving

$$\begin{aligned} KE_{1t} = -\alpha g\bar{h}_1\sum\sum & u_{1ij}\left[\Delta_1(h_{1x})_{ij} + \Delta_2(h_{1x} + h_{2x})_{ij}\right]DXH_iDYV_{j-1} \\ & + \; v_{1ij}\left[\Delta_1(h_{1y})_{ij} + \Delta_2(h_{1y} + h_{2y})_{ij}\right]DXU_{i-1}DYH_j \quad , \end{aligned} \tag{C6}$$

$$\begin{aligned} KE_{2t} = -\alpha g\bar{h}_2\sum\sum & u_{2ij}\Delta_2(h_{1x} + h_{2x})_{ij}\; DXH_iDYV_{j-1} \\ & + \; v_{2ij}\Delta_2(h_{1y} + h_{2y})_{ij}\; DXU_{i-1}DYH_j \quad . \end{aligned} \tag{C7}$$

The potential energy in the two-layer system is

$$PE = \frac{1}{2}\alpha g\sum\sum \Delta_1 h_{1ij}^2 \;+\; \Delta_2(h_1 + h_2)^2\; dA_{ij} \quad . \tag{C8}$$

Taking the time derivative, and using the continuity equations (A3) and (A4) leads to

$$\begin{aligned} PE_t = -\alpha g\sum\sum & \Delta_1 h_{1ij}\bar{h}_1(u_{1x} + v_{1y})_{ij} + \\ & \Delta_2(h_1 + h_2)_{ij}\left[\bar{h}_1(u_{1x} + v_{1y}) + \bar{h}_2(u_{2x} + v_{2y})\right]_{ij}\; DXU_{i-1}DYV_{j-1} \quad . \end{aligned} \tag{C9}$$

Using the spatial derivatives defined in section 3, and the boundary conditions on u and v, we find for example that

$$\begin{aligned}\sum\sum u_{ij}(h_x)_{ij}DXH_iDYV_{j-1} \;+\; h_{ij}(u_x)_{ij}DXU_{i-1}DYV_{j-1}\\ &= \sum\sum u_{ij}(h_{i+1j}-h_{ij})DYV_{j-1} \;+\; h_{ij}(u_{ij}-u_{i-1j})DYV_{j-1}\\ &= \sum_j\Big(\sum_i u_{ij}h_{i+1j}-h_{ij}u_{i-1j}\Big)DYV_{j-1}\\ &= 0 \qquad . \end{aligned} \tag{C10}$$

All terms cancel in this way, leaving

$$KE_{1t}+KE_{2t}+PE_t=0 \quad . \tag{C11}$$

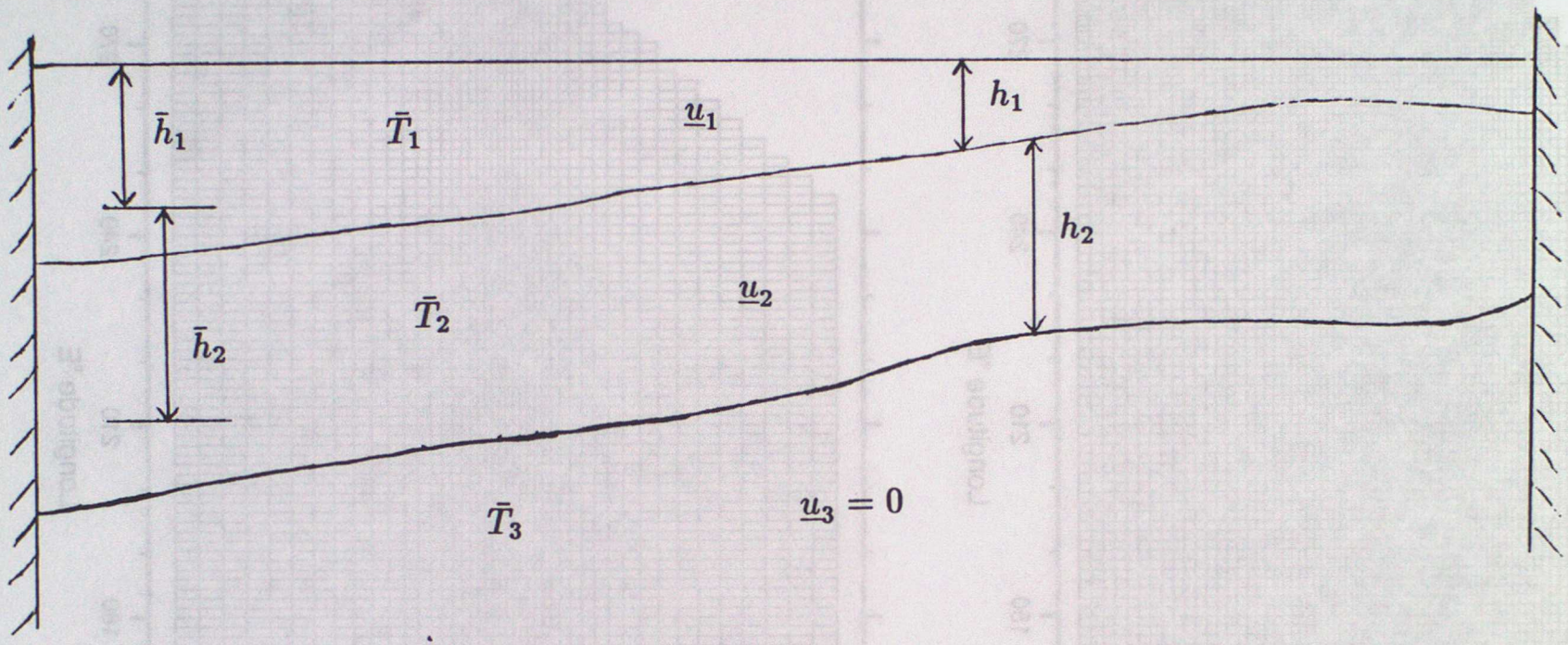

Fig. 2.1: The vertical structure of the dynamical ocean model, with two active layers overlying a deep passive layer. The equations of motion are linearised about a state of rest with layer depths $\bar{h}_1$ and $\bar{h}_2$ and density determined by fixed temperatures $\bar{T}_1$, $\bar{T}_2$ and $\bar{T}_3$.

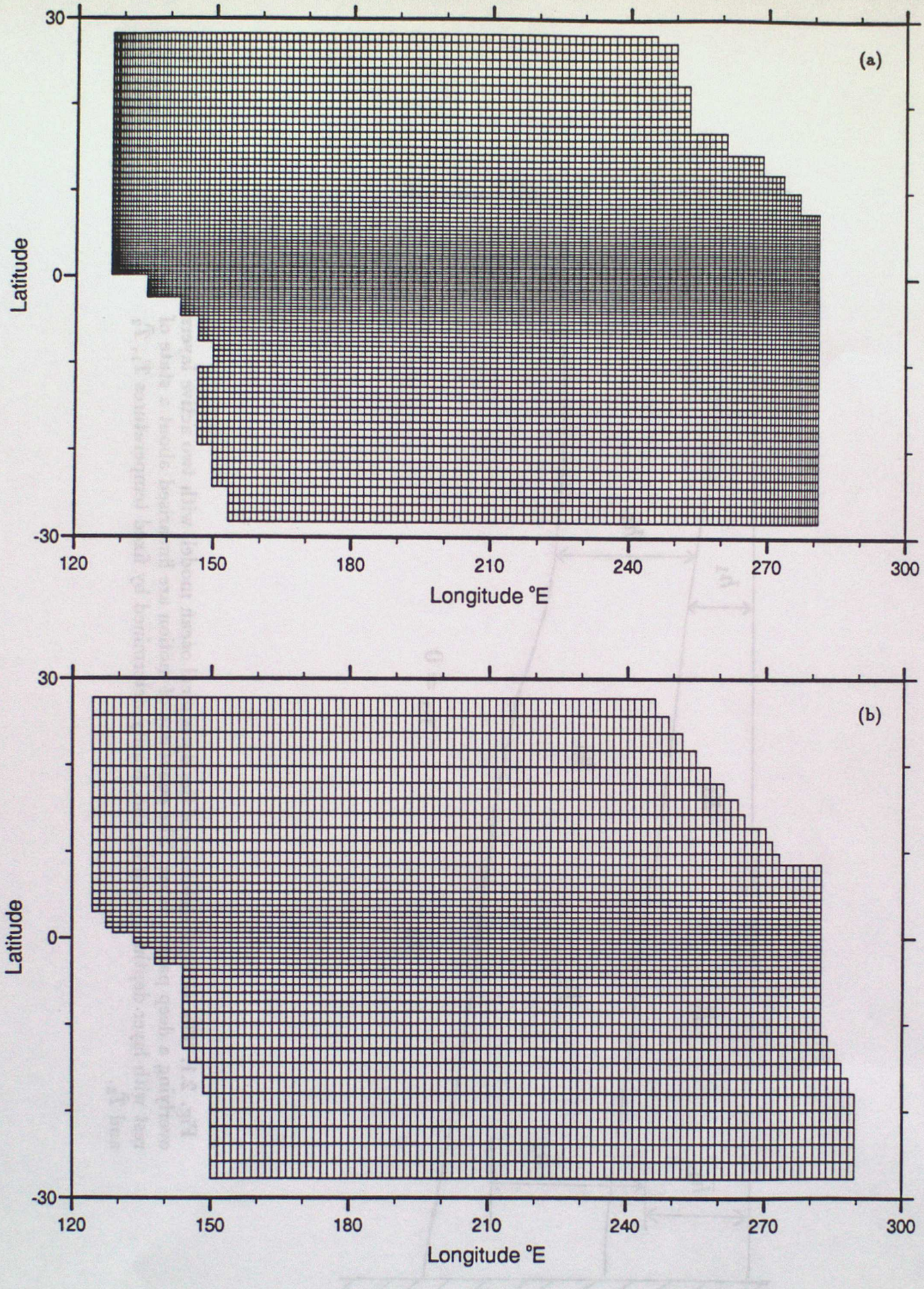

Fig. 3.1: Horizontal grids with variable resolution for the tropical Pacific Ocean.

(a) MetO general circulation model

(b) two-layer model, with land mask based on the FSU pseudostress dataset.

(a)

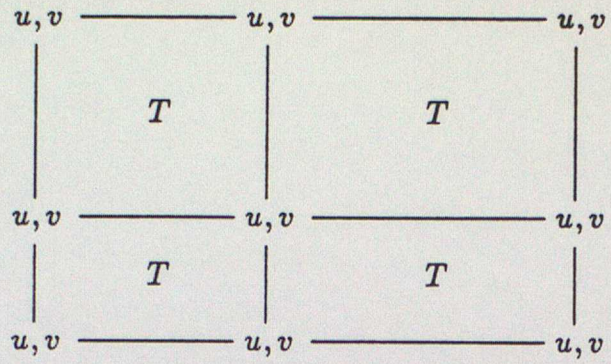

(b)

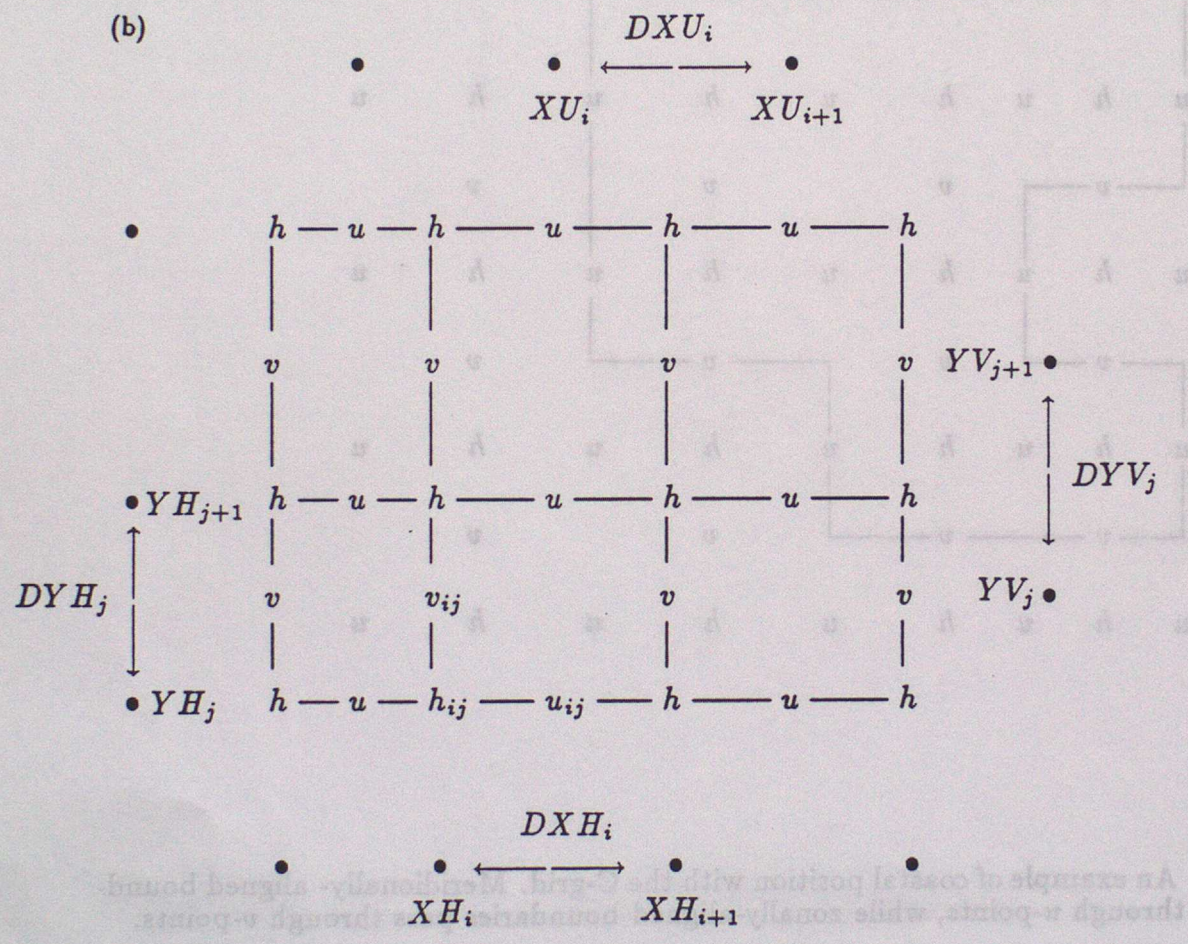

Fig. 3.2: Grid arrangements.

(a) the B-grid as used in the MetO ocean GCM

(b) the C-grid for the two-layer model, showing the naming convention used in the text and code.

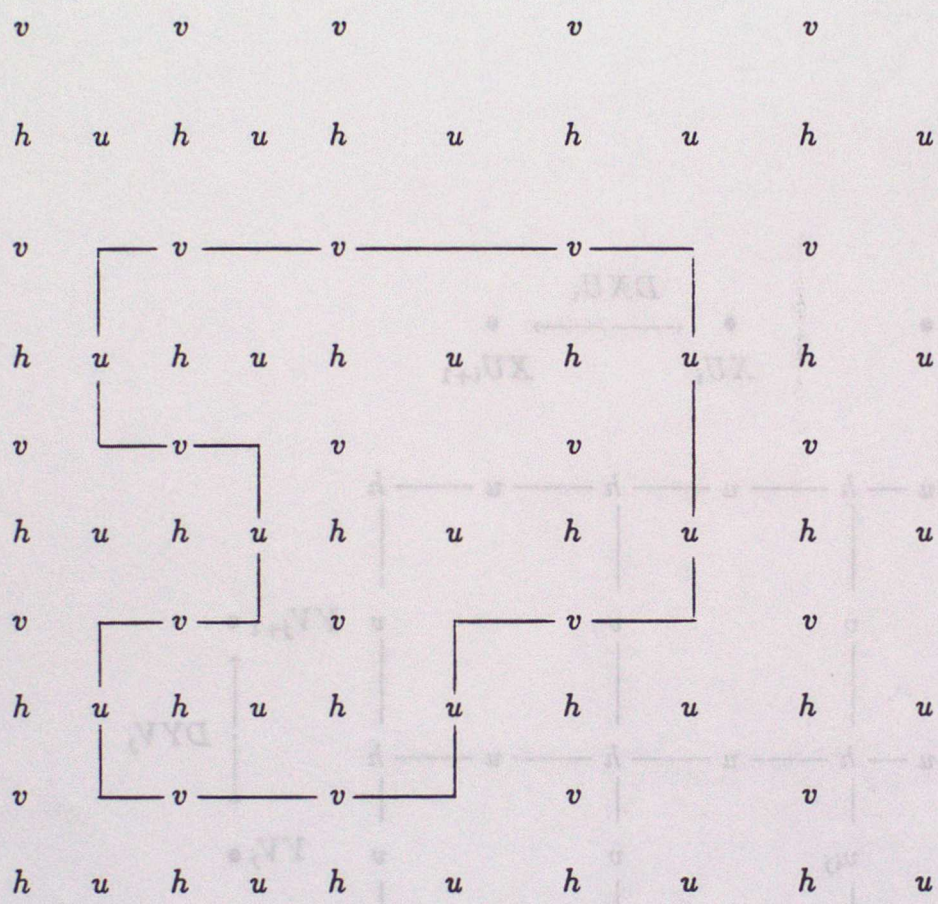

Fig. 3.3: An example of coastal position with the C-grid. Meridionally- aligned boundaries pass through u-points, while zonally-aligned boundaries pass through v-points.

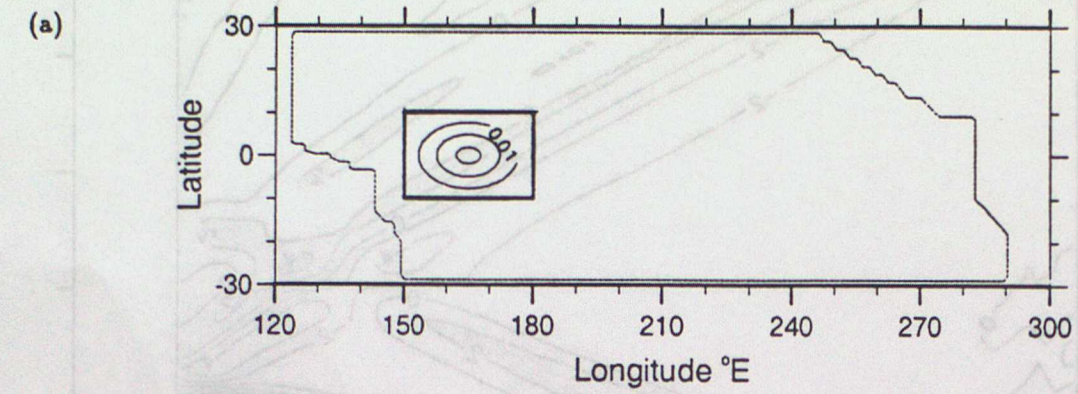

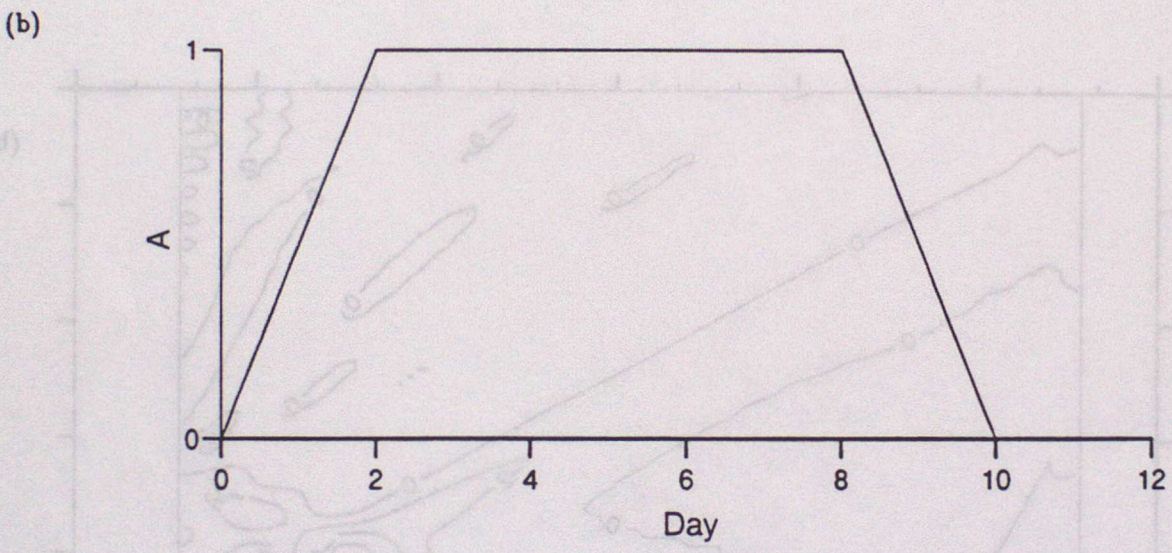

Fig. 5.1: Structure of the westerly windburst.

(a) The zonal wind stress at day 5.
Max = 0.032 $N\ m^{-2}$

(b) Time profile of amplitude A(t).

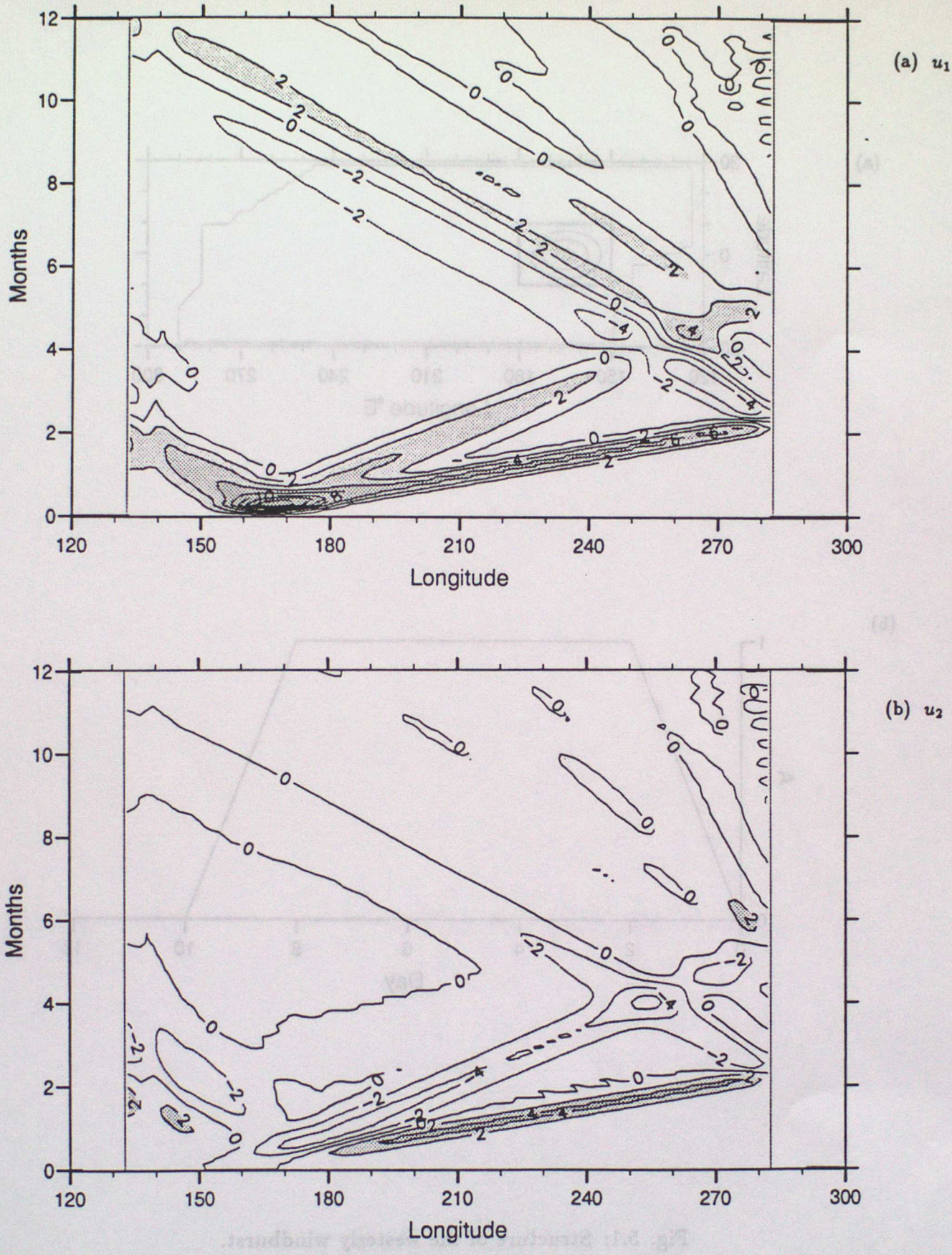

Fig. 5.2: Equatorial section of the zonal current reponse to a westerly windburst. Values greater than 2 $cm\ sec^{-1}$ are shaded.

(a) u_1, min=$-5.3\ cm\ sec^{-1}$, max=$16.0\ cm\ sec^{-1}$,

(b) u_2, min=$-6.7\ cm\ sec^{-1}$, max=$4.6\ cm\ sec^{-1}$.

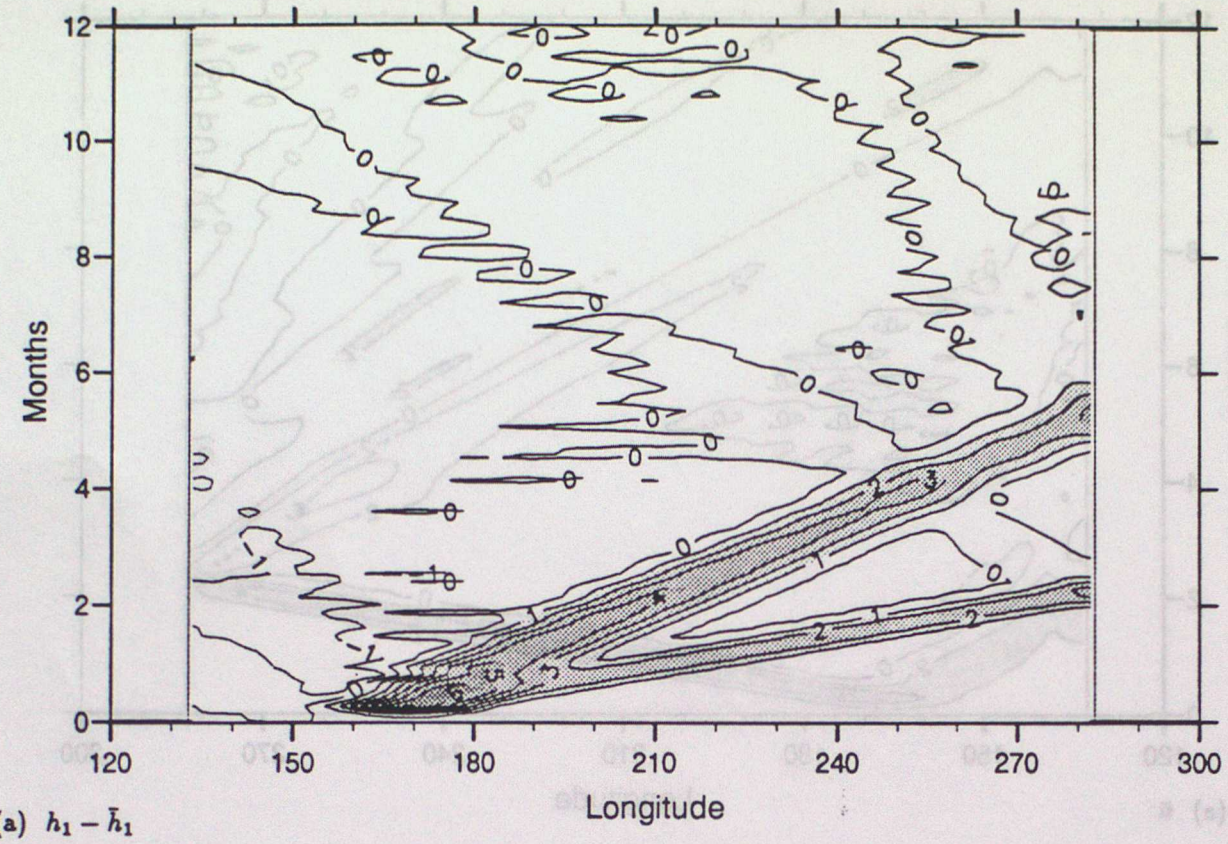

(a) $h_1 - \bar{h}_1$

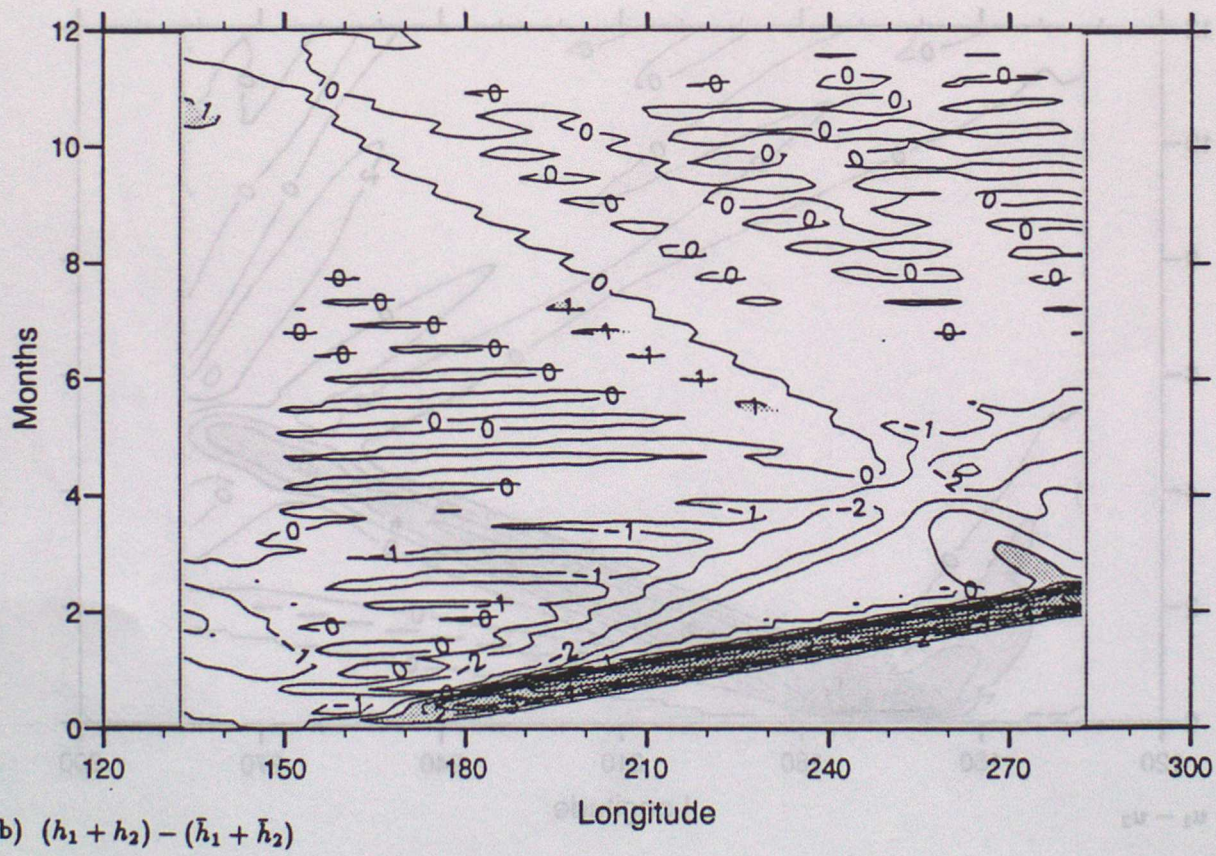

(b) $(h_1 + h_2) - (\bar{h}_1 + \bar{h}_2)$

Fig. 5.3: Equatorial section of the layer depth changes in reponse to a westerly wind-burst. Values greater than $1m$ are shaded.

(a) $h_1 - \bar{h}_1$, min=$-2.0m$, max=$7.1m$,

(b) $(h_1 + h_2) - (\bar{h}_1 + \bar{h}_2)$, min=$-3.1m$, max=$7.3m$.

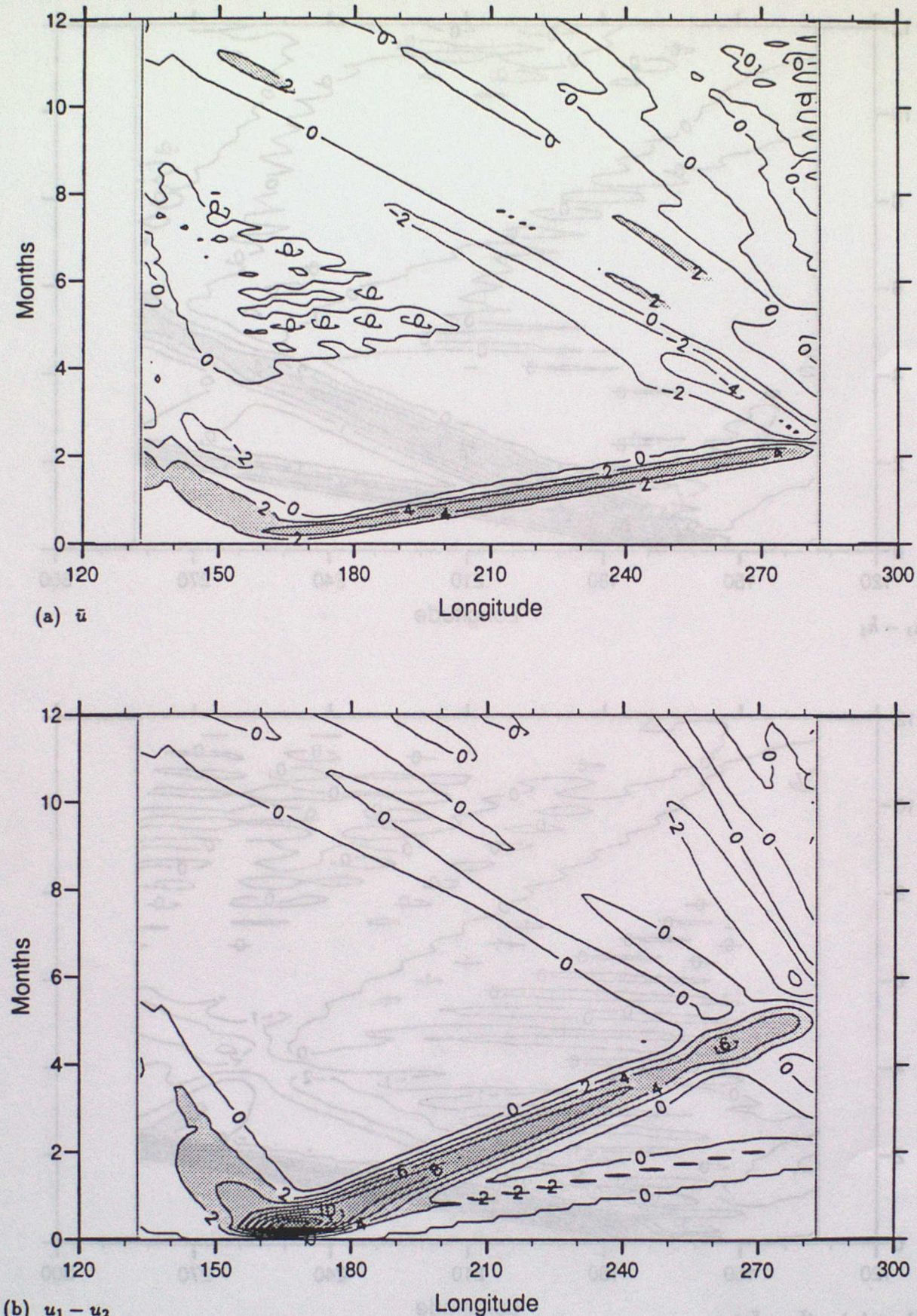

Fig. 5.4: Equatorial section of the zonal current reponse to a westerly windburst. Values greater than 2 *cm sec*$^{-1}$ are shaded.

(a) $\bar{u} = (\bar{h}_1 u_1 + \bar{h}_2 u_2)/(\bar{h}_1 + \bar{h}_2)$, min=$-4.8$ *cm sec*$^{-1}$, max=5.9 *cm sec*$^{-1}$,

(b) $u_1 - u_2$, min=-4.3 *cm sec*$^{-1}$, max=16.9 *cm sec*$^{-1}$.

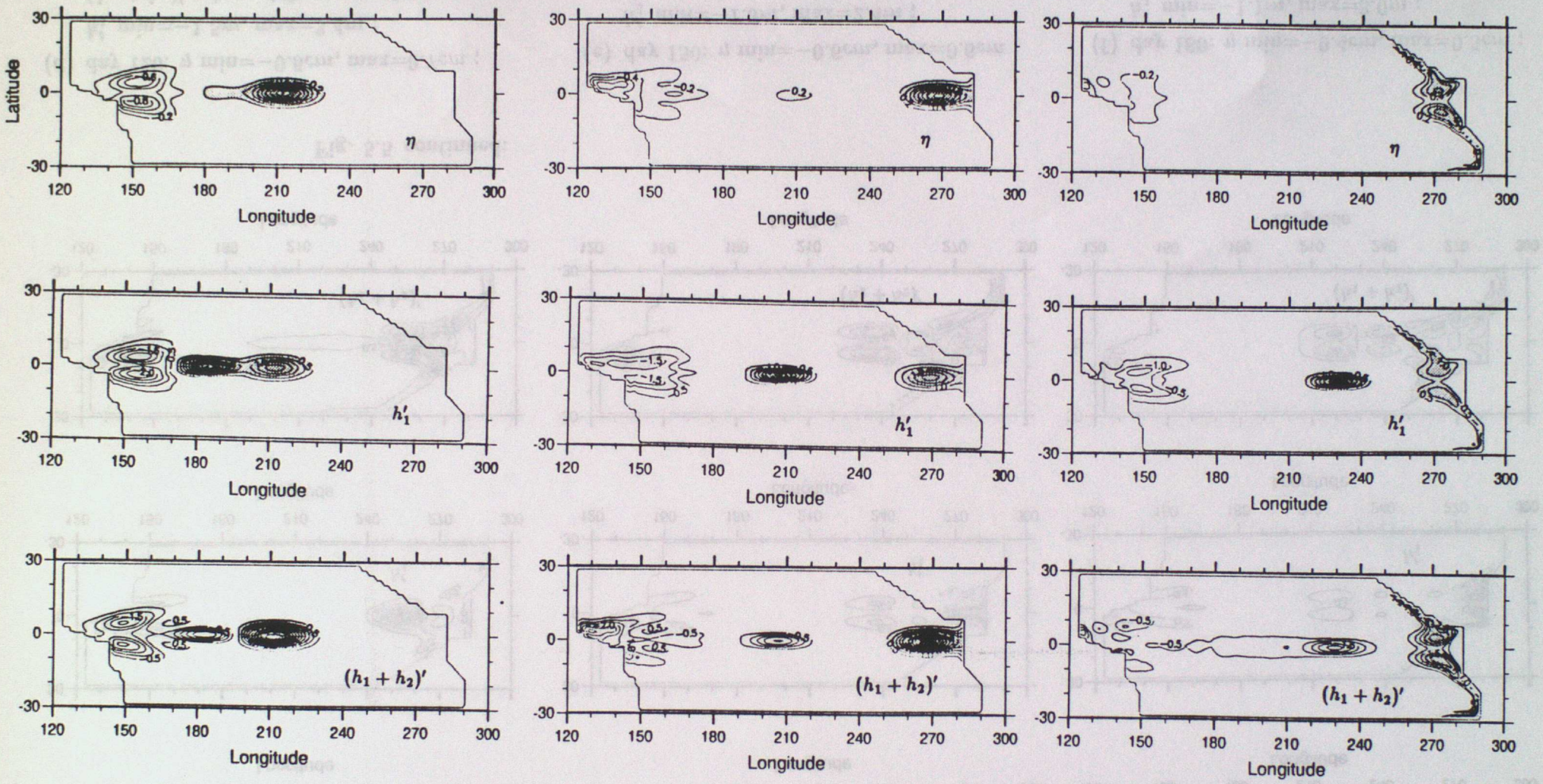

Fig. 5.5: Vertical displacements in response to a westerly windburst. Values of surface displacement η greater than 0.2 cm are shaded, values of $h_1' = h_1 - \bar{h}_1$ and of $(h_1 + h_2)' = h_1 + h_2 - (\bar{h}_1 + \bar{h}_2)$ greater than $0.5m$ are shaded.

(a) day 30: η min$=-1.0cm$, max$=1.7cm$;
h_1' min$=-2.9m$, max$=4.9m$;
$(h_1 + h_2)'$ min$=-3.0m$, max$=5.6m$

(b) day 60: η min$=-0.9cm$, max$=1.6cm$;
h_1' min$=-1.9m$, max$=4.2m$;
$(h_1 + h_2)'$ min$=-3.1m$, max$=5.6m$

(c) day 90: η min$=-0.6cm$, max$=2.0cm$;
h_1' min$=-1.7m$, max$=3.4m$;
$(h_1 + h_2)'$ min$=-2.7m$, max$=6.6m$

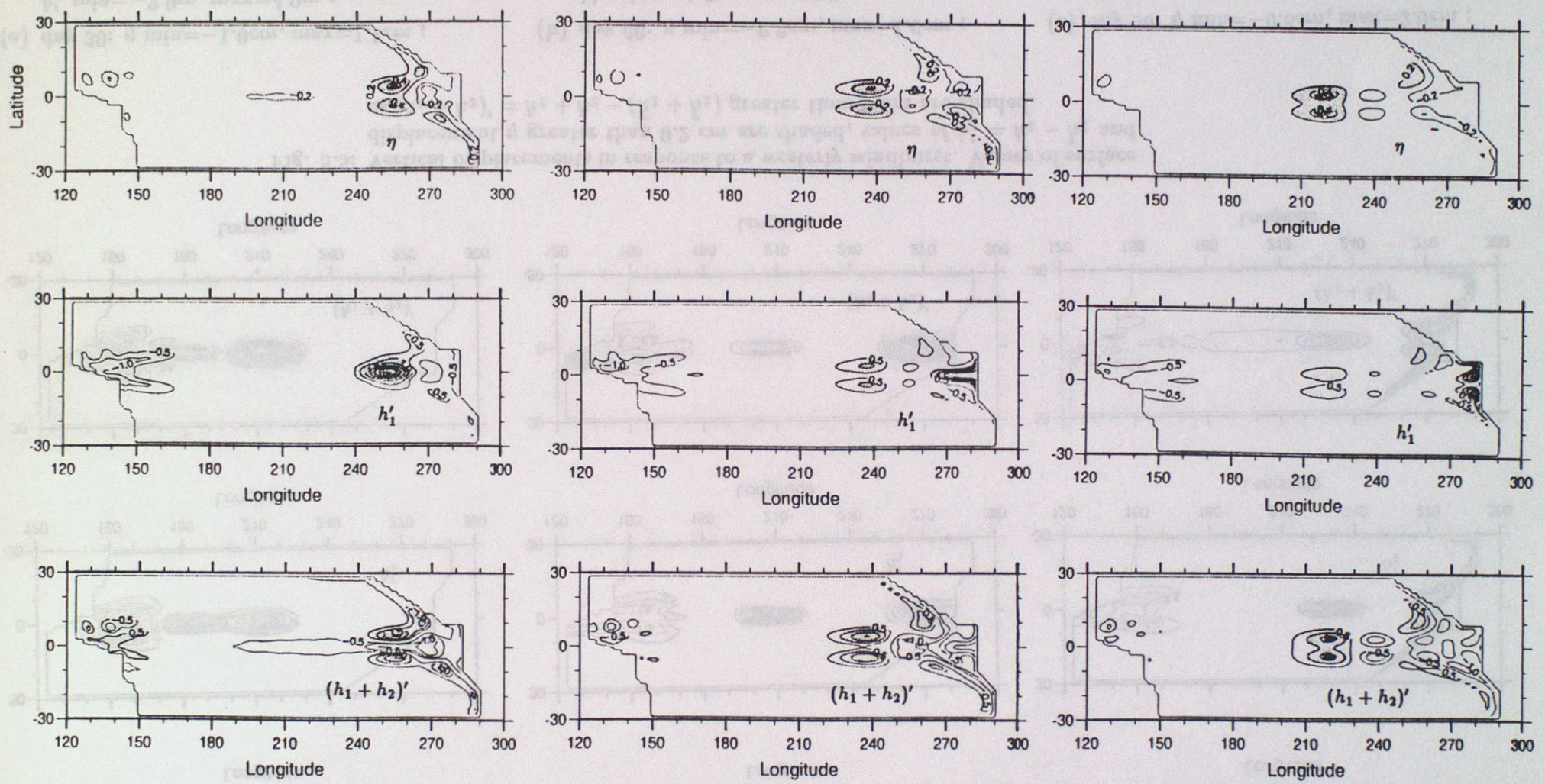

Fig. 5.5 continued:

(d) day 120: η min=$-0.5cm$, max=$0.7cm$;
h_1' min=$-1.5m$, max=$3.4m$;
$(h_1+h_2)'$ min=$-1.8m$, max=$2.1m$

(e) day 150: η min=$-0.6cm$, max=$0.6cm$;
h_1' min=$-1.3m$, max=$2.4m$;
$(h_1+h_2)'$ min=$-2.7m$, max=$2.0m$

(f) day 180: η min=$-0.4cm$, max=$0.5cm$;
h_1' min=$-1.1m$, max=$3.0m$;
$(h_1+h_2)'$ min=$-2.0m$, max=$1.7m$

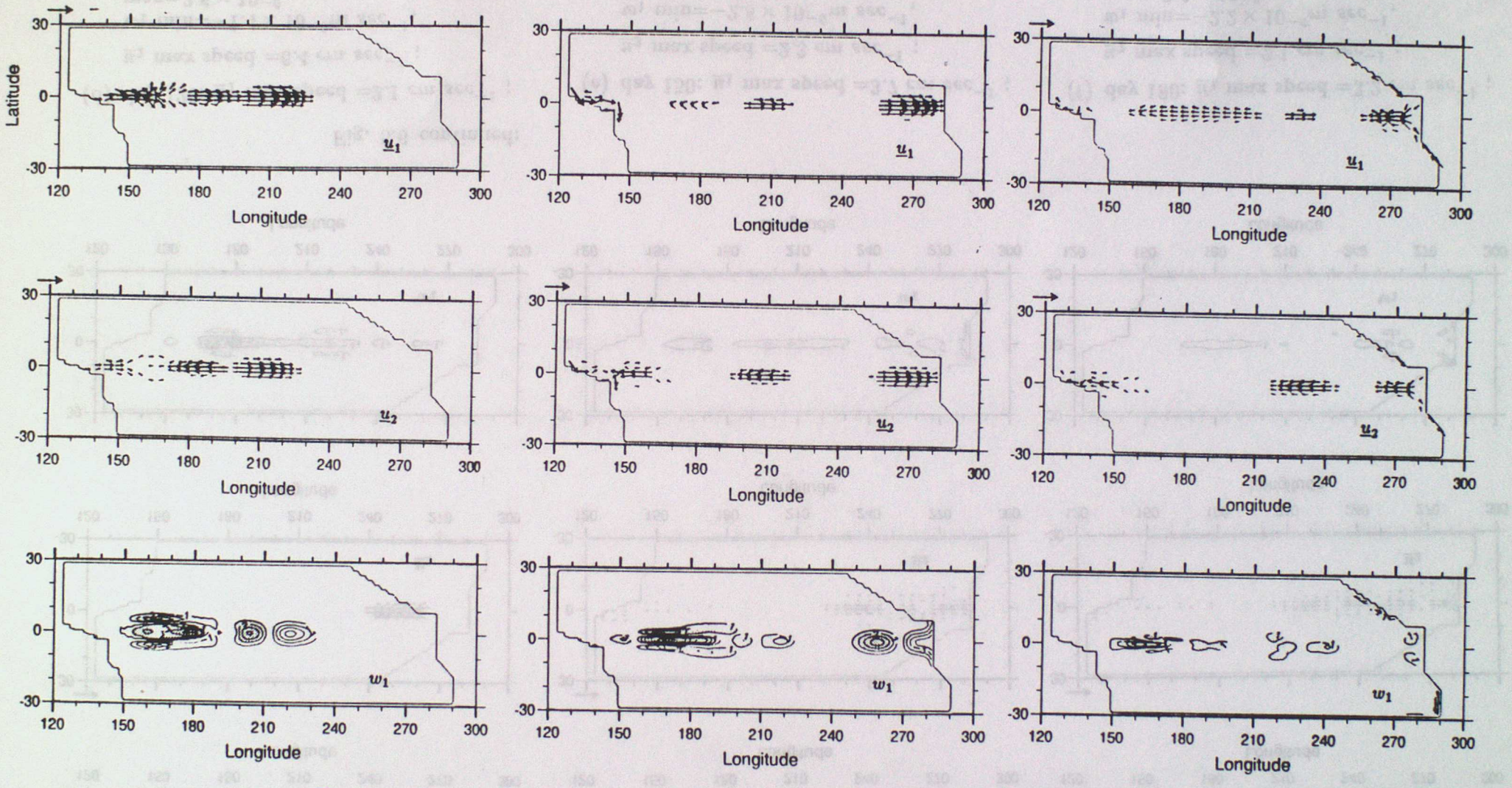

Fig. 5.6: Currents in response to a westerly windburst. Vectors (u, v) are drawn for speeds greater than 20% of the maximum in each case.
The scaling arrow represents 5 $cm\ sec^{-1}$.
Values of vertical velocity w_1 greater than $10^{-6} m\ sec^{-1}$ are shaded.

(a) day 30: $\underline{u}_1$ max speed $=6.5\ cm\ sec^{-1}$;
$\underline{u}_2$ max speed $=4.5\ cm\ sec^{-1}$;
w_1 min$=-4.4 \times 10^{-6} m\ sec^{-1}$,
max$=5.2 \times 10^{-6}$

(b) day 60: $\underline{u}_1$ max speed $=6.3\ cm\ sec^{-1}$;
$\underline{u}_2$ max speed $=4.3\ cm\ sec^{-1}$;
w_1 min$=-8.5 \times 10^{-6} m\ sec^{-1}$,
max$=4.5 \times 10^{-6}$

(c) day 90: $\underline{u}_1$ max speed $=4.7\ cm\ sec^{-1}$;
$\underline{u}_2$ max speed $=3.9\ cm\ sec^{-1}$;
w_1 min$=-4.7 \times 10^{-6} m\ sec^{-1}$,
max$=6.5 \times 10^{-6}$

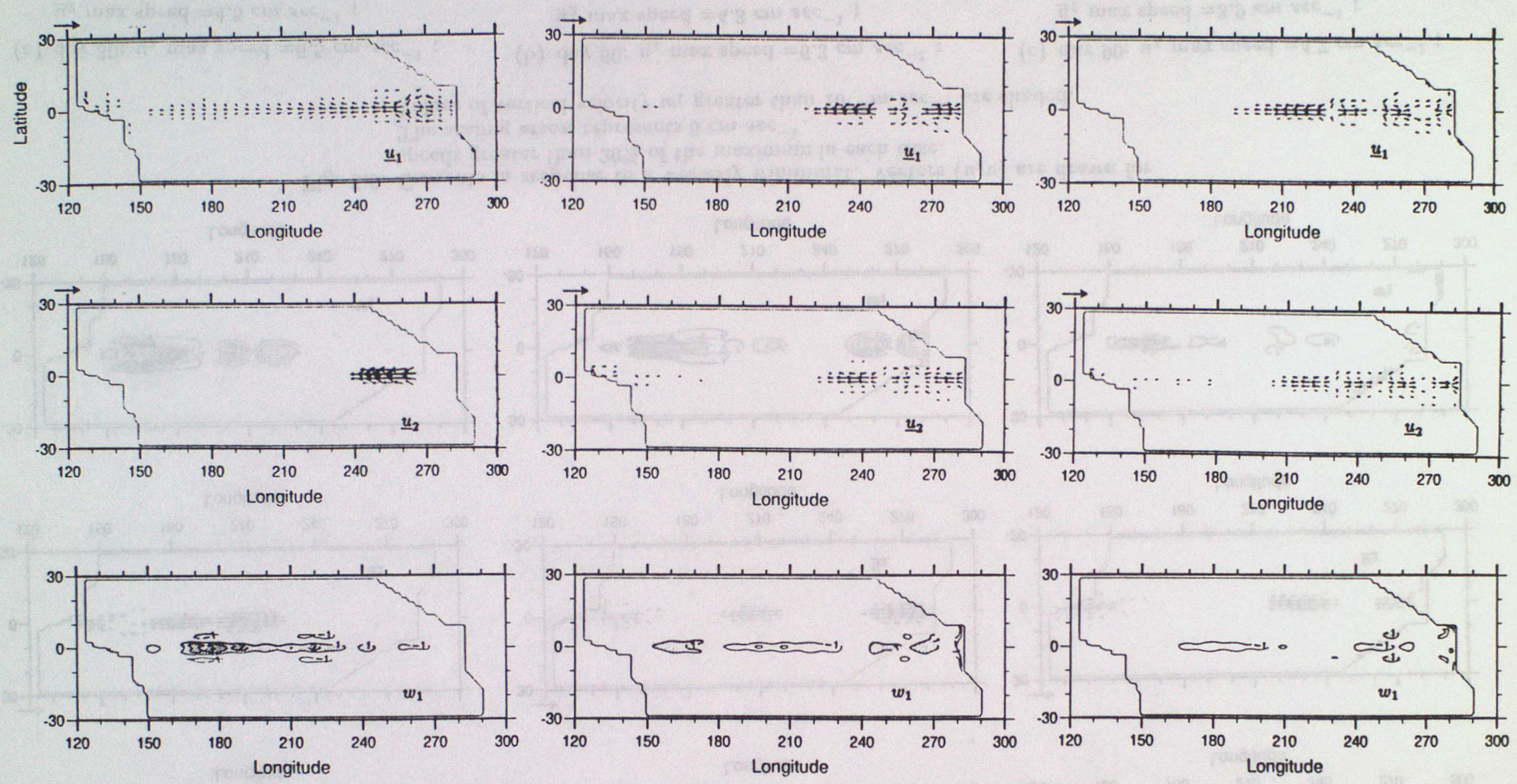

Fig. 5.6 continued:

(d) day 120: $\underline{u}_1$ max speed $=2.1\ cm\ sec^{-1}$;
$\underline{u}_2$ max speed $=6.4\ cm\ sec^{-1}$;
w_1 min$=-1.4\times10^{-6} m\ sec^{-1}$,
max$=2.6\times10^{-6}$

(e) day 150: $\underline{u}_1$ max speed $=3.7\ cm\ sec^{-1}$;
$\underline{u}_2$ max speed $=2.3\ cm\ sec^{-1}$;
w_1 min$=-2.8\times10^{-6} m\ sec^{-1}$,
max$=1.9\times10^{-6}$

(f) day 180: $\underline{u}_1$ max speed $=3.2\ cm\ sec^{-1}$;
$\underline{u}_2$ max speed $=2.1\ cm\ sec^{-1}$;
w_1 min$=-2.2\times10^{-6} m\ sec^{-1}$,
max$=3.6\times10^{-6}$

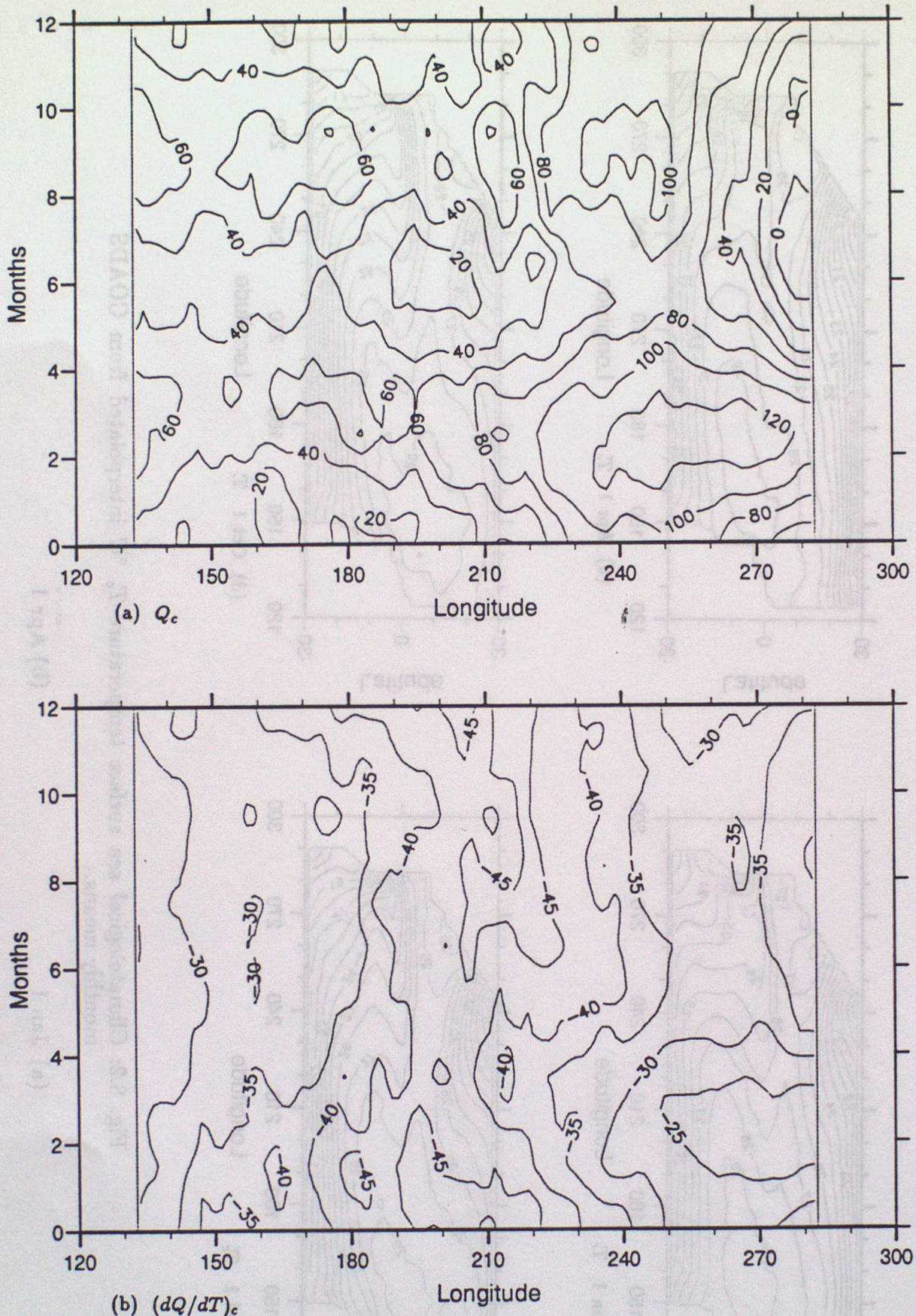

Fig. 8.1: The surface heat flux is formulated as $Q = Q_c - \left(dQ/dT\right)_c (T_c - T_1)$ with climatological values based on COADS monthly means (Oberhuber 1988).

(a) Q_c along the equator: max=137 $W\ m^{-2}$, min=−19.

(b) $\left(dQ/dT\right)_c$ along the equator: max=−20 $W\ m^{-2}\ {}^{\circ}C^{-1}$, min=−50.

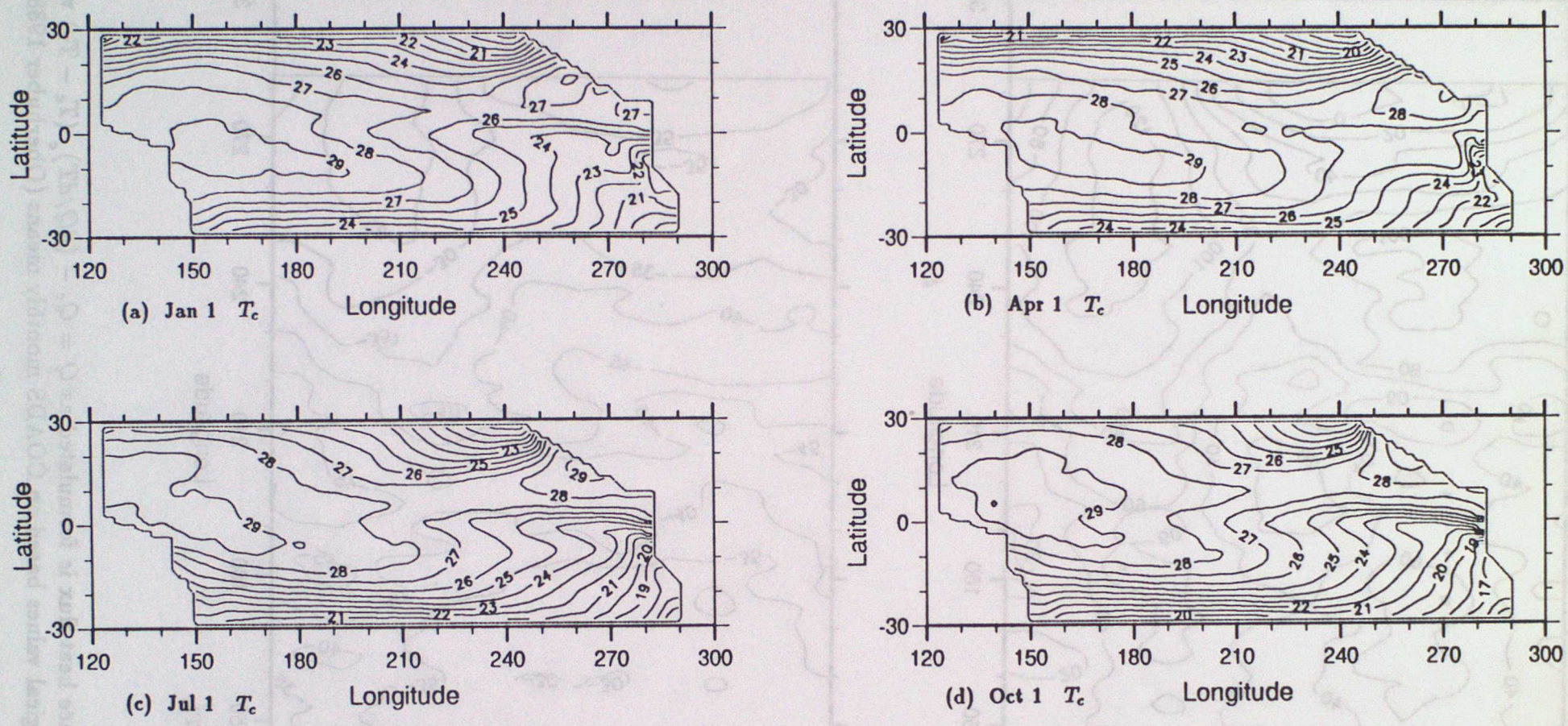

Fig. 8.2: Climatological sea surface temperature T_c $°C$ interpolated from COADS monthly means.

(a) Jan 1

(b) Apr 1

(c) Jul 1

(d) Oct 1

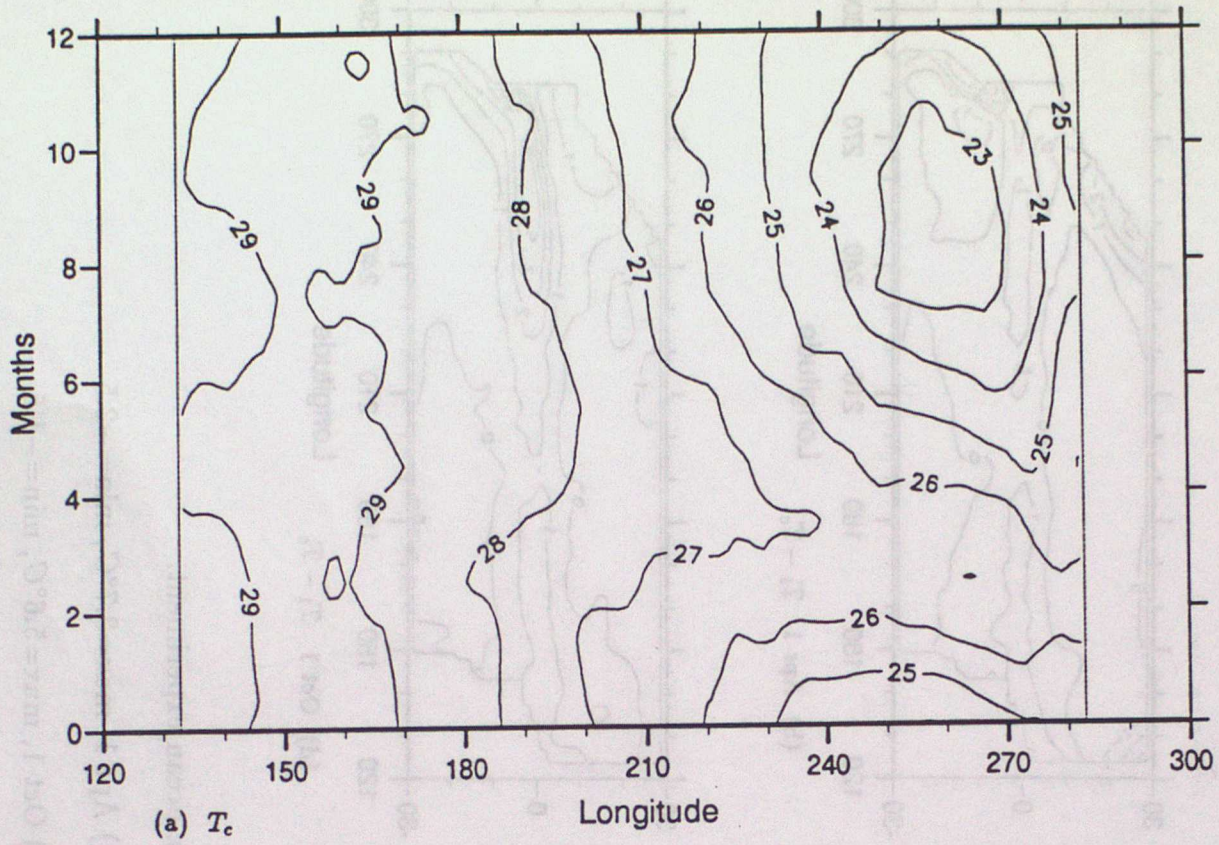

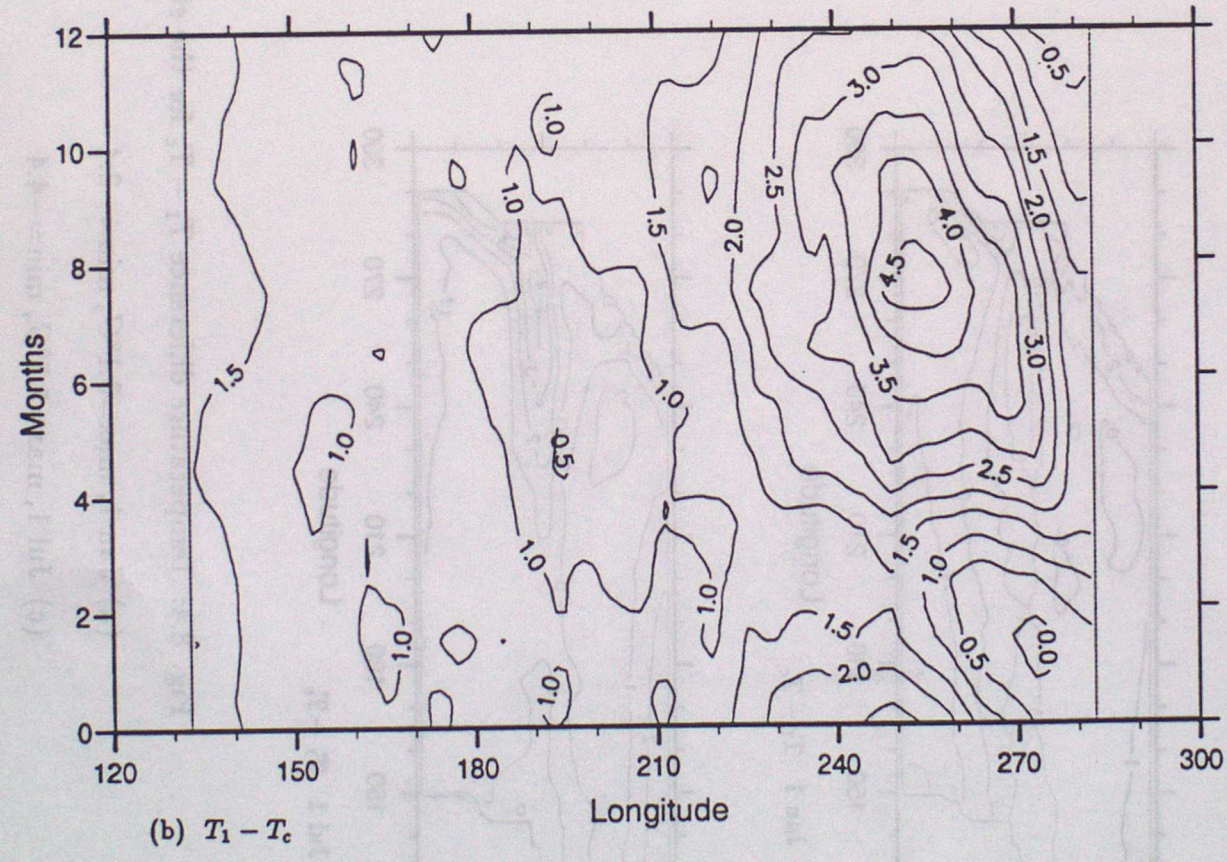

Fig. 8.3: Seasonal cycles along the equator.

(a) Climatological sea surface temperature T_c

(b) Temperature difference $T_1 - T_c$ for the static ocean experiment: max=4.8°C, min=−0.2 .

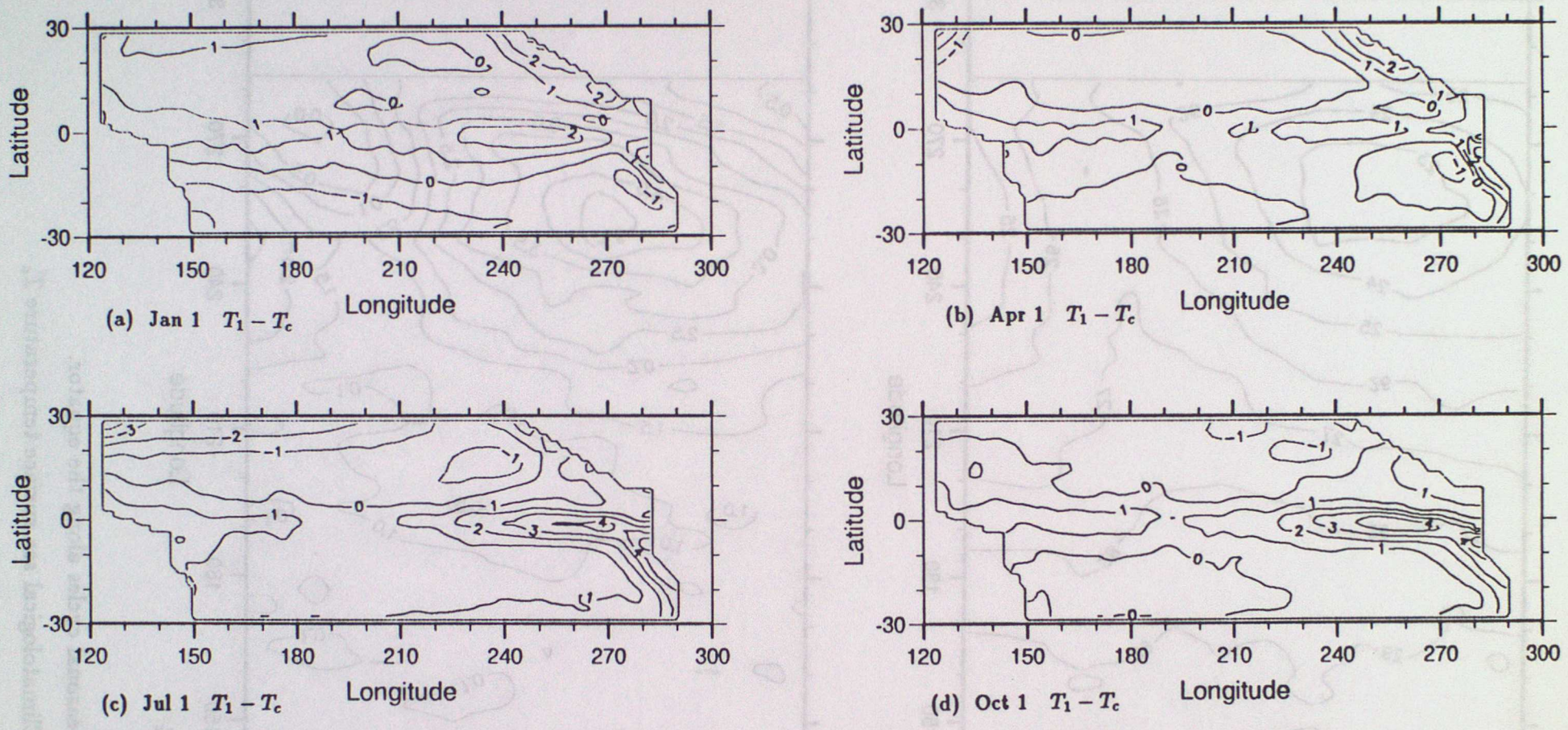

Fig. 8.4: Temperature difference $T_1 - T_c$ for the static ocean experiment.

(a) Jan 1, max=3.1°C, min=−2.4

(b) Apr 1, max=3.7°C, min=−2.5

(c) Jul 1, max=5.7°C, min=−4.4

(d) Oct 1, max=5.6°C, min=−1.5 .

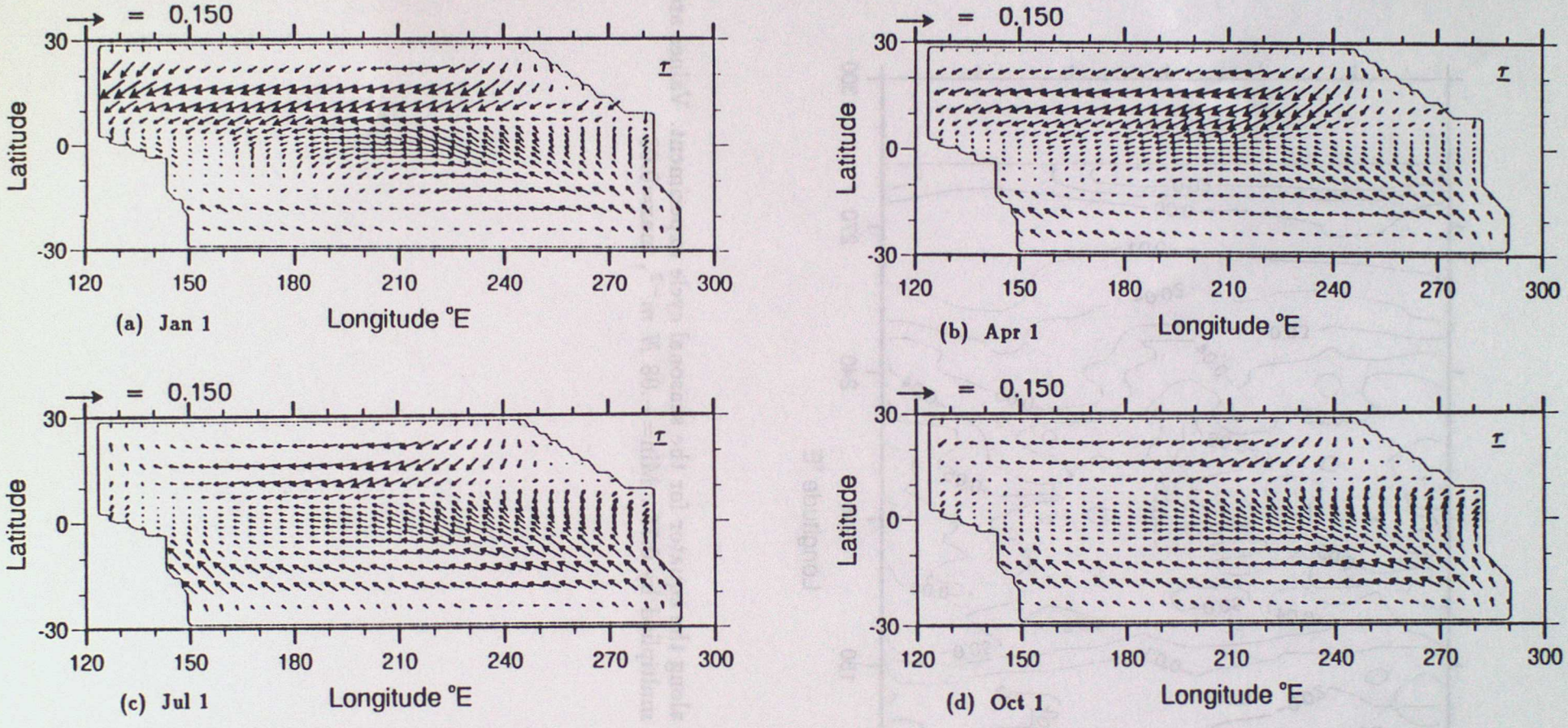

Fig. 9.1: Wind stress vectors for the seasonal cycle experiment, based on the Hellerman dataset. The Hellerman stresses are multiplied by 0.75 and are reduced to zero near the northern and southern boundaries of the model ocean.

(a) Jan 1, max=0.13 $N\ m^{-2}$

(b) Apr 1, max=0.12 $N\ m^{-2}$

(c) Jul 1, max=0.10 $N\ m^{-2}$

(d) Oct 1, max=0.09 $N\ m^{-2}$

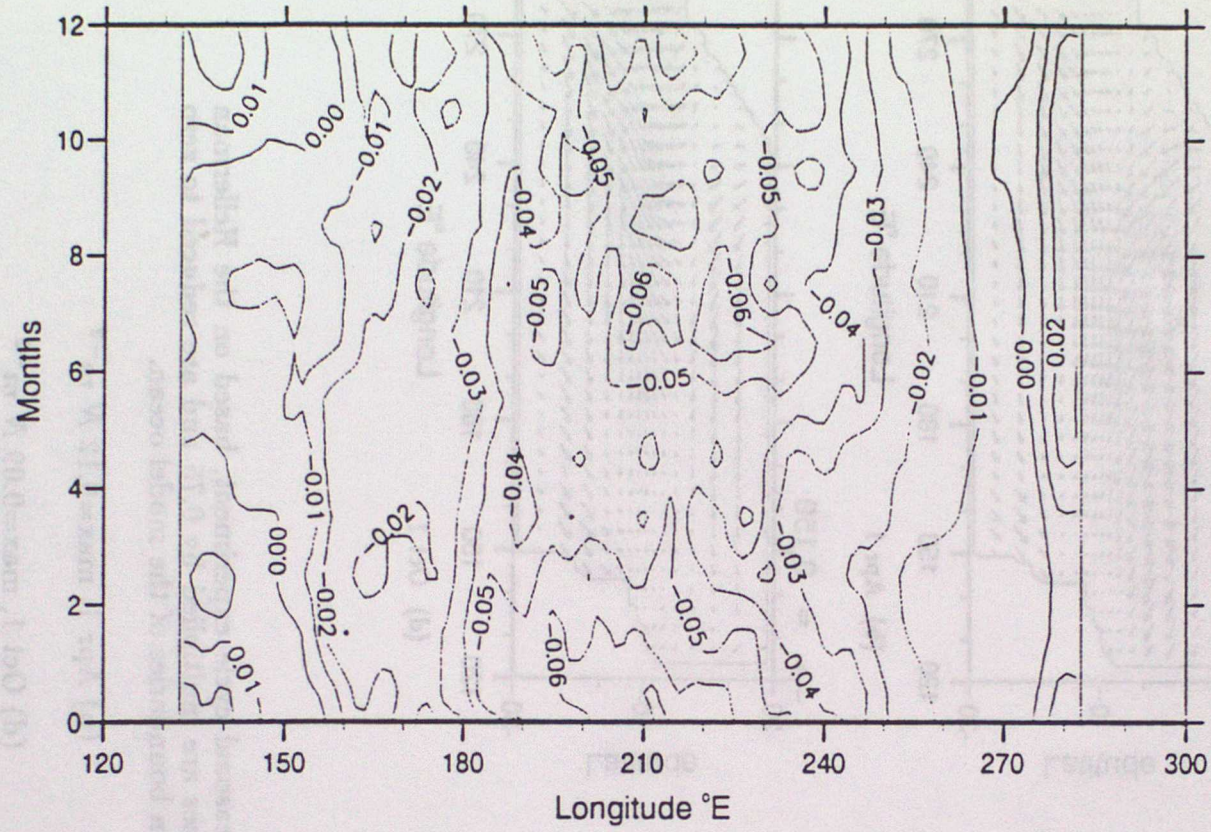

Fig. 9.2: Zonal wind stress along the equator for the seasonal cycle experiment. Values are from the Hellerman dataset, multiplied by 0.75 . Min=$-.08$ $N\ m^{-2}$, max=0.03

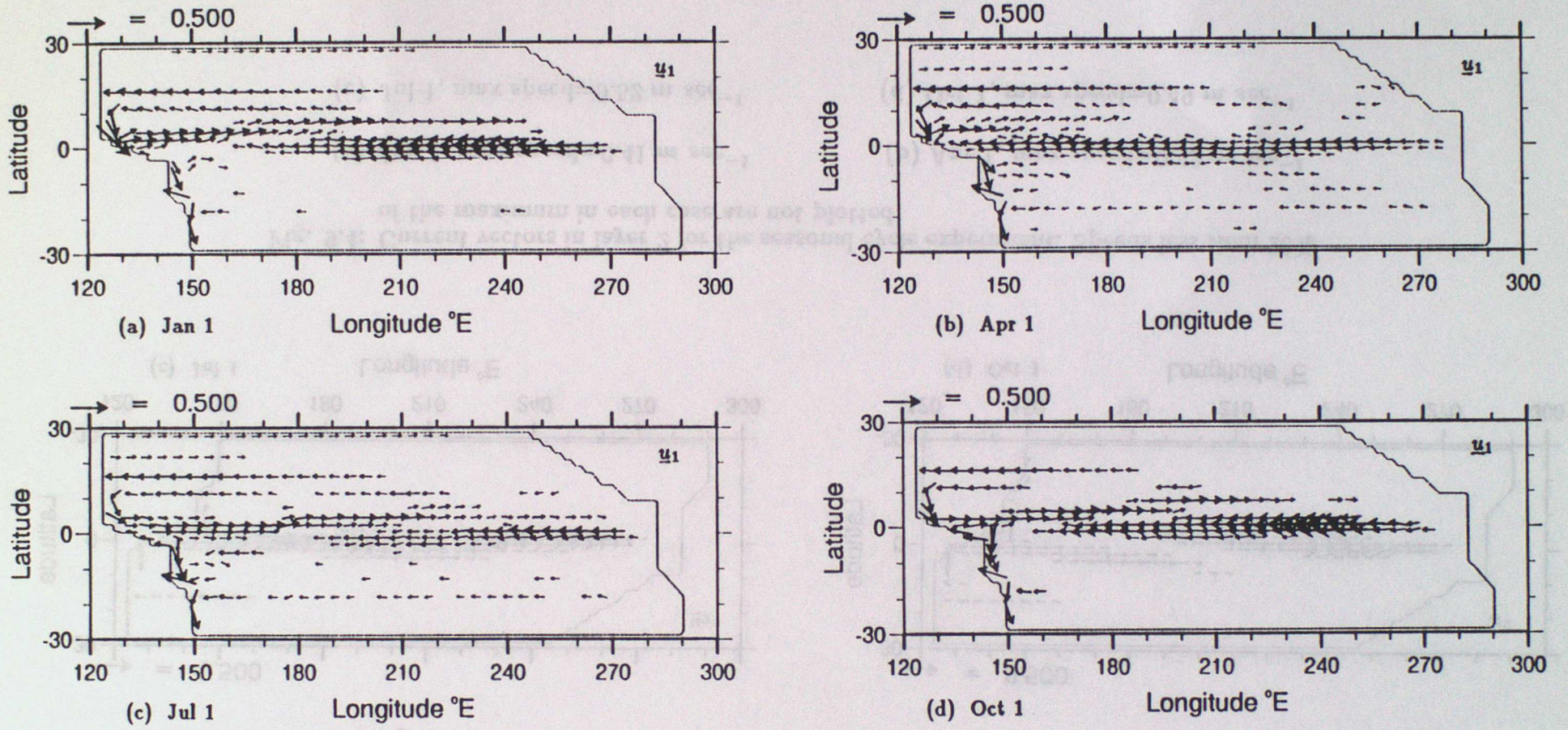

Fig. 9.3: Current vectors in layer 1 for the seasonal cycle experiment. Speeds less than 20% of the maximum in each case are not plotted.

(a) Jan 1, max speed=0.63 $m\ sec^{-1}$

(b) Apr 1, max speed=0.45 $m\ sec^{-1}$

(c) Jul 1, max speed=0.51 $m\ sec^{-1}$

(d) Oct 1, max speed=0.81 $m\ sec^{-1}$

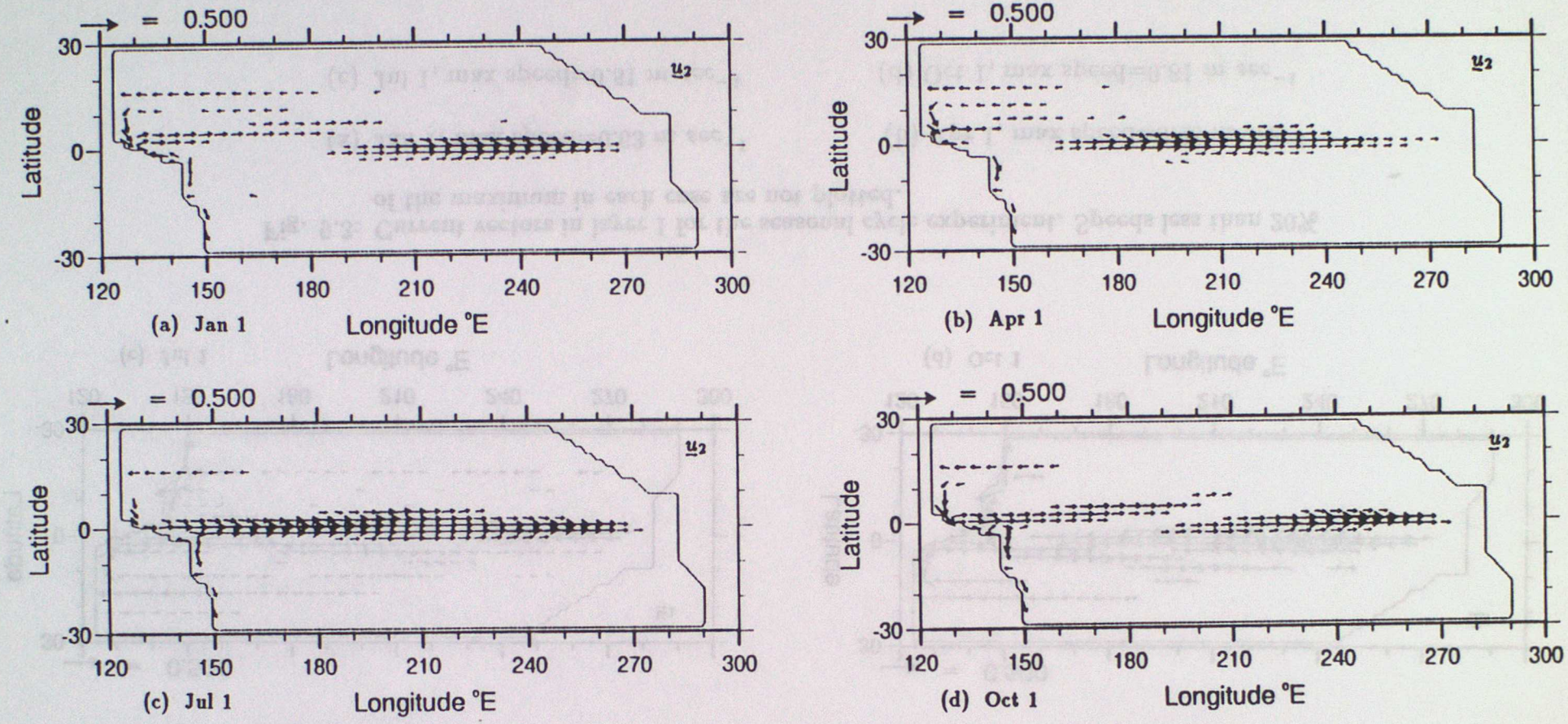

Fig. 9.4: Current vectors in layer 2 for the seasonal cycle experiment. Speeds less than 20% of the maximum in each case are not plotted.

(a) Jan 1, max speed=0.41 $m\ sec^{-1}$

(b) Apr 1, max speed=0.42 $m\ sec^{-1}$

(c) Jul 1, max speed=0.52 $m\ sec^{-1}$

(d) Oct 1, max speed=0.49 $m\ sec^{-1}$

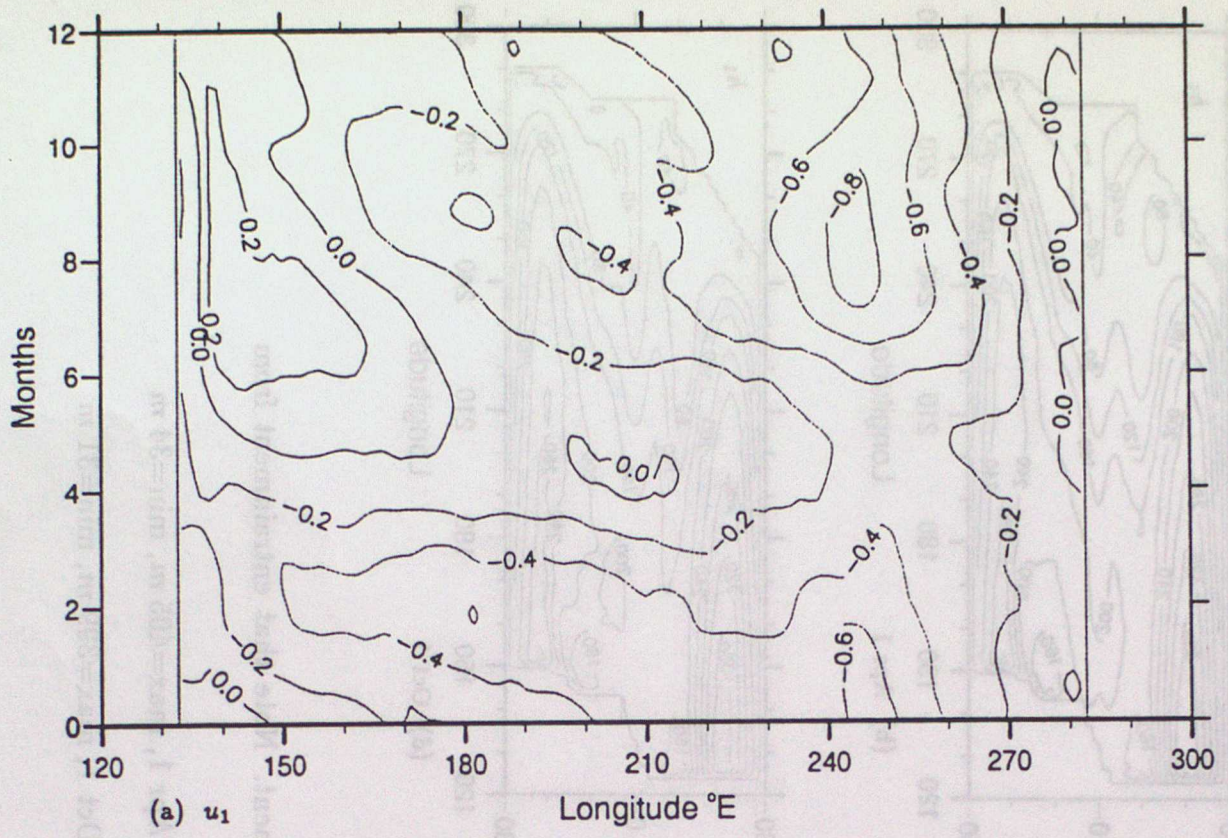

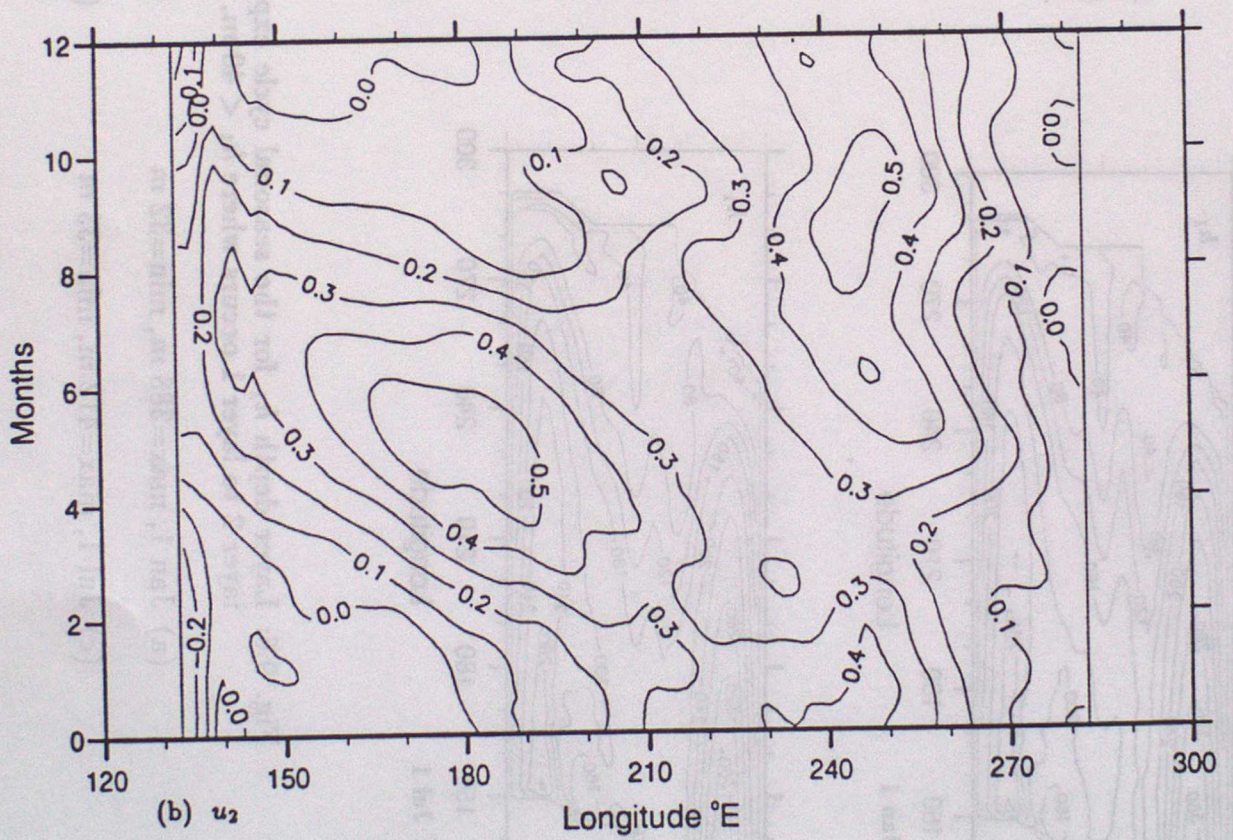

Fig. 9.5: Zonal velocity along the equator for the seasonal cycle experiment.

(a) u_1, min=$-0.86\ m\ sec^{-1}$, max=0.36

(b) u_2, min=$-0.29\ m\ sec^{-1}$, max=0.57

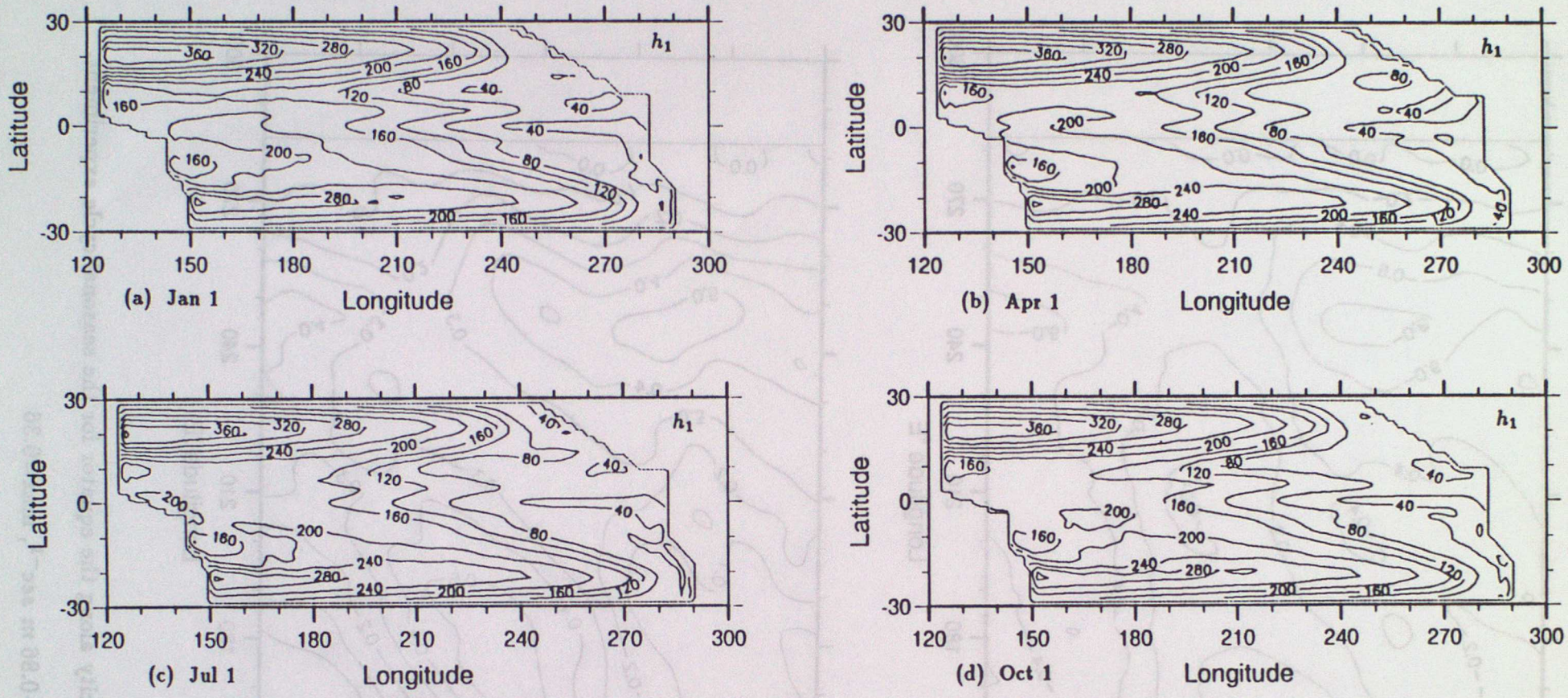

Fig. 9.6: Layer depth h_1 for the seasonal cycle experiment. Note that entrainment from layer 2 to layer 1 occurs where $h_1 < 40\ m$.

(a) Jan 1, max=388 m, min=32 m

(b) Apr 1, max=405 m, min=34 m

(c) Jul 1, max=412 m, min=33 m

(d) Oct 1, max=399 m, min=31 m

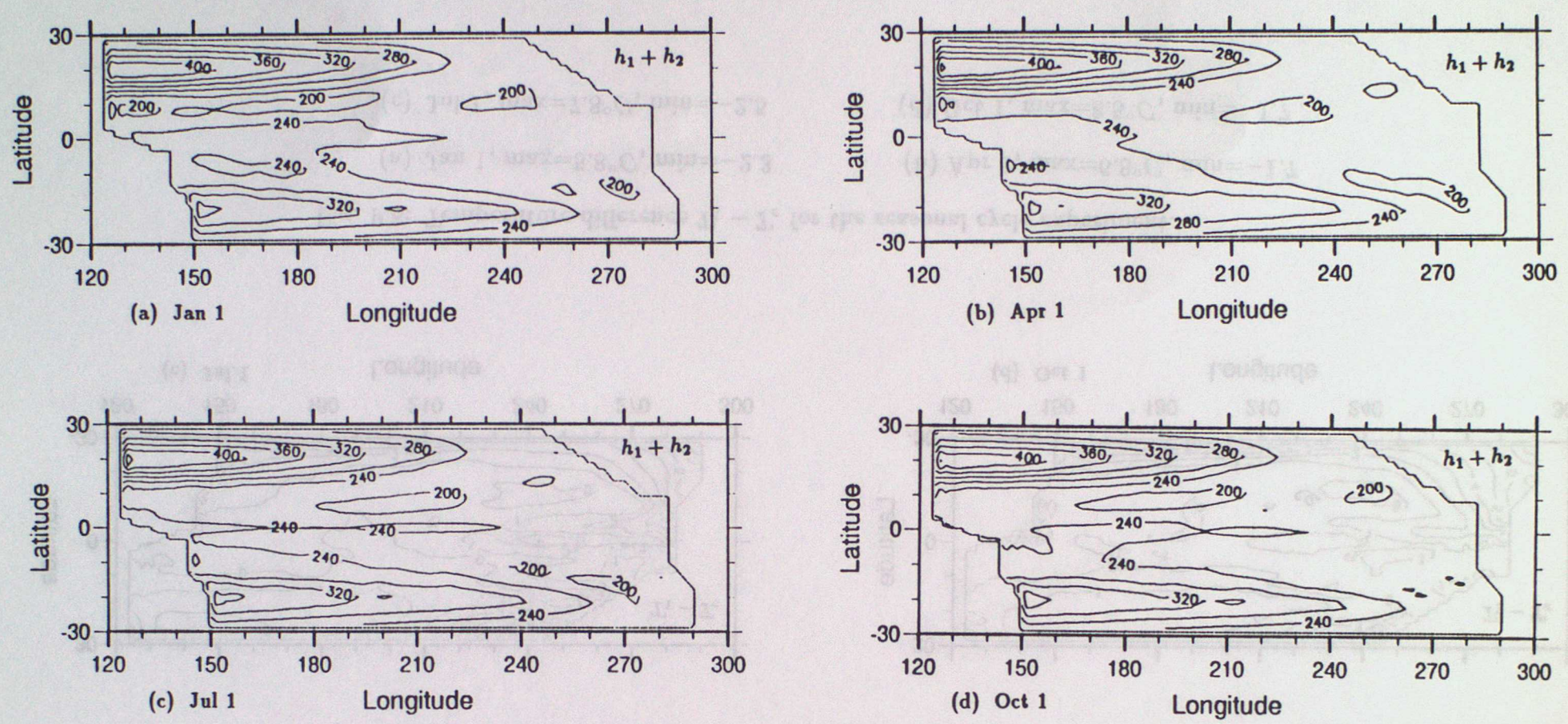

Fig. 9.7: Depth $h_1 + h_2$ for the seasonal cycle experiment.

(a) Jan 1, max=434 m, min=184 m

(b) Apr 1, max=456 m, min=181 m

(c) Jul 1, max=464 m, min=177 m

(d) Oct 1, max=444 m, min=183 m

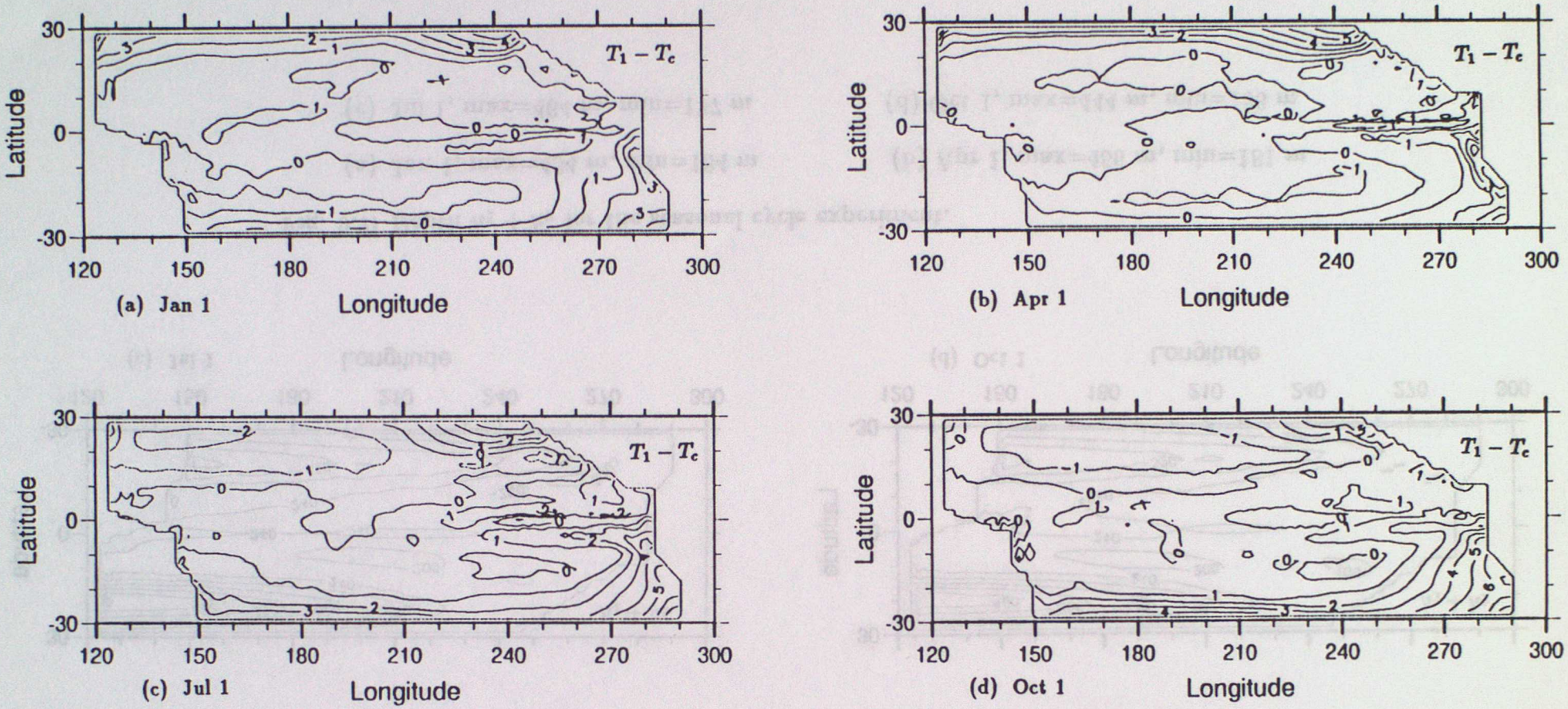

Fig. 9.8: Temperature difference $T_1 - T_c$ for the seasonal cycle experiment.

(a) Jan 1, max=5.8°C, min=−2.3

(b) Apr 1, max=6.8°C, min=−1.7

(c) Jul 1, max=7.8°C, min=−2.5

(d) Oct 1, max=8.5°C, min=−1.7 .

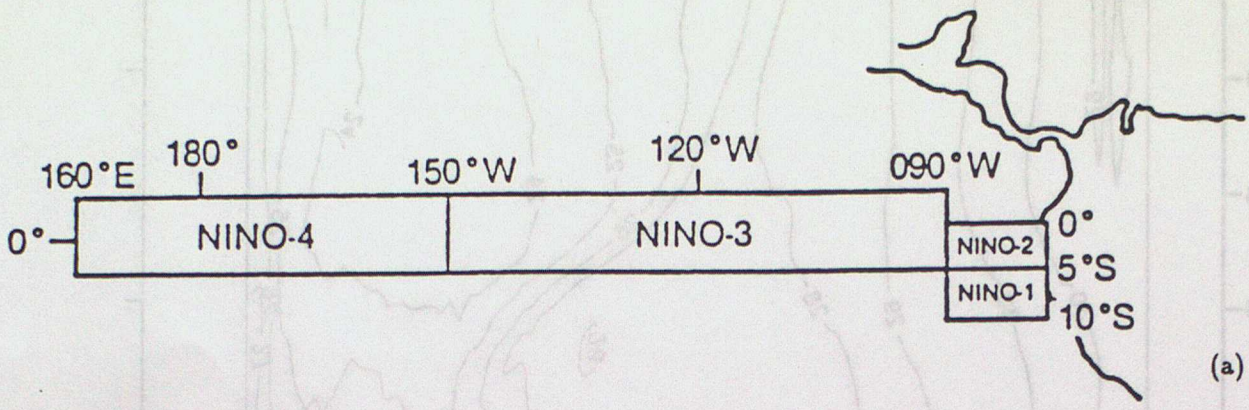

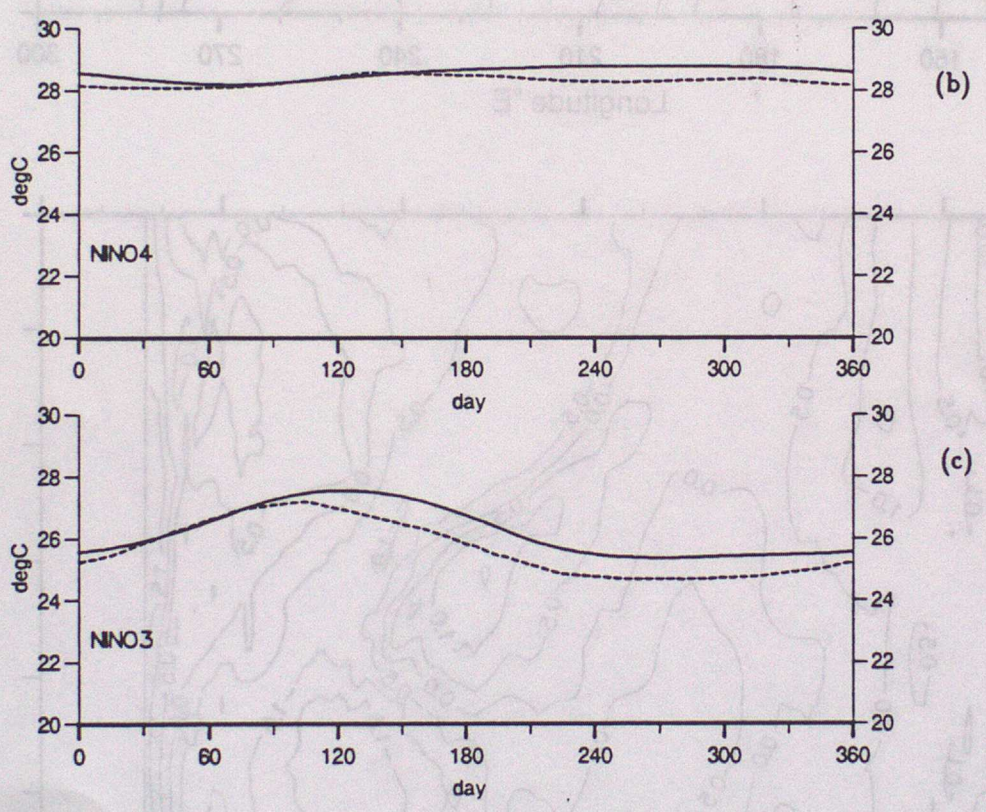

Fig. 9.9: Area averages for the seasonal cycle experiment.

(a) Location of the NINO areas

(b) Average temperature for NINO4: T_1 solid, T_c dashed.

(c) Average temperature for NINO3: T_1 solid, T_c dashed.

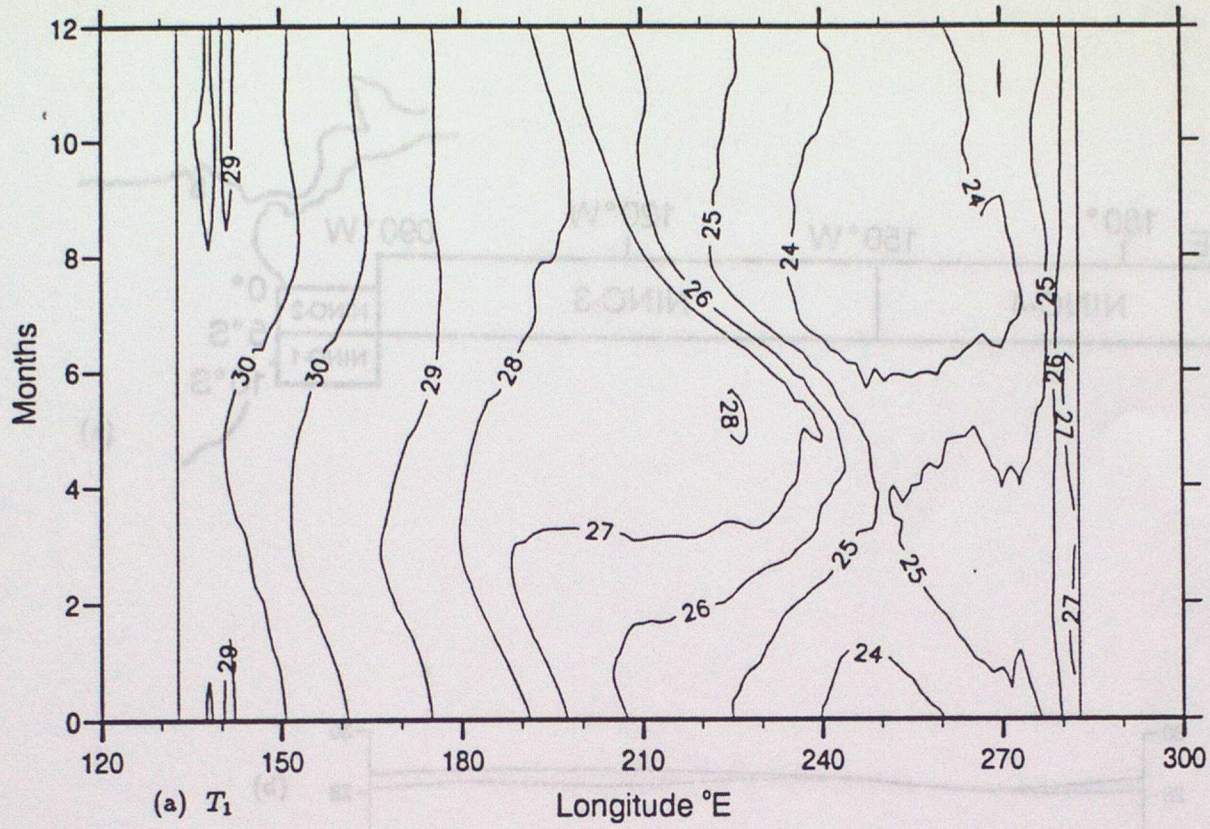

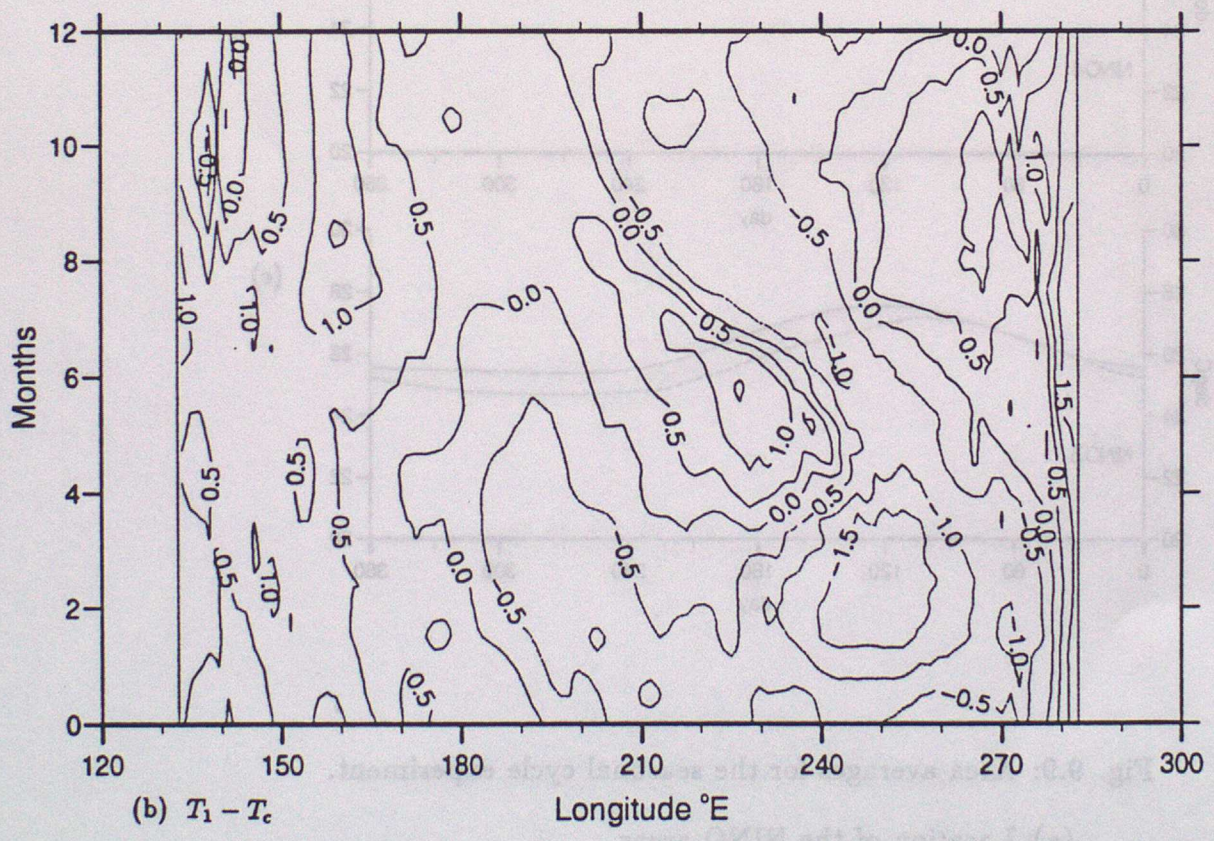

Fig. 9.10: Temperatures along the equator for the seasonal cycle experiment.

(a) Upper layer temperature T_1

(b) Temperature difference $T_1 - T_c$.
Max=1.8°C, min=-2.0

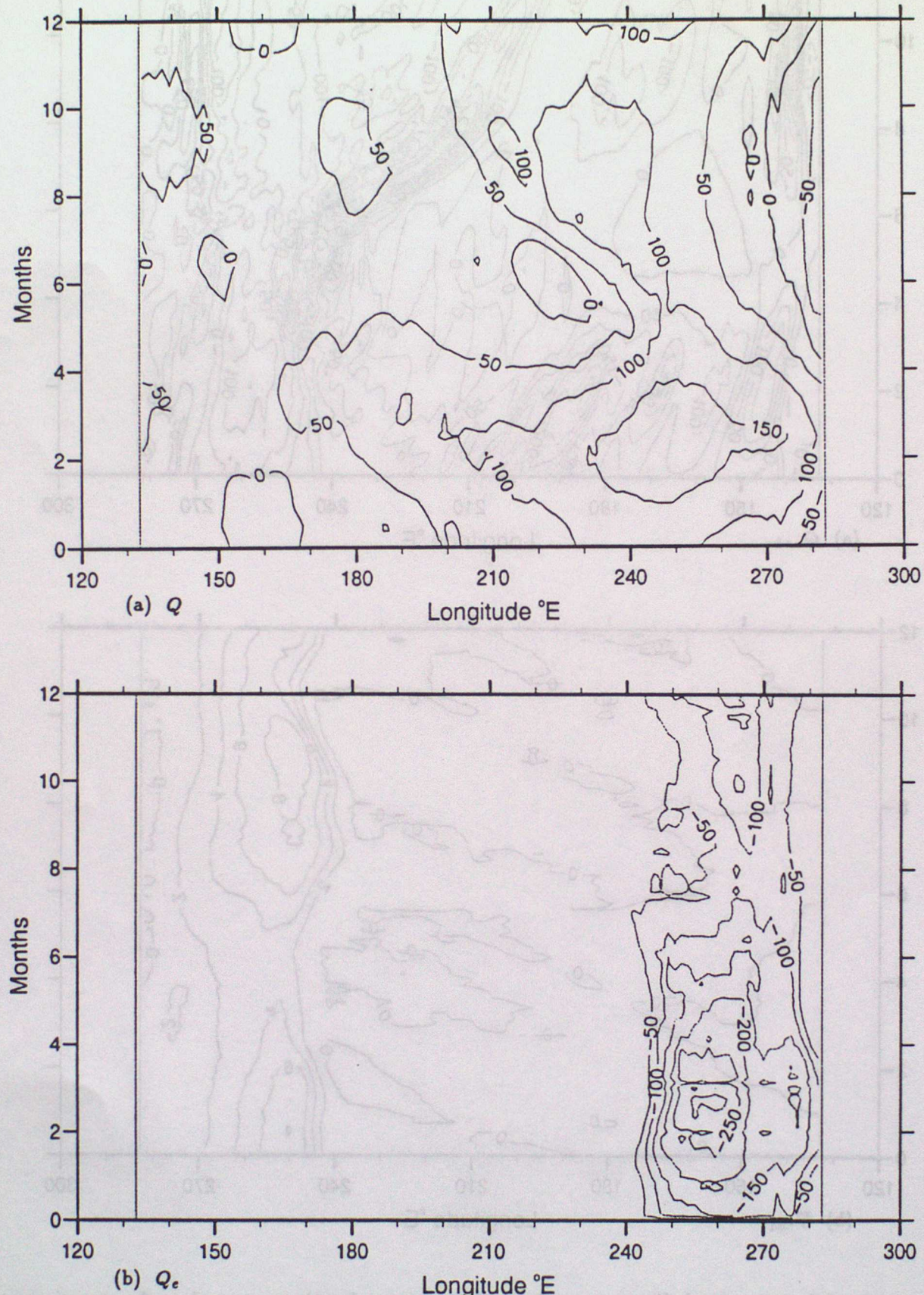

Fig. 9.11: Heat fluxes along the equator for the seasonal cycle experiment.

(a) Surface heat flux $Q = Q_c - (dQ/dT)_c(T_c - T_1)$
Max=181 $W\ m^{-2}$, min=-80

(b) Entrainment heat flux $Q_e = -\rho c_p(T_1 - T_2)w_{e1}$
Min=$-320\ W\ m^{-2}$, max=0

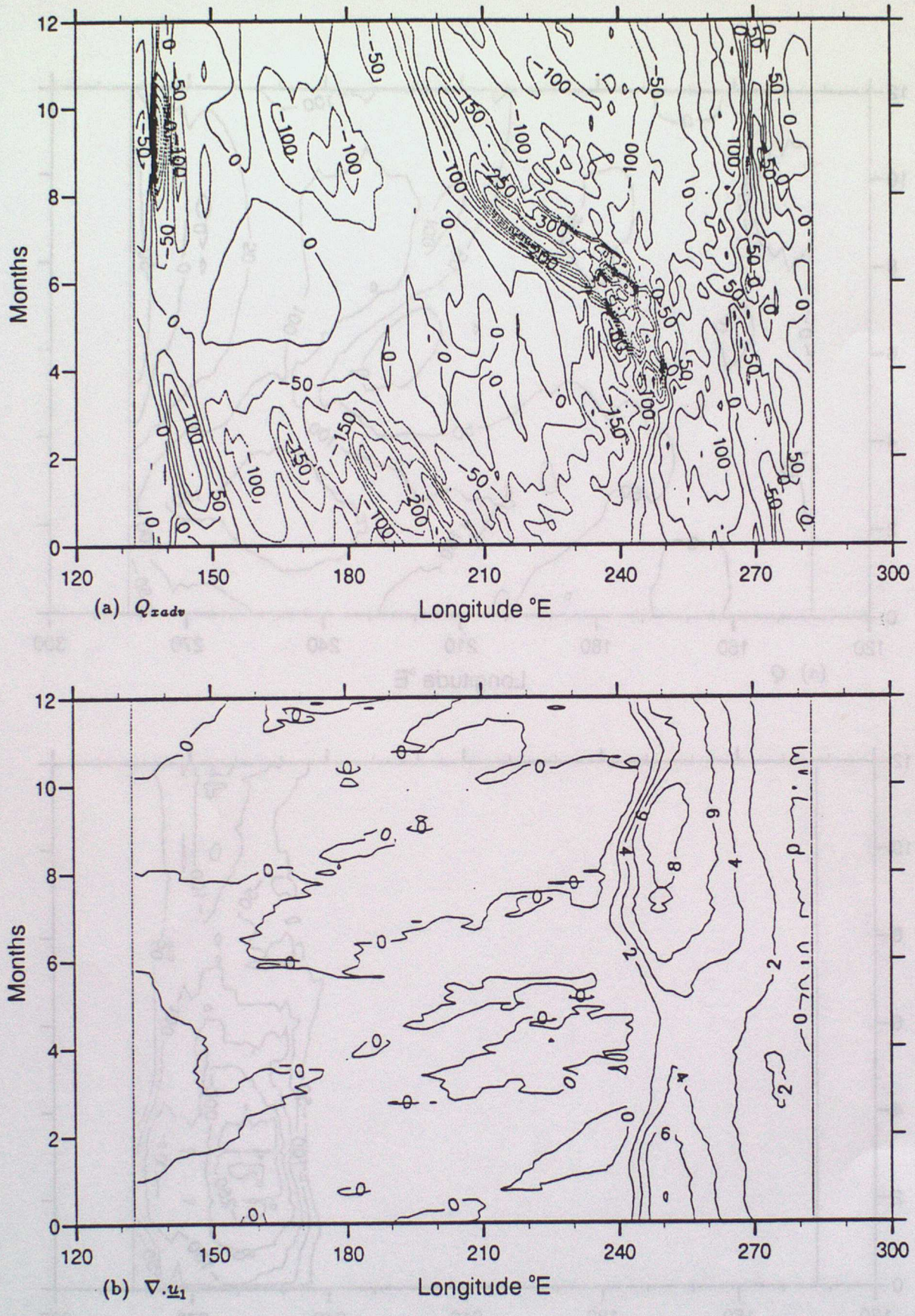

Fig. 9.12: Advection and divergence along the equator for the seasonal cycle experiment.

(a) Zonal heat flux $Q_{xadv} = -\rho c_p \bar{h}_1 u_1 \partial T_1 / \partial x$
Min=$-455\ W\ m^{-2}$, max=201

(b) $\nabla.\underline{u}_1$
Min=$-0.6 \times 10^{-7}\ sec^{-1}$, max=$9.7 \times 10^{-7}$

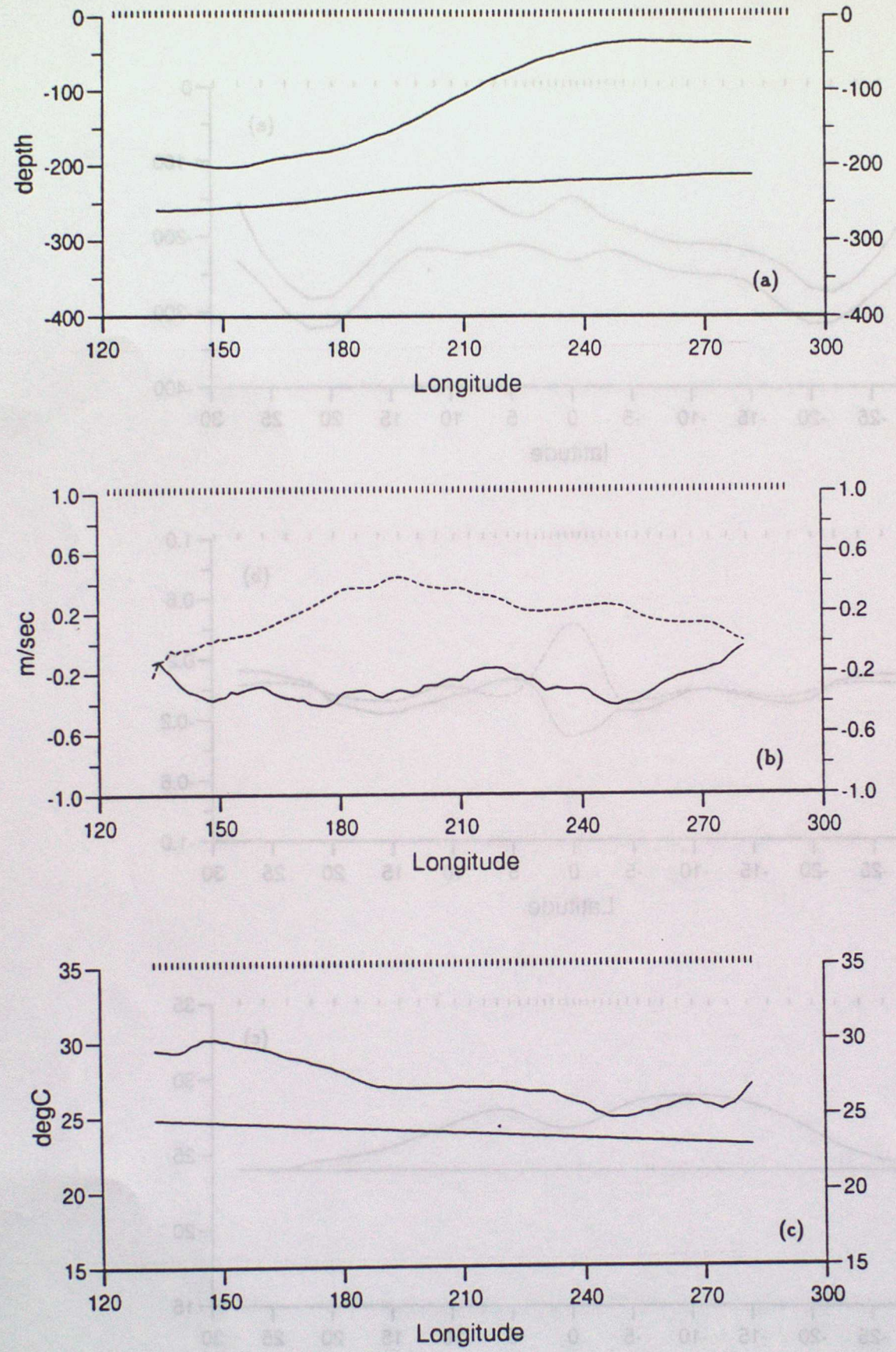

Fig. 9.13: Sections along the equator for April 1 for the seasonal cycle experiment.

(a) h_1 (upper curve) and $h_1 + h_2$ (lower curve)

(b) u_1 (solid curve) and u_2 (dashed curve)

(c) T_1 (upper curve) and T_2 (lower curve)

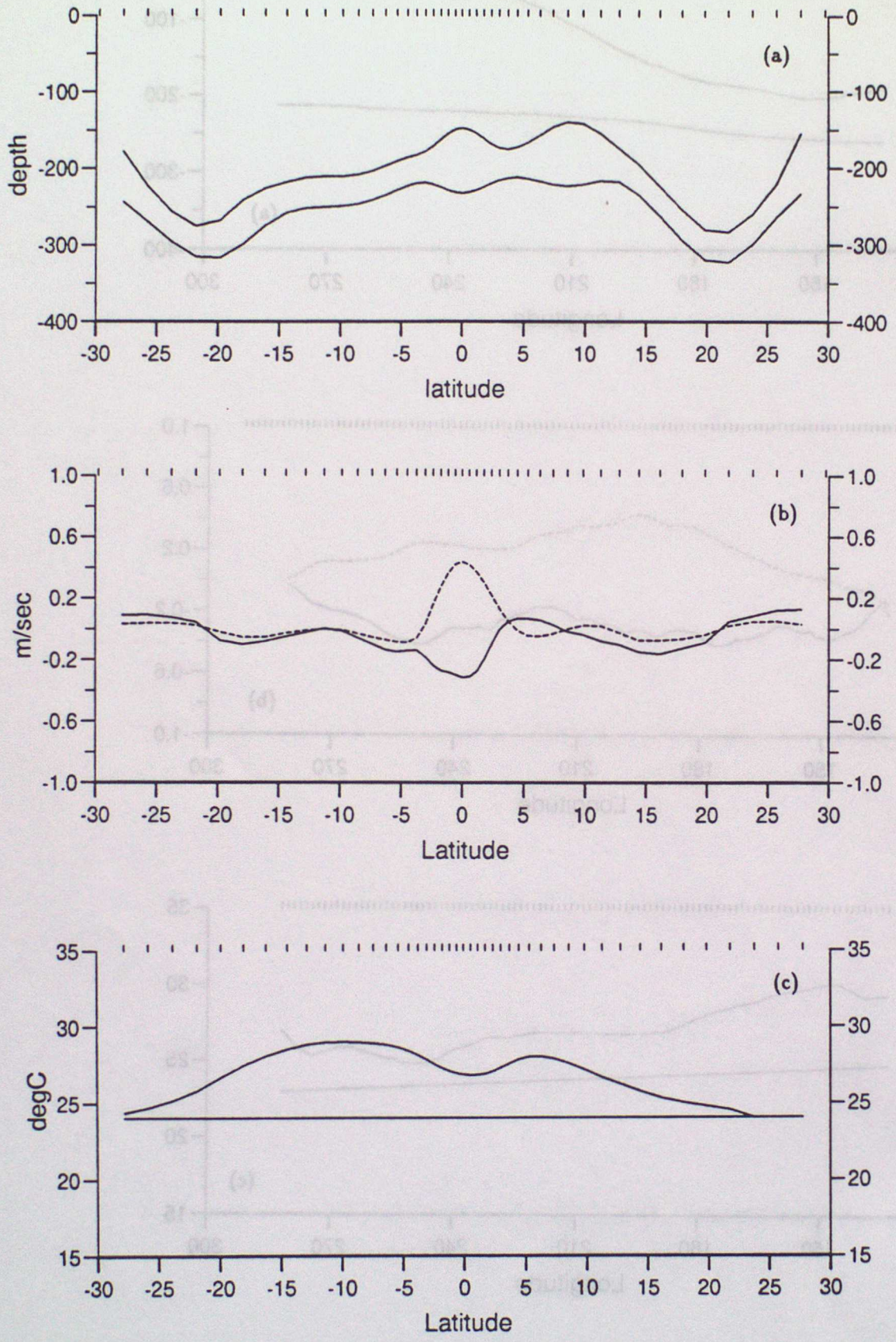

Fig. 9.14: Sections along 195°E for April 1 from the seasonal cycle experiment.

(a) h_1 (upper curve) and $h_1 + h_2$ (lower curve)

(b) u_1 (solid curve) and u_2 (dashed curve)

(c) T_1 (upper curve) and T_2 (lower curve)

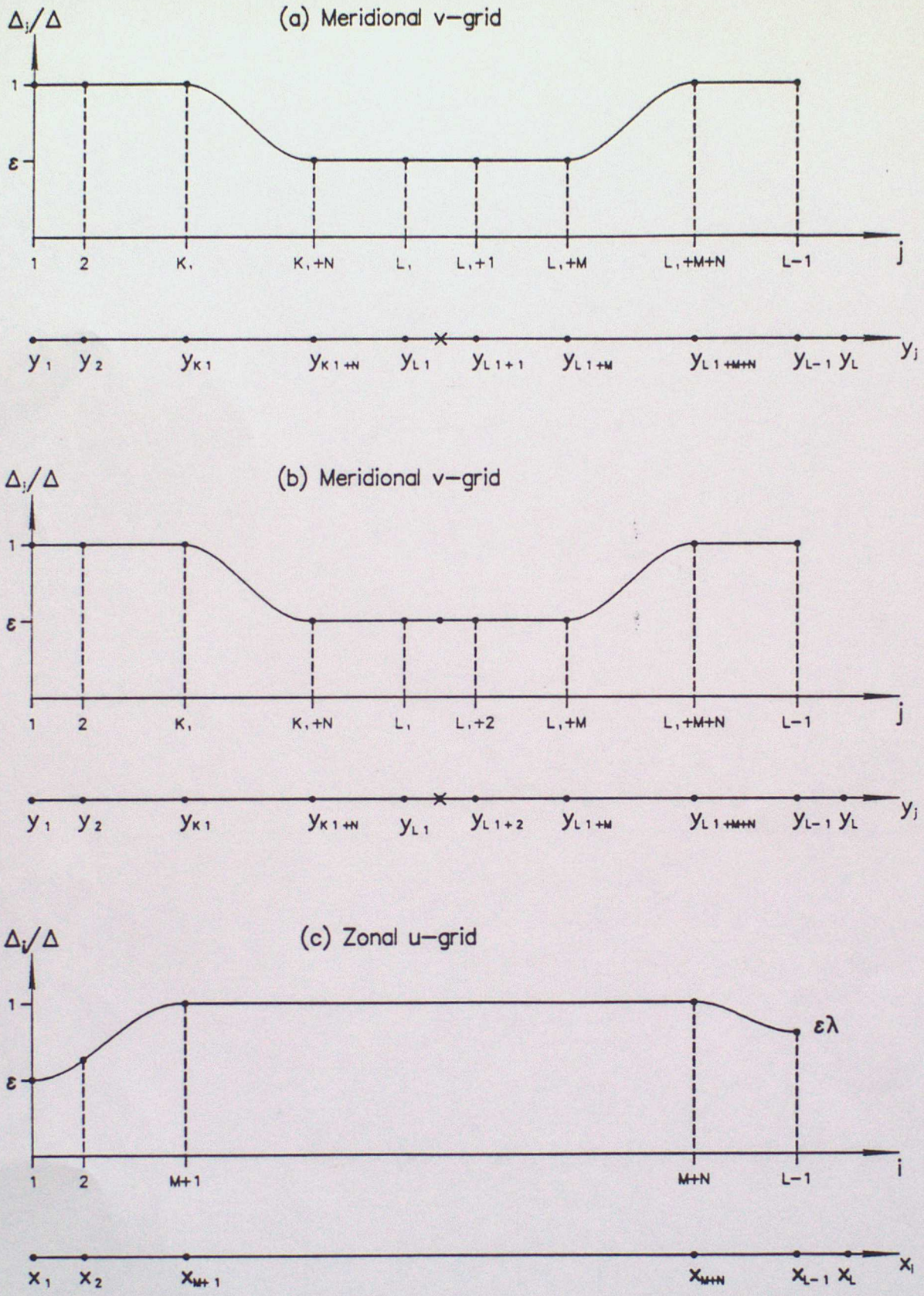

Fig. B1: Grid intervals and velocity points for the grid-generating algorithms.

(a) v-points with no point on the equator

(b) v-points with a point on the equator

(c) u-points

CLIMATE RESEARCH TECHNICAL NOTES

CRTN 1	Oct 1990	Estimates of the sensitivity of climate to vegetation changes using the Penman-Monteith equation. P R Rowntree
CRTN 2	Oct 1990	An ocean general circulation model of the Indian Ocean for hindcasting studies. D J Carrington
CRTN 3	Oct 1990	Simulation of the tropical diurnal cycle in a climate model. D P Rowell
CRTN 4	Oct 1990	Low frequency variability of the oceans. C K Folland, A Colman, D E Parker and A Bevan
CRTN 5	Dec 1990	A comparison of 11-level General Circulation Model Simulations with observations in the East Sahel. K Maskell
CRTN 6	Dec 1990	Climate Change Prediction. J F B Mitchell and Qing-cun Zeng
CRTN 7	Jan 1991	Deforestation of Amazonia - modelling the effects of albedo change. M F Mylne and P R Rowntree
CRTN 8	Jan 1991	The role of observations in climate prediction and research. D J Carson
CRTN 9	Mar 1991	The greenhouse effect and its likely consequences for climate change. D J Carson
CRTN 10	Apr 1991	Use of wind stresses from operational N.W.P. models to force an O.G.C.M. of the Indian Ocean. D J Carrington
CRTN 11	Jun 1991	A new daily Central England Temperature series, 1772-1991. D E Parker, T P Legg and C K Folland
CRTN 12	Jul 1991	Causes and predictability of Sahel rainfall variability. D P Rowell, C K Folland, K Maskell, J A Owen, M N Ward
CRTN 13	Jul 1991	Modelling changes in climate due to enhanced CO_2, the role of atmospheric dynamics, cloud and moisture. C A Senior, J F B Mitchell, H Le Treut and Z-X Li

CLIMATE RESEARCH TECHNICAL NOTES

CRTN 14	Sep 1991	Sea temperature bucket models used to correct historical SST data in the Meteorological Office. C K Folland
CRTN 15	Aug 1991	Modelling climate change, and some potential effects on agriculture in the U.K. P R Rowntree, B A Callander and J Cochrane
CRTN 16	Aug 1991	The Boreal Forests and Climate G Thomas and P R Rowntree
CRTN 17	Aug 1991	Development of a Stratosphere-Troposphere Data Assimilation System. R Swinbank.
CRTN 18	Sep 1991	A study of asynchronous coupling using a simple climate model. M K Davey.
CRTN 19	Sep 1991	The Oceanic Carbon Cycle. N K Taylor
CRTN 20	Nov 1991	Worldwide ocean-atmosphere surface fields in Sahel wet and dry years using provisionally corrected surface wind data. M N Ward
CRTN 21	Dec 1991	Coupled tropical ocean global atmosphere models at the UKMO. M K Davey, C Gordon, S Ineson and S Lawrence
CRTN 22	Dec 1991	Empirical parameterisation of tropical ocean-atmosphere coupling. M Allen, M K Davey, D L T Anderson and P D Killworth
CRTN 23	Feb 1992	The temporal evolution of Equatorial Currents in the Indian Ocean D L T Anderson, D J Carrington, R A Corry and C Gordon
CRTN 24	Feb 1992	Stratospheric analyses provided by the U.K. Meteorological Office M J Bailey, A O'Neill and V D Pope
CRTN 25	Feb 1992	Modelling interannual variability in the Indian Ocean using momentum fluxes from the UKMO and ECMWF operational weather analyses. D L T Anderson and D J Carrington

CLIMATE RESEARCH TECHNICAL NOTES

CRTN 26	Mar 1992	A GCM simulation of the impact of Amazonian deforestation on climate using an improved canopy representation J Lean and P R Rowntree
CRTN 27	Mar 1992	The parameterization of rainfall interception in GCMs A J Dolman and D Gregory
CRTN 28	Jun 1992	Development of worldwide marine data eigenvectors since 1985 A W Colman
CRTN 29	Jun 1992	A tropical ocean model with reduced physics M K Davey